

UNIVERSITY OF LJUBLJANA  
FACULTY OF MATHEMATICS AND PHYSICS  
DEPARTMENT OF PHYSICS

Luka Šantelj

MEASUREMENT OF TIME-DEPENDENT  
CP VIOLATION IN  $B \rightarrow \eta' K_S^0$  DECAYS

Doctoral thesis

ADVISOR: prof. Boštjan Golob

Ljubljana, 2013



UNIVERZA V LJUBLJANI  
FAKULTETA ZA MATEMATIKO IN FIZIKO  
ODDELEK ZA FIZIKO

Luka Šantelj

MERITEV ČASOVNO ODVISNE KRŠITVE  
SIMETRIJE CP V RAZPADU  $B \rightarrow \eta' K_S^0$

Doktorska disertacija

MENTOR: prof. Boštjan Golob

Ljubljana, 2013



## Abstract

We present a measurement of the time-dependent CP violation parameters in  $B^0 \rightarrow \eta' K_S^0$  decays. Measurement is based on a data sample that contains 772 millions  $B\bar{B}$  pairs collected at the  $Y(4S)$  resonance, with the Belle detector at the KEKB asymmetric-energy  $e^+e^-$  collider. The measured values of the CP violation parameters are:  $S_{\eta' K_S^0} = +0.71 \pm 0.07 \pm 0.03$  and  $\mathcal{A}_{\eta' K_S^0} = +0.02 \pm 0.05 \pm 0.03$ , where the first uncertainty is statistical and the second is systematic. The obtained values are the most accurate up-to-date and are consistent with expectations from other measurements and the Standard Model prediction.

**Keywords:** CP violation —  $B$  mesons: hadronic decays — Standard Model — Belle detector —  $B \rightarrow \eta' K_S^0$  decay

**PACS:** 11.30.Er, 13.25.Hw, 13.66.Jn



## Izvleček

V delu je predstavljena meritev časovno odvisne kršitve simetrije CP v razpadu  $B^0 \rightarrow \eta' K_S^0$ . Meritev je narejena na vzorcu  $772 \times 10^6$  parov mezonov  $B\bar{B}$ , zbranih z detektorjem Belle na asimetričnem  $e^+e^-$  trkalniku KEKB. Izmerjene vrednosti parametrov kršitve simetrije CP so:  $S_{\eta'K_S^0} = +0.71 \pm 0.07 \pm 0.03$  in  $A_{\eta'K_S^0} = +0.02 \pm 0.05 \pm 0.03$ , kjer je prva negotovost statistična in druga sistematska. Dobljene vrednosti so izmerjene najbolj natančno do sedaj in so v skladu s pričakovanji iz drugih meritev ter napovedmi Standardnega Modela.

**Ključne besede:** kršitev CP — mezoni  $B$ : hadronski razpadi — Standardni Model — detektor Belle — razpad  $B \rightarrow \eta' K_S^0$

**PACS:** 11.30.Er, 13.25.Hw, 13.66.Jn



## Acknowledgments

I would like to thank to my advisor Prof. Boštjan Golob for all his help and effort to make this thesis better. I am grateful to him and to Prof. Peter Križan, for their guidance and continuous support of my Ph.D study and research. My thanks also go to all members of the Ljubljana Belle group for their contribution to this work, and for a great research atmosphere.

I am grateful to all my closest friends for not allowing me to work as hard as my advisors would like me to. Finally, I would like to thank to my family for their endless support on every step of my way.



# Contents

<b>1</b>	<b>Introduction</b>	<b>13</b>
<b>2</b>	<b>CP violation in the Standard Model</b>	<b>17</b>
<b>3</b>	<b>CP violation in <math>B^0 \rightarrow \eta' K_S^0</math> decays</b>	<b>23</b>
3.1	Mixing of neutral $B$ mesons . . . . .	23
3.2	CP violation in neutral $B$ meson decays . . . . .	26
3.3	CP violation in $B^0 \rightarrow \eta' K_S^0$ . . . . .	28
<b>4</b>	<b>Principle of measurement</b>	<b>33</b>
4.1	From principle to reality . . . . .	35
<b>5</b>	<b>The Belle experiment</b>	<b>39</b>
5.1	The KEKB collider . . . . .	39
5.2	The Belle detector . . . . .	42
5.3	Offline computing . . . . .	56
<b>6</b>	<b>Preparation of measurement procedure</b>	<b>57</b>
6.1	$B^0 \rightarrow \eta' K_S^0$ decay . . . . .	59
6.2	Event reconstruction and selection . . . . .	59
6.3	Signal to background fraction fit . . . . .	71
6.4	Flavor tagging . . . . .	79
6.5	Vertex reconstruction . . . . .	80
6.6	Signal $\Delta t$ resolution function . . . . .	83
6.7	Background $\Delta t$ shape . . . . .	87
6.8	Extraction of CPV parameters . . . . .	89

## CONTENTS

---

<b>7</b>	<b>Validation tests</b>	<b>93</b>
7.1	Signal MC test . . . . .	93
7.2	Full MC test . . . . .	94
7.3	Control sample study . . . . .	96
7.4	Lifetime fit of $B^0 \rightarrow \eta' K_S^0$ data . . . . .	99
<b>8</b>	<b>Measurement results</b>	<b>101</b>
8.1	Toy MC ensemble test . . . . .	103
8.2	Systematic uncertainty . . . . .	104
<b>9</b>	<b>Conclusion</b>	<b>109</b>
<b>A</b>	<b>Analysis with <math>K_S^0 \rightarrow \pi^0 \pi^0</math></b>	<b>113</b>
A.1	Event reconstruction and selection . . . . .	113
A.2	Signal to background fraction fit . . . . .	114
A.3	Background $\Delta t$ shape . . . . .	116
A.4	Lifetime fit . . . . .	116
A.5	Fit of CPV parameters . . . . .	117
<b>B</b>	<b>Miscellaneous</b>	<b>119</b>
B.1	Units . . . . .	119
B.2	Wrong tag fractions and $\Delta t$ resolution function . . . . .	119
B.3	Tables of PDF shape parameters . . . . .	123
<b>C</b>	<b>SLOVENSKI POVZETEK</b>	
	<b>Meritev kršitve simetrije CP v razpadih <math>B^0 \rightarrow \eta' K_S^0</math></b>	<b>127</b>
C.1	Uvod . . . . .	127
C.2	Kršitev simetrije CP v Standardnem Modelu . . . . .	129
C.3	Kršitev simetrije CP v razpadu $B^0 \rightarrow \eta' K_S^0$ . . . . .	130
C.4	Detektor Belle . . . . .	133
C.5	Priprava postopka meritve . . . . .	135
C.6	Rezultat meritve . . . . .	143
C.7	Zaključek . . . . .	145

# 1

## Introduction

Symmetries are not only important in everyday life but also in science. Considering the symmetries of physical laws, we attempt to understand the dynamics of various physical systems. Especially important are the transformations under which certain physics phenomena are invariant. We say that such phenomena observe a given symmetry, or that they are symmetry invariant. The subject of this work is related to two discrete symmetries, parity **P** and charge conjugation **C**, that are of fundamental importance in modern physics. Assuming them to be exact symmetries of nature, the universe in which

- everything is replaced with its mirror image, **P**:  $\vec{r} \rightarrow -\vec{r}$ , or
- every particle is replaced with its antiparticle, **C**:  $x \rightarrow \bar{x}$ ,

would be indistinguishable from the actual universe and would follow exactly the same physical laws. Intuitively it seems natural that parity is conserved, or in other words, that nature has no preference about left or right. As it was known to be respected by gravitation, electromagnetic and the strong interaction, the conservation of parity was assumed to be a universal law. However, in the mid 1950s Chen Ning Yang and Tsung-Dao Lee suggested that the fourth of the fundamental interactions of nature, the weak interaction, might violate this law [1]. Indeed, parity violation of the weak interaction was confirmed in the famous  $^{60}\text{Co}$  experiment by Chien Shiung Wu and collaborators [2], earning Yang and Lee the 1957 Nobel Prize in Physics. This and further experiments showed that only left (right) handed neutrinos (anti-neutrinos) exist (or more exactly, only those participate in the weak interaction). Since the neutrinos are (almost) massless, handedness coincides with helicity, i.e.

the projection of spin on the particle's momentum. Hence both,  $\mathbf{C}$  and  $\mathbf{P}$ , are violated maximally by the weak interaction. Soon after this discovery, the combined  $\mathbf{CP}$  symmetry was proposed as the exact symmetry of nature, representing the true symmetry between matter and antimatter. Taking the mirror image of a physical system and replacing every particle with its antiparticle would result in exactly the same phenomena as in the original setting. The weak interaction seemed to violate  $\mathbf{P}$  and  $\mathbf{C}$  in a way that combined  $\mathbf{CP}$  is conserved. However, in the mid 1960s the second great surprise came. James Cronin, Val Fitch and coworkers provided an experimental demonstration that also  $\mathbf{CP}$  symmetry is violated in certain weak processes [3], in particular, in decays of neutral kaons<sup>1</sup>. Beside the discovery that  $\mathbf{CP}$  symmetry, which by then became widely believed to be exact, is violated, also the smallness of the observed violation was intriguing. It took nearly ten years for the breakthrough in understanding how the observed  $\mathbf{CP}$  violation can be connected with at that time emerging structure of the Standard Model (SM) of particle physics. In 1973 Makoto Kobayashi and Toshihide Maskawa pointed out that in the case of three quark generations the number of degrees of freedom in the SM naturally gives rise to the  $\mathbf{CP}$  violating complex phase in the  $3 \times 3$  quark mixing matrix, now known as the *Cabibbo–Kobayashi–Maskawa (CKM) matrix* [4] (note that in 1973 only the  $u, d, s$  quarks were known). Indeed, two new quarks were discovered soon after,  $c$  (1974) and  $b$  (1977), and finally also  $t$  in 1995. The CKM matrix has four free parameters (three angles and one complex phase) and in an elegant way encodes information on the relative strength of flavor changing weak decays, predicting correlations between different quark decays and  $\mathbf{CP}$  violating observables. The predicted large  $\mathbf{CP}$  violation in the  $B$  meson system was the main motivation for construction of two so-called  $B$  factory experiments, Belle [5] and BaBar [6]. Already in the first years of operation, in 2001, these two experiments observed decay time dependent  $\mathbf{CP}$  violation by analyzing decays of neutral  $B$  mesons to  $J/\psi K_S^0$ . This represented the first observation of  $\mathbf{CP}$  violation outside the kaon system [7, 8]. In the past decade Belle and BaBar have measured  $\mathbf{CP}$  violating observables in many decays<sup>2</sup> of  $B$  mesons, in some with only a few percent experimental uncertainty, and confirmed the single complex phase of the CKM matrix as the main source of  $\mathbf{CP}$  violation. After the experimental confirmation of their predictions Kobayashi and Maskawa were awarded the 2008 Nobel Prize in Physics.

So far the SM, a theory of electromagnetic, weak, and strong interaction with the CKM paradigm at the heart of its flavor sector, has proven to be a good description of Nature up to energies of nearly 1 TeV. Apart from the non-zero neutrino masses no significant deviations from the SM predictions, induced by possible new physics processes at some higher energy scale, were yet experimentally observed. However, the existence of new physics is assured at least by the fact the SM does not include

---

<sup>1</sup>Cronin and Fitch won the 1980 Nobel Prize in Physics for this discovery.

<sup>2</sup> $\mathbf{CP}$  violation is observed in about 20 different decay modes with more than  $3\sigma$  significance.

---

gravity, and also by non-zero neutrino masses. This makes us consider the SM as a low energy effective theory, valid up to some new physics energy scale  $\Lambda$ . Concerning the SM flavor sector, two intriguing facts in addition stimulate the thinking about new physics. First, the CKM matrix is almost a unit matrix. The origin of this hierarchy is unknown (as the elements of CKM matrix are free parameters of the SM) and indicates the presence of some new flavor symmetry at higher energy scale. Second, CP violation is one of the necessary conditions for the observed dominance of matter over antimatter in the present Universe [9], but the CP violating phase of CKM matrix fails by many orders of magnitude to explain the observed asymmetry [10]. Therefore, yet unknown additional CP violating phases must exist from the cosmological point of view.

The energy frontier experiments at the Large Hadron Collider have in recent years started to probe physics at the TeV energy scale. This research is stimulated by the well known fine tuning problem of the Higgs mass within the SM (the so-called *hierarchy problem*) implying the energy scale of new physics (i.e.  $\Lambda \sim \text{TeV}$ ). Strictly speaking, so far no deviations from the SM predictions were observed, although the long awaited discovery of the Higgs-like boson [11, 12] has not yet been decisively confirmed to be of the SM origin. On the other hand, the flavor physics, mainly supported by  $B$  physics measurements at  $B$  factories, already provides strong constraints on the flavor structure of new physics models at this energy scale. New physics, if present at the TeV scale, must most probably have a non-generic flavor structure in order to suppress the Flavor-Changing Neutral Current (FCNC) processes, which would otherwise violate current experimental limits. Despite a necessary mechanism of FCNC suppression, new flavor mixing and CP violating phases almost inevitably arise in a large class of new physics scenarios at TeV energies [13]. This gives the motivation for search of new physics effects in the wide range of FCNC processes available in  $B$  meson decays. Because FCNC processes can, within the SM, proceed only through the so-called penguin diagrams, one can investigate the effects of possible new heavy particles in quantum loops of these diagrams. At many points in the history of particle physics this approach turned out to be very fruitful, leading to several important breakthroughs<sup>3</sup>.

In this work we present a measurement of time-dependent CP violation in  $B^0 \rightarrow \eta' K_S^0$  decays. This decay is mediated by the  $b \rightarrow s\bar{q}q$  quark transition, which is an example of FCNC process induced by a penguin diagram, and as such sensitive to possible new CP violating phases. The decay final state  $\eta' K_S^0$  is a CP eigenstate into which both  $B^0$  and its antiparticle  $\bar{B}^0$  meson can decay. The SM predicts the asymmetry in time-dependent decay rates of  $B^0$  and  $\bar{B}^0$  mesons into  $\eta' K_S^0$  to be very close (at few % level [15–21]) to the asymmetry in  $B^0 \rightarrow J/\psi K_S^0$  decay. However,

---

<sup>3</sup>The existence of the *charm* quark was postulated to explain the smallness of FCNC (GIM mechanism [14]), observation of CP violation led to the prediction of third generation of quarks [4], the *top* quark mass was predicted based on the  $B^0$  mixing measurements.

the presence of new CP violating phases can potentially induce a large deviation between the asymmetries in these two decays. While the penguin dominated decay  $B \rightarrow \eta' K_S^0$ , can receive sizable contributions from such phases, the tree diagram dominated  $B^0 \rightarrow J/\psi K_S^0$  decay, is relatively insensitive to those phases. The very well measured CP asymmetry in the latter decay and a relatively clean SM prediction make CP violation in  $B^0 \rightarrow \eta' K_S^0$  decays one of the gold-plated observables for possible new CP violating phases.

The measurement presented here is based on a data sample that contains 772 million  $B\bar{B}$  pairs, collected with the Belle detector during the years of its operation (1999-2010). We start with a brief introduction to CP violation in the SM (chapter 2), which is followed by a description of possible manifestations of CP violation in the  $B$  meson system, and in particular in  $B^0 \rightarrow \eta' K_S^0$  decays, and a summary of previous experimental results, in chapter 3. Next, in chapter 4, we present the basic principles of time-dependent CP violation measurements at  $B$  factories, and describe the KEKB collider and Belle detector in chapter 5. After these introductory chapters we move to the performed measurement. In the main part of the work we describe the method of measurement (chapter 6) and its validation tests (chapter 7) in some detail. The results and the estimation of the systematic uncertainty of the method are presented in chapter 8. Finally we conclude in chapter 9 with some future prospects.

# 2

## CP violation in the Standard Model

The Standard Model is a theory that describes the dynamics of the known subatomic particles, driven by the electromagnetic, weak and strong interaction. Mathematically, it is formulated as a gauge field theory with the local  $SU(3)_C \times SU(2)_L \times U(1)$  gauge symmetry, and this internal symmetry essentially defines it. Usually we divide the SM into two sectors, one being the *quantum chromodynamics* with the  $SU(3)_C$  as a gauge symmetry that describes the strong interaction, and the other being the *electroweak theory* with the  $SU(2)_L \times U(1)$  symmetry that describes the unified electroweak interaction. Since CP violation resides in the latter part we briefly introduce its structure.

In the  $SU(2)_L \times U(1)$  gauge symmetry, the  $SU(2)_L$  represents the *weak isospin* and the  $U(1)$  represents the *weak hypercharge*. The subscript  $L$  indicates that only left handed fermions transform non-trivially under isospin, they belong to an isodoublet, while right handed fermions belong to an isosinglet. In the SM fermions come in three generations

$$\text{leptons: } l_L = \left( \begin{pmatrix} \nu_e \\ e \end{pmatrix}_L, \begin{pmatrix} \nu_\mu \\ \mu \end{pmatrix}_L, \begin{pmatrix} \nu_\tau \\ \tau \end{pmatrix}_L \right), \quad e_R, \mu_R, \tau_R \quad (2.1)$$

$$\text{quarks: } q_L = \left( \begin{pmatrix} u \\ d \end{pmatrix}_L, \begin{pmatrix} c \\ s \end{pmatrix}_L, \begin{pmatrix} t \\ b \end{pmatrix}_L \right), \quad u_R, d_R, c_R, s_R, t_R, b_R. \quad (2.2)$$

In the following text the notation  $\vec{e} = (e, \mu, \tau)$ ,  $\vec{\nu} = (\nu_e, \nu_\mu, \nu_\tau)$ ,  $\vec{u} = (u, c, t)$  and  $\vec{d} = (d, s, b)$  is also used. Hypercharge is also assigned to each of the degrees of freedom given above. To satisfy the  $SU(2)_L \times U(1)$  invariance, four gauge boson fields have to be introduced. After the electroweak symmetry breaking, these fields

result in the  $W^+, W^-$  and  $Z^0$  gauge bosons of the weak interaction and the photon  $A$ , a gauge boson of the electromagnetic interaction. A gauge invariant Lagrangian describing the interaction between the gauge bosons and fermions is given by

$$\mathcal{L}_{int} = \frac{g}{\sqrt{2}} \left( J_\mu^+ W^\mu + J_\mu^- W^{+\mu} \right) + e J_\mu^{em} A^\mu + \frac{g}{\cos \theta_W} \left( J_\mu^3 - \sin^2 \theta_W J_\mu^{em} \right) Z^\mu, \quad (2.3)$$

where

$$\begin{aligned} J_\mu^+ &= \bar{u}_L^i \gamma_\mu d_{L,i} + \bar{\nu}_L^i \gamma_\mu e_{L,i} \quad \text{is the charged weak current,} \\ J_\mu^3 &= \frac{1}{2} \left( \bar{u}_L^i \gamma_\mu u_{L,i} - \bar{d}_L^i \gamma_\mu d_{L,i} + \bar{\nu}_L^i \gamma_\mu \nu_{L,i} - \bar{e}_L^i \gamma_\mu e_{L,i} \right) \quad \text{is the neutral weak current,} \\ J_\mu^{em} &= \frac{2}{3} \bar{u}_L^i \gamma_\mu u_{L,i} - \frac{1}{3} \bar{d}_L^i \gamma_\mu d_{L,i} - \bar{e}_L^i \gamma_\mu e_{L,i} \quad \text{is the electromagnetic current,} \end{aligned} \quad (2.4)$$

$g$  and  $e$  are the coupling constants,  $\theta_W$  is the Weinberg angle, and the summation over generation index  $i = 1, 2, 3$  is assumed. As will be shown shortly, the CP violation manifests itself in  $\mathcal{L}_{int}$  introduced above, but its origin is actually in another part of the SM Lagrangian, namely in the couplings of the  $SU(2)$  doublet of the Higgs fields  $\phi$  with fermions

$$-\mathcal{L}_{HF} = f_u^{ij} \bar{q}_{L,i} \begin{pmatrix} \phi^0 \\ -\phi^- \end{pmatrix} u_{R,j} + f_d^{ij} \bar{q}_{L,i} \begin{pmatrix} \phi^+ \\ \phi^0 \end{pmatrix} d_{R,j} + f_e^{ij} \bar{l}_{L,i} \begin{pmatrix} \phi^0 \\ -\phi^- \end{pmatrix} e_{R,j}, \quad (2.5)$$

where  $\mathbf{f}_u, \mathbf{f}_d, \mathbf{f}_e$  are the generational coupling matrices. After the spontaneous symmetry breaking, the neutral Higgs field acquires the vacuum expectation value  $\langle \phi^0 \rangle = v$ , giving rise to the fermion mass terms, with the mass matrices  $\mathbf{M}_\alpha = v \mathbf{f}_\alpha$  ( $\alpha = u, d, e$ ). Since, within the SM, there is no prescription or symmetry constraining the content of  $\mathbf{f}_\alpha$ , the mass matrices  $\mathbf{M}_\alpha$  are in general non-diagonal. Therefore, the fermions introduced in (2.2) and used in  $\mathcal{L}_{int}$  are not mass eigenstates of the theory. To obtain the latter, we diagonalize each of the mass matrices with the help of two unitary matrices

$$\mathbf{S}_L^\alpha \mathbf{M}_\alpha \mathbf{S}_R^{\alpha\dagger} = \mathbf{M}_\alpha^{diag} \quad (\alpha = u, d, e), \quad (2.6)$$

and obtain the mass eigenstates as

$$u_{L(R)}^m = \mathbf{S}_{L(R)}^u u_{L(R)}, \quad d_{L(R)}^m = \mathbf{S}_{L(R)}^d d_{L(R)}, \quad e_{L(R)}^m = \mathbf{S}_{L(R)}^e e_{L(R)}. \quad (2.7)$$

If we were to rewrite the Lagrangian  $\mathcal{L}_{int}$  given in (2.3) in the mass basis, we would find that the change of the basis has no effect on the electromagnetic, neutral and leptonic charged current<sup>1</sup>. For the quark charged current the situation is different. We have

$$J_\mu^+(qk) = \bar{u}_L^i \gamma_\mu d_{L,i} = \bar{u}_L^{m,i} \gamma_\mu S_{L,i}^{u\dagger} S_L^{d,jk} d_{L,k}^m = \bar{u}_L^{m,i} \gamma_\mu V_{ij} d_{L,j}^m, \quad (2.8)$$

<sup>1</sup>For the electromagnetic and neutral current the reason is simple, the matrices  $\mathbf{S}$  are unitary and therefore  $\mathbf{S}\mathbf{S}^\dagger = \mathbf{1}$ . For the leptonic charged current the reason is different, it is due to the fact that within the SM the neutrinos are massless and as such mass degenerate. This allows for the flavor eigenstates to coincide with the mass eigenstates.

---

where we introduce the *Cabibbo-Kobayashi-Maskawa* (CKM) matrix  $\mathbf{V}$ , a unitary matrix that by convention mixes down-type quark mass states to obtain quark states participating in the weak interaction

$$\mathbf{V} \equiv \mathbf{S}_L^{u\dagger} \mathbf{S}_L^d = \begin{pmatrix} V_{ud} & V_{us} & V_{ub} \\ V_{cd} & V_{cs} & V_{cb} \\ V_{td} & V_{ts} & V_{tb} \end{pmatrix}. \quad (2.9)$$

Although a general  $3 \times 3$  unitary matrix has 9 real valued parameters, 3 angles and 6 phases, in the CKM matrix besides the angles only one phase is of physical significance<sup>2</sup>. This irreducible phase introduces CP violation in the SM [4]. Usually it is called the Kobayashi-Maskawa (KM) phase, and as experimentally confirmed, is responsible for all the CP violating phenomena observed so far (or at least it is the main source). By performing CP transformation on  $\mathcal{L}_{int}$  one can show that  $(\mathbf{CP})\mathcal{L}_{int}(\mathbf{CP})^\dagger = \mathcal{L}_{int}^\dagger$ , concluding that CP is conserved if  $\mathcal{L}_{int} = \mathcal{L}_{int}^\dagger$ . In the presence of a complex phase in the CKM matrix this condition does not hold, and therefore CP is violated.

The mechanism described above is one of the two possible ways of breaking CP symmetry within the SM. There are natural terms in the QCD Lagrangian that are able to break CP symmetry. By natural we mean that they are gauge invariant and renormalizable, and that there is no known principle prohibiting their presence. However, experiments do not indicate any CP violation in the QCD sector, limiting the presence of such terms to "unnaturally" tiny values. Why there is no CP violation in the QCD is an open problem, usually referred to as *the strong CP problem* [22].

### 2.0.1 Wolfenstein parametrization

There is no unique parametrization of the CKM matrix in terms of the three rotation angles and one phase. Any scheme that is consistently employed leads to the same physics observables. On the phenomenological grounds the *Wolfenstein parametrization* is particularly useful [23]. It incorporates the experimentally observed hierarchy  $|V_{ub}|^2 \ll |V_{cb}|^2 \ll |V_{us}|^2 \ll 1$ . We define  $\lambda \equiv |V_{us}| \simeq 0.22$ , and expand the elements of the CKM matrix in powers of  $\lambda$  as

$$\mathbf{V} = \begin{pmatrix} 1 - \lambda^2/2 & \lambda & \lambda^3 A(\rho - i\eta) \\ -\lambda & 1 - \lambda^2/2 & \lambda^2 A \\ \lambda^3 A(1 - \rho - i\eta) & -\lambda^2 A & 1 \end{pmatrix}, \quad (2.10)$$

where the real valued parameters  $A$ ,  $\rho$  and  $\eta$  are required to be of the order unity, and the non-zero  $\eta$  introduces the CP violation. Their current experimental values

---

<sup>2</sup>Five phases can be removed by re-phasing the quark fields.

are [24]:

$$\begin{aligned} \lambda &= 0.22535 \pm 0.00065, & A &= 0.811^{+0.022}_{-0.012} \\ \rho &= 0.131^{+0.026}_{-0.013}, & \eta &= 0.345^{+0.013}_{-0.014}. \end{aligned} \quad (2.11)$$

Since the elements of the CKM matrix are free parameters of the SM, it is very intriguing that such an obvious hierarchy is found. It shows that some, yet unknown, mechanism from physics beyond the SM must be at work.

## 2.0.2 Unitarity triangle

As it was already pointed out, the CKM matrix is unitary. This imposes the conditions  $\sum_i V_{ij}V_{ik}^* = \delta_{jk}$  and  $\sum_j V_{ij}V_{kj}^* = \delta_{ik}$  on its elements. The six of the vanishing relations can be presented as triangles in the complex plane, called the *unitarity triangles*. It can be seen from (2.10) that two of these have all three sides of the order  $\lambda^3$ , potentially having all three of their angles large. In this case, the relative weak phases in the quark transitions are of the order unity, inducing large CP asymmetries in some decays. The triangle that is usually used is obtained from

$$V_{ud}V_{ub}^* + V_{cd}V_{cb}^* + V_{td}V_{tb}^* = 0, \quad (2.12)$$

by dividing it with  $V_{cd}V_{cb}^*$ . This results in the triangle with the vertices at  $(0,0)$ ,  $(1,0)$  and  $(\bar{\rho}, \bar{\eta})$ , where  $\bar{\rho} = \rho(1 - \lambda^2/2)$  and  $\bar{\eta} = \eta(1 - \lambda^2/2)$ . The sketch of the unitary triangle, with the defined sides and angles, is given in figure 2.1. The angles are expressed with the CKM matrix elements by

$$\phi_1 = \arg \left[ -\frac{V_{cd}V_{cb}^*}{V_{td}V_{tb}^*} \right], \quad \phi_2 = \arg \left[ -\frac{V_{td}V_{tb}^*}{V_{ud}V_{ub}^*} \right], \quad \phi_3 = \arg \left[ -\frac{V_{ud}V_{ub}^*}{V_{cd}V_{cb}^*} \right]. \quad (2.13)$$

The parameters (sides, angles) of the described triangle can be obtained mainly from the measurements of decay rates and CP asymmetries in the  $B$  meson system. These measurements are of great importance for three reasons: they are measurements of the SM free parameters, they provide an experimental test of CP violation mechanism and the flavor structure of the SM, and some decay modes are sensitive to new physics contributions and provide a way to discover new physics, or at least constrain theoretical models of it.

The current experimental constraints on the position of  $(\bar{\rho}, \bar{\eta})$  from several measurements are summarized in figure 2.2. It is remarkable that the area consistent with all constraints, coming from the measurements of very different processes, exists. This gives a great experimental confirmation of the SM flavor structure.





# 3

## CP violation in $B^0 \rightarrow \eta' K_S^0$ decays

In this chapter we present how CP violation can be observed in the decays of neutral  $B$  mesons into  $\eta'$  and  $K_S^0$  mesons. First we give a brief introduction into the mixing of neutral  $B$  mesons and describe how CP violation can manifest itself in  $B$  meson decays. We then estimate the size of CP violation in the  $B^0 \rightarrow \eta' K_S^0$  decay within the SM, and discuss the connection with new physics. Finally, we conclude with the summary of the past experimental results.

### 3.1 Mixing of neutral $B$ mesons

Unlike the  $\pi^0$  meson, which is its own anti-particle, the neutral  $B$  meson carries an additional quantum number called *bottomness*, allowing a distinction between the  $B^0$  meson and its anti-particle,  $\bar{B}^0$ . Bottomness is a flavor quantum number, defined as  $B' = -(n_b - n_{\bar{b}})$ , where  $n_b$  stands for the number of bottom quarks, and  $n_{\bar{b}}$  for the number of bottom anti-quarks.  $B^0$  ( $d\bar{b}$ ) meson has  $B' = 1$ , and  $\bar{B}^0$  ( $db$ ) meson has  $B' = -1$ . As other flavor quantum numbers, bottomness is conserved by the electromagnetic and strong interaction, while the weak interaction varies it for  $\Delta B' = \pm 1$  (in 1st order processes, i.e. processes involving a single quark). However, in processes of the 2nd order in the weak interaction, there is also a possibility of transitions with  $\Delta B' = \pm 2$ . In the SM these transitions are in the lowest order given by so-called *box diagrams*, as shown in figure 3.1. These diagrams connect the  $B^0$  and  $\bar{B}^0$  states, and give rise to the phenomenon called  $B^0 - \bar{B}^0$  *mixing*. If, for example, we produce a pure  $B^0$  state, as this state propagates in time, it will gain a component of the  $\bar{B}^0$  state.

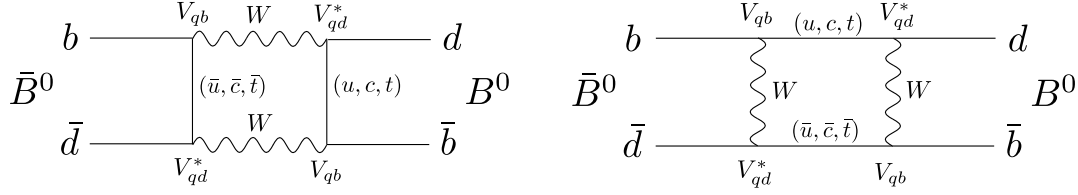


Figure 3.1: Feynman diagrams responsible for  $\Delta B' = 2$  transitions,  $B - \bar{B}$  mixing, usually called box diagrams.

Phenomenologically we can describe and obtain the time evolution of mixing of neutral mesons through a simple quantum mechanical reasoning. We describe the  $B^0 - \bar{B}^0$  system with a vector in a Hilbert space

$$|\Psi(t)\rangle = a(t)|B^0\rangle + b(t)|\bar{B}^0\rangle. \quad (3.1)$$

Its time evolution is given by the Schrödinger equation with the effective Hamiltonian  $\mathcal{H}$

$$i\hbar \frac{\partial}{\partial t} |\Psi(t)\rangle = \mathcal{H} |\Psi(t)\rangle, \quad (3.2)$$

where in the  $|B^0\rangle, |\bar{B}^0\rangle$  basis

$$|\Psi(t)\rangle = \begin{pmatrix} a(t) \\ b(t) \end{pmatrix}, \quad \text{and } \mathcal{H} = \mathbf{M} - \frac{i}{2}\mathbf{\Gamma} = \begin{pmatrix} M_{11} - \frac{i}{2}\Gamma_{11} & M_{12} - \frac{i}{2}\Gamma_{12} \\ M_{21} - \frac{i}{2}\Gamma_{21} & M_{22} - \frac{i}{2}\Gamma_{22} \end{pmatrix}. \quad (3.3)$$

In (3.3) we decomposed  $\mathcal{H}$  into the *mass matrix*  $\mathbf{M}$  and the *decay matrix*  $\mathbf{\Gamma}$ , both of which are hermitian matrices. In addition to the hermicity condition, giving  $M_{12} = M_{21}^*$  and  $\Gamma_{12} = \Gamma_{21}^*$ , the CPT invariance<sup>1</sup> constrains the diagonal elements to  $M_{11} = M_{22}$  and  $\Gamma_{11} = \Gamma_{22}$ . The non-diagonal parts of  $\mathbf{M}$  and  $\mathbf{\Gamma}$  come from the dispersive and absorptive parts of box diagrams, and can be calculated within the SM [27]. The light (L) and heavy (H) mass eigenstates of the theory, obtained by diagonalization of  $\mathcal{H}$ , are

$$|B_L\rangle = p|B^0\rangle + q|\bar{B}^0\rangle, \quad (3.4)$$

$$|B_H\rangle = p|B^0\rangle - q|\bar{B}^0\rangle, \quad (3.5)$$

with eigenvalues

$$M_L - \frac{i}{2}\Gamma_L = M_{11} - \frac{i}{2}\Gamma_{11} + \frac{q}{p} \left( M_{12} - \frac{i}{2}\Gamma_{12} \right), \quad (3.6)$$

$$M_H - \frac{i}{2}\Gamma_H = M_{22} - \frac{i}{2}\Gamma_{22} - \frac{q}{p} \left( M_{12} - \frac{i}{2}\Gamma_{12} \right), \quad (3.7)$$

<sup>1</sup>CPT theorem [26] assures that any Lorentz invariant local quantum field theory with a hermitian Hamiltonian is CPT invariant.

where  $q/p$  is given by

$$\frac{q}{p} = \sqrt{\frac{M_{12}^* - \frac{i}{2}\Gamma_{12}^*}{M_{12} - \frac{i}{2}\Gamma_{12}}}. \quad (3.8)$$

In the SM, the quantity  $|\Gamma_{12}/M_{12}| \sim \mathcal{O}(m_b^2/m_t^2)$  is very small ( $\lesssim \mathcal{O}(10^{-3})$ ) [28] and  $M_{12} \propto V_{td}^* V_{tb}$  [27], resulting in

$$\frac{q}{p} \simeq \frac{V_{td}^* V_{tb}}{V_{td} V_{tb}^*}, \quad \text{and therefore} \quad \left| \frac{q}{p} \right| \simeq 1. \quad (3.9)$$

Knowing the time evolution of the mass eigenstates  $|B_L\rangle$  and  $|B_H\rangle$  (i.e.  $|B_{L,H}(t)\rangle = |B_{L,H}\rangle e^{-i(M_{L,H} - i\Gamma_{L,H}/2)t}$ ), and taking into account (3.5), one can easily obtain how an initially produced pure  $B^0$  ( $\bar{B}^0$ ) state, denoted as  $|B^0(t)\rangle$  ( $|\bar{B}^0(t)\rangle$ ), evolves in time

$$|B^0(t)\rangle = f_+(t)|B^0\rangle + \frac{q}{p}f_-(t)|\bar{B}^0\rangle, \quad (3.10)$$

$$|\bar{B}^0(t)\rangle = f_+(t)|\bar{B}^0\rangle + \frac{p}{q}f_-(t)|B^0\rangle. \quad (3.11)$$

Here we introduced

$$f_{\pm}(t) = \frac{1}{2}e^{-iMt - \frac{1}{2}\Gamma t} \left[ 1 \pm e^{-i\Delta Mt + \frac{1}{2}\Delta\Gamma t} \right], \quad (3.12)$$

with the  $B$  meson mass  $M \equiv (M_L + M_H)/2$ , decay width  $\Gamma \equiv (\Gamma_L + \Gamma_H)/2$ , mixing frequency  $\Delta M \equiv M_H - M_L$ , and the width difference  $\Delta\Gamma = \Gamma_L - \Gamma_H$ . As the initial  $B^0$  (or  $\bar{B}^0$ ) state evolves in time, it oscillates between the  $B^0$  and  $\bar{B}^0$  states with the frequency  $\Delta M$ . Luckily, the value of the mixing parameter  $x = \Delta M/\Gamma$  (giving the number of oscillations in a lifetime) is of order unity in the  $B$  meson system (exp.  $x = 0.77 \pm 0.01$  [29]), allowing the oscillations to be experimentally observed. In addition, it can be seen from (3.6) and (3.7) that  $\Delta\Gamma \ll \Delta M$ , since  $|\Gamma_{12}/M_{12}| \lesssim \mathcal{O}(10^{-3})$ , and from  $\Delta M/\Gamma \sim 1$  it follows that  $\Delta\Gamma \ll \Gamma$ . Unlike in the kaon system, the decay width difference between the two mass states is very small here.

### 3.1.1 Decay rates

What we can measure in the experiments are the decay rates. Therefore we ask ourselves at which rate an initially produced  $B^0$  (or  $\bar{B}^0$ ) state decays into some final state  $f$ . Clearly the decay rate  $\Gamma(B^0(t) \rightarrow f)$  is time dependent, since the  $B^0(t)$  state is a time dependent superposition of the  $B^0$  and  $\bar{B}^0$  states. We denote the decay amplitudes of flavor eigenstates  $B^0$  and  $\bar{B}^0$  decaying into  $f$  with  $A_f = \langle f|B^0\rangle$  and  $\bar{A}_f = \langle f|\bar{B}^0\rangle$ , and define the parameter

$$\lambda_f \equiv \frac{1}{\bar{\lambda}_f} \equiv \frac{q}{p} \frac{\bar{A}_f}{A_f}. \quad (3.13)$$

The decay rates can be obtained from the equations (3.10) and (3.11) by  $\Gamma(B^0(t) \rightarrow f) = |\langle f | B^0(t) \rangle|^2$ , yielding

$$\Gamma(B^0(t) \rightarrow f) \propto e^{-\Gamma t} |A_f|^2 [K_+(t) + K_-(t) |\lambda_f|^2 + 2\text{Re}(L(t)\lambda_f)], \quad (3.14)$$

$$\Gamma(\bar{B}^0(t) \rightarrow f) \propto e^{-\Gamma t} |\bar{A}_f|^2 [K_+(t) + K_-(t) |\bar{\lambda}_f|^2 + 2\text{Re}(L(t)\bar{\lambda}_f)], \quad (3.15)$$

with

$$K_{\pm}(t) = 1 + e^{\Delta\Gamma t} \pm 2e^{\frac{1}{2}\Delta\Gamma t} \cos \Delta Mt, \quad (3.16)$$

$$L(t) = 1 - e^{\Delta\Gamma t} + 2ie^{\frac{1}{2}\Delta\Gamma t} \sin \Delta Mt. \quad (3.17)$$

From (3.14) and (3.15) one can see that in the case when both  $B^0$  and  $\bar{B}^0$ , can decay into the same final state  $f$  (i.e.  $\lambda_f, \bar{\lambda}_f \neq 0$ ), the decay rate consists of three terms. The first one representing a decay of  $B^0$ , second one a decay of the  $\bar{B}^0$  component arising through mixing, and the third one representing the interference between these two possible decays.

## 3.2 CP violation in neutral $B$ meson decays

To measure CP violation, we measure the asymmetry between the decays of  $B^0(t)$  and  $\bar{B}^0(t)$  into the CP conjugated final states,  $f$  and  $\bar{f}$ . Since the decay rates of the neutral  $B$  mesons are time dependent, the asymmetry also depends on time, and is defined by

$$a_f(t) \equiv \frac{\Gamma(B^0(t) \rightarrow f) - \Gamma(\bar{B}^0(t) \rightarrow \bar{f})}{\Gamma(B^0(t) \rightarrow f) + \Gamma(\bar{B}^0(t) \rightarrow \bar{f})}. \quad (3.18)$$

By carefully examining the equations (3.14) and (3.15) one can find three extreme cases in which  $a_f$  differs from zero, but for different reasons [30]. In general, all three of them can contribute, depending on the decay final state  $f$ .

- CP is most obviously violated if  $|A_f| \neq |\bar{A}_f|$ , and therefore  $\Gamma(B^0(t) \rightarrow f) \neq \Gamma(\bar{B}^0(t) \rightarrow \bar{f})$ . This is called *direct* CP violation. It is independent of the  $B^0 - \bar{B}^0$  mixing effects and can also be observed in the decays of charged  $B$  mesons.
- Another possibility is found by studying flavor specific decays, i.e. decays with such final state  $f$  ( $\bar{f}$ ), that only the  $B^0$  ( $\bar{B}^0$ ) flavor eigenstate can decay into. The most prominent examples of these are semileptonic decays. In this case  $\bar{A}_f = 0$  and  $A_{\bar{f}} = 0$ . If, in addition, we demand that there is no direct CP violation in the selected decay ( $|A_f| = |\bar{A}_f|$ ), the equations (3.14) and (3.15) yield the asymmetry

$$a_f = \frac{1 - |p/q|^4}{1 + |p/q|^4}, \quad (3.19)$$

which is time independent and differs from zero if  $|\frac{q}{p}| \neq 1$ . However, as given in (3.9),  $\frac{q}{p}$  is in close approximation a pure phase, making this asymmetry too small to be experimentally observed so far. Its current experimental value from semileptonic  $B$  decays is  $a_{SL} = (-3.3 \pm 3.3) \times 10^{-3}$  [24]. This type of CP violation is called CP violation in mixing.

- The third way in which CP violation can manifest itself, can be observed in decays into flavor non-specific final states, i.e. states into which both  $B^0$  and  $\bar{B}^0$  can decay. Decays into CP eigenstates are obviously of this type ( $f = \bar{f}$ ). Beginning with a general case, we allow for the  $B^0$  and  $\bar{B}^0$  to have different amplitudes to decay into  $f$  ( $|A_f| \neq |\bar{A}_f|$ ). First we can simplify the decay rates, as given in (3.14) and (3.15), by taking into account that  $\Delta\Gamma \ll \Gamma$  and the definition of  $\lambda_f$  and  $\bar{\lambda}_f$  (3.13)

$$\Gamma(B^0(t) \rightarrow f) \propto e^{-\Gamma t} |A_f|^2 \left[ 1 + \frac{1 - |\lambda_f|^2}{1 + |\lambda_f|^2} \cos \Delta Mt - \frac{2\text{Im}\lambda_f}{1 + |\lambda_f|^2} \sin \Delta Mt \right] \quad (3.20)$$

$$\Gamma(\bar{B}^0(t) \rightarrow f) \propto e^{-\Gamma t} |A_f|^2 \left[ 1 - \frac{1 - |\lambda_f|^2}{1 + |\lambda_f|^2} \cos \Delta Mt + \frac{2\text{Im}\lambda_f}{1 + |\lambda_f|^2} \sin \Delta Mt \right]. \quad (3.21)$$

From this and the definition of asymmetry  $a_f(t)$  (3.18) we then obtain

$$a_f(t) = \mathcal{A}_f \cos \Delta Mt + \mathcal{S}_f \sin \Delta Mt, \quad (3.22)$$

where we have introduced two so-called *CP violation parameters* (commonly we will use "CPV parameters" notation) given by

$$\mathcal{A}_f = \frac{|\lambda_f|^2 - 1}{|\lambda_f|^2 + 1}, \quad \mathcal{S}_f = \frac{2\text{Im}\lambda_f}{1 + |\lambda_f|^2}. \quad (3.23)$$

Remembering that  $\lambda_f = \frac{q}{p} \frac{\bar{A}_f}{A_f}$  and  $|\frac{q}{p}| \simeq 1$ , we can see that the first term in (3.22) is due to direct CP violation, since  $\mathcal{A}_f \neq 0$  only if  $|A_f| \neq |\bar{A}_f|$ . However, the second term in (3.22) is something new and represents CP violation in the interference between the direct  $B^0 \rightarrow f$  and mixed  $B^0 \rightarrow \bar{B}^0 \rightarrow f$  decay. This second term can be non-zero even in the case when  $|q/p| = 1$  and also  $|A_f| = |\bar{A}_f|$  holds, as then  $\mathcal{S}_f = \sin[\arg(q/p) + \arg(\bar{A}_f/A_f)]$ . Measuring the asymmetry (3.22), and consequently the parameter  $\mathcal{S}_f$ , therefore allows us to measure a sum of CP violating phases in mixing and decay.

### 3.3 CP violation in $B^0 \rightarrow \eta' K_S^0$

Neutral  $B^0$  and  $\bar{B}^0$  meson can both decay into  $\eta' K_S^0$  final state, since this state is a CP eigenstate (if a tiny CP odd component of  $K_S^0$  is neglected). Strictly speaking, in terms of the flavor eigenstates,  $B^0$  decays into  $\eta' K^0$  and  $\bar{B}^0$  into  $\eta' \bar{K}^0$ , and the common final state is then reached by  $K^0 - \bar{K}^0$  mixing. On the quark level, this decay proceeds through  $b \rightarrow s\bar{q}q$  ( $q = d, s$ ) transition, which is an example of flavor changing neutral transition (quarks  $b$  and  $s$  have the same charge). In the SM these are not allowed at the tree level, but can happen via penguin diagrams, as shown in figure 3.2. There also exists a tree level diagram with  $b \rightarrow u$  transition that contributes to the decay, shown in figure 3.3, but it is CKM suppressed by  $\lambda^2$  and also color suppressed, giving less than a few percent contribution.

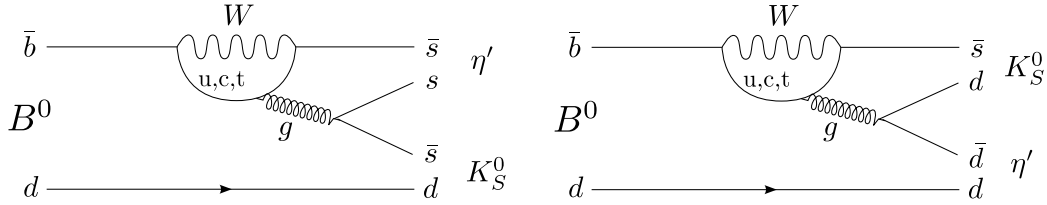


Figure 3.2: Feynman diagrams contributing to the  $B^0 \rightarrow \eta' K_S^0$  decay. The diagrams for  $\bar{B}^0$  decay can be obtained by changing  $q \rightarrow \bar{q}$ .

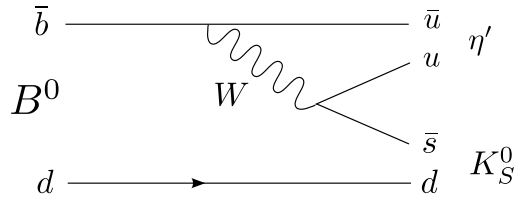


Figure 3.3: Tree level Feynman diagram contributing to the  $B^0 \rightarrow \eta' K_S^0$  decay. It is CKM (by  $\lambda^2$ ) and color suppressed compared to the penguin diagrams from figure 3.2.

CP violation in  $B^0 \rightarrow \eta' K_S^0$  clearly belongs to the third type presented in section 3.2, resulting in the time dependent asymmetry

$$a_{\eta' K_S^0}(t) = \mathcal{A}_{\eta' K_S^0} \cos \Delta M t + \mathcal{S}_{\eta' K_S^0} \sin \Delta M t. \quad (3.24)$$

To obtain the SM prediction for the values of  $\mathcal{A}_{\eta' K_S^0}$  and  $\mathcal{S}_{\eta' K_S^0}$ , we need to calculate the ratio of the amplitudes  $\bar{A}_{\eta' K_S^0} / A_{\eta' K_S^0}$ . Both of the amplitudes can be written as a sum of three amplitudes of penguin diagrams, with quarks  $u, c, t$  in the loop. With the use of CKM unitarity we can eliminate one of the three CKM combinations and

write

$$\frac{\bar{A}_{\eta'K_S^0}}{A_{\eta'K_S^0}} = -\frac{(V_{cb}V_{cs}^*)(p^c - p^t) + (V_{ub}V_{us}^*)(p^u - p^t)}{(V_{cb}^*V_{cs})(p^c - p^t) + (V_{ub}^*V_{us})(p^u - p^t)} \times \frac{V_{cd}^*V_{cs}}{V_{cd}V_{cs}^*}, \quad (3.25)$$

where  $p^c, p^u, p^t$  are the amplitudes of penguin diagrams with  $u, c, t$  quarks excluding the CKM elements, and the last factor accounts for the phase in  $K^0 - \bar{K}^0$  mixing, that provides  $K_S^0$  in the final state. The minus sign in (3.25) comes from  $\mathbf{CP}(\eta'K_S^0) = -1(\eta'K_S^0)$ . The second term of the sum in the numerator and denominator of (3.25) is suppressed by  $\lambda^2$  compared to the first, and can be neglected (to a few % level). With the use of (3.9) and (3.13) we obtain

$$\lambda_{\eta'K_S^0} = \frac{q}{p} \frac{\bar{A}_{\eta'K_S^0}}{A_{\eta'K_S^0}} \simeq -\frac{V_{tb}^*V_{td}}{V_{tb}V_{td}^*} \frac{V_{cd}^*V_{cb}}{V_{cd}V_{cb}^*} = -e^{-2i\phi_1}, \quad (3.26)$$

where  $\phi_1$  is one of the unitarity triangle angles, as defined in (2.13). Finally with (3.23) we conclude that

$$\mathcal{A}_{\eta'K_S^0} \simeq 0, \quad \mathcal{S}_{\eta'K_S^0} \simeq \sin 2\phi_1. \quad (3.27)$$

Thanks to the CKM suppression of the second term in the sums of (3.25), we have a very clean interpretation of CP violation parameters. It is accurate to a few percent and free of large theoretical uncertainties in the penguin amplitudes (unlike for example the  $B^0 \rightarrow \eta'K_S^0$  branching fraction). Several theoretical approaches were used to estimate the contributions of the CKM and color suppressed amplitudes, neglected in the above derivation, to the value of  $\mathcal{S}_{\eta'K_S^0}$ . They provide bounds on possible deviation of  $\mathcal{S}_{\eta'K_S^0}$  from  $\sin 2\phi$  within the SM. For example, from QCD factorization  $\mathcal{S}_{\eta'K_S^0} - \sin 2\phi$  is in the range  $(-0.03, 0.03)$  [15–17], while using  $SU(3)$  relations constrains it to  $(-0.05, 0.09)$  [18]. Related calculations are also presented in [19–21].

### 3.3.1 New physics search

As it was shown in the previous section, the amplitude of asymmetry  $a_{\eta'K_S^0}(t)$  is within the SM given by  $\sin 2\phi_1$ . However, the primary importance of measuring this asymmetry is not to determine  $\sin 2\phi_1$ , but its sensitivity to new physics.

The value of  $\sin 2\phi_1$  can be much more accurately measured in the famed  $B^0 \rightarrow J/\psi K_S^0$  and other  $b \rightarrow c\bar{c}s$  quark transition dominated decays. The main contribution to the amplitudes of these decays is the tree level amplitude of the diagram shown in figure 3.4. There is also a penguin contribution to the decay, but it is suppressed compared to the tree amplitude by "loop  $\times \lambda^2$ ", where "loop" refers to a penguin versus tree suppression, which is  $\sim 0.2$  in this case [31]. The CKM part of the tree amplitude is given by  $V_{cb}^*V_{cs}$ , which is the same as in the  $B \rightarrow \eta'K_S^0$  penguin diagram. Therefore we again obtain

$$\mathcal{A}_{J/\psi K_S^0} \simeq 0, \quad \mathcal{S}_{J/\psi K_S^0} \simeq \sin 2\phi_1, \quad (3.28)$$

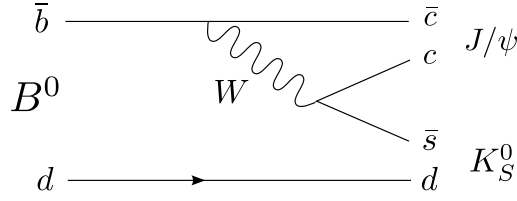


Figure 3.4: Tree level Feynman diagram of  $B^0 \rightarrow J/\psi K_S^0$  decay. The diagram for  $\bar{B}^0$  decay can be obtained by changing  $q \rightarrow \bar{q}$ .

which holds to better than 1%, due to the additional "loop" suppression of the penguin diagram [31].

In the presence of new physics, new heavy particles in the loops of the penguin diagrams can contribute to decay amplitudes, and potentially also carry additional weak phases. Regarding  $B^0 \rightarrow J/\psi K_S^0$  decay, the tree dominated amplitude  $A_{J/\psi K_S^0}$  is unlikely to be significantly modified, but the mixing amplitude, governed by box diagrams, might be. This would result in the inconsistencies between the measured values of  $\mathcal{S}_{J/\psi K_S^0}$  and predictions for  $\sin 2\phi_1$  as inferred from  $\Delta M_B, |V_{ub}/V_{cb}|$  and measurements in the kaon system. For  $B^0 \rightarrow \eta' K_S^0$  decay the situation is different. Here, beside the mixing amplitude, the amplitude  $A_{\eta' K_S^0}$  is also dominated by a loop diagram and new particles in loops can bring contributions that are comparable to those of the SM penguin [13]. In this case, the value of  $\mathcal{S}_{\eta' K_S^0}$  can differ greatly from the value of  $\mathcal{S}_{J/\psi K_S^0}$ . Observing the difference  $|\mathcal{S}_{\eta' K_S^0} - \mathcal{S}_{J/\psi K_S^0}|$  to be larger than a few percent (potentially also  $\mathcal{A}_{\eta' K_S^0}$  to differ from zero more than few percent) would be a model independent sign of new physics. If, on the other hand, the difference is not observed, this can be used to constrain the parameter space of several new physics models, in which new CP violating phases arise naturally [32].

### 3.3.2 Summary of previous experimental results

Measuring the time dependent CP violation in  $B^0 \rightarrow J/\psi K_S^0$  (expected to be large within the SM) was the main motivation for the construction of  $B$  factories. Already in the first years of their operation (in 2001) the Belle and BaBar collaborations reported the value of  $\sin 2\phi_1 \sim 1$ , consistent with the SM prediction, confirming the Kobayashi-Maskawa phase as the main source of CP violation in the  $B$  meson system [7,8]. Even today, after the accumulation of huge amount of  $B$  meson decays by Belle and BaBar, the value of  $\sin 2\phi_1$  is remarkably consistent with the SM expectations [33,34], as can be seen from the unitarity triangle in figure 2.2.

Soon after the value of  $\sin 2\phi_1$  was settled, the attention turned to the measurements of CP violation in charmless  $b \rightarrow s\bar{q}q$  penguin dominated decays. There are quite a few  $B^0$  decays of this kind, with  $B^0 \rightarrow \eta' K_S^0$  being preferred from the experimental point of view, having the largest branching fraction. These measurements have written an interesting chapter in the history of  $B$  factories. In the early years

(around 2004), some decay modes were showing significant deviations from  $\sin 2\phi_1$ , with the average of all measured  $b \rightarrow s\bar{q}q$  modes being more than  $3\sigma$  off (at that time  $\sin 2\phi = 0.725 \pm 0.037$ , and  $\mathcal{S}_{b \rightarrow s\bar{q}q} = 0.41 \pm 0.07$  [29]). The value of  $\mathcal{S}$  was lower than  $\sin 2\phi_1$  for practically all measured modes which was very intriguing, especially because the theoretical studies of higher order corrections within SM show  $\mathcal{S}_{b \rightarrow s\bar{q}q} > \sin 2\phi_1$ . The discrepancy was very persistent, staying at more than  $2\sigma$  level until 2008. Later the situation softened and today there is less than  $1\sigma$  discrepancy. In figure 3.5, the experimental results of CP violation parameters in  $b \rightarrow s\bar{q}q$  modes are shown, as of summer 2012. The rather large error bars of these measurements are however still leaving some space for possible new physics contributions. Since the uncertainties are statistically dominated, a larger data sample of recorded  $B$  meson decays is needed to clarify the situation.

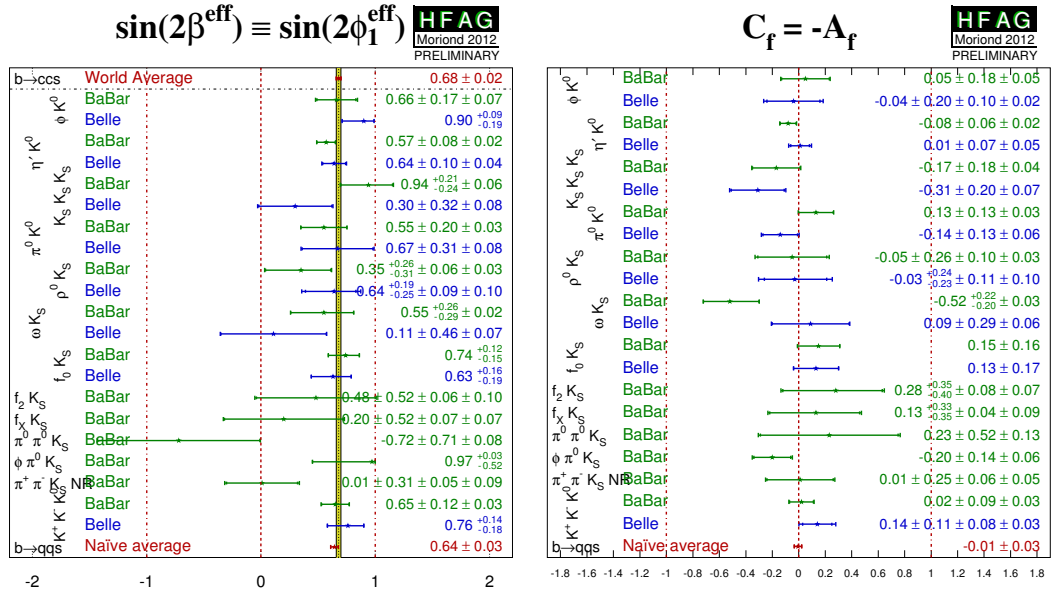


Figure 3.5: Summary of measurements of the CP violation parameters in  $b \rightarrow s\bar{q}q$  transition dominated decays, as of 2012. Left plot shows the values of  $\mathcal{S}_f$ , usually also denoted as  $\sin 2\phi_1^{\text{eff}}$ . The world average value of  $\sin 2\phi_1$  from  $b \rightarrow c\bar{c}s$  decays is shown as the yellow band. On the right, the values of parameter  $-\mathcal{A}_f$  are shown [29].

For CP violation in  $B^0 \rightarrow \eta' K_S^0$  decay, the latest measurements were done by Belle in 2007 [35] and BaBar in 2009 [36]. Belle used data sample with  $535 \times 10^6$  and BaBar with  $467 \times 10^6$  recorded  $B\bar{B}$  pair decays. The results are summarized in table 3.1, where we also give the results for  $B^0 \rightarrow \eta' K^0$  which combines  $B^0 \rightarrow \eta' K_S^0$  and  $B^0 \rightarrow \eta' K_L^0$  results<sup>2</sup>.

<sup>2</sup>For  $B^0 \rightarrow \eta' K_L^0$  decay the predicted CP violation is the same as for  $B^0 \rightarrow \eta' K_S^0$ .

	$\mathcal{S}$	$\mathcal{A}$
<hr/>		
$B \rightarrow \eta' K_S^0$		
Belle	$0.67 \pm 0.11 \pm 0.04$	$-0.03 \pm 0.07 \pm 0.05$
BaBar	$0.53 \pm 0.08 \pm 0.02$	$+0.11 \pm 0.06 \pm 0.02$
<hr/>		
$B \rightarrow \eta' K^0$		
Belle	$0.64 \pm 0.10 \pm 0.04$	$-0.01 \pm 0.07 \pm 0.05$
BaBar	$0.57 \pm 0.08 \pm 0.02$	$+0.08 \pm 0.06 \pm 0.02$
Average	$0.60 \pm 0.07$	$+0.05 \pm 0.05$
<hr/>		
$B \rightarrow c\bar{c}K_S^0$	$0.68 \pm 0.02$	$-0.01 \pm 0.02$

Table 3.1: Current experimental values of CP violation parameters in  $B^0 \rightarrow \eta' K_S^0$ . The first uncertainties are statistical and the second are systematic. Also the values for combined fit of  $B^0 \rightarrow \eta' K_S^0$  and  $B^0 \rightarrow \eta' K_L^0$  data are given, and the world average value of  $\sin 2\phi_1$  [29, 35, 36].

# 4

## Principle of measurement

In this chapter we present the basic principles of measuring time dependent CP asymmetry at  $B$  factories.

To obtain the asymmetry  $a_{\eta'K_S^0}(t)$  as given in (3.18), we need to measure the difference between the time dependent decay rates of states  $B^0(t)$  and  $\bar{B}^0(t)$  into the final state  $\eta'K_S^0$ . This means that we need to select  $B$  mesons that were in pure flavor eigenstate at time  $t = 0$ , determine their flavor at that time ( $B^0$  or  $\bar{B}^0$ ), and measure the time distribution of their decays into  $\eta'K_S^0$ . The difference between the distributions of the initial  $B^0$  and  $\bar{B}^0$  states gives the asymmetry  $a_{\eta'K_S^0}(t)$ , that allows us to extract the values of  $\mathcal{A}_{\eta'K_S^0}$  and  $\mathcal{S}_{\eta'K_S^0}$ .

After many conceptual insights it was realized by the late 1980s that measuring the time dependent asymmetries, as described above, is experimentally possible. This resulted in the construction of two novel experiments, so-called  $B$  factories, in the 1990s. One being the KEKB/Belle [5, 37] and the other PEP-II/BaBar [6] accelerator and detector complexes. In the following we describe four main principles utilized by  $B$  factories, that have enabled to perform such measurements.

- Collisions of electrons and positrons provide a clean environment for studying  $B$  physics. At  $B$  factories, the center of mass energy of colliding electron and positron beams is tuned to the mass<sup>1</sup> of  $\Upsilon(4S)$  resonance (10.58 GeV), which is just above the threshold for  $B\bar{B}$  ( $B^0\bar{B}^0$  or  $B^+B^-$ ) pair production. It decays in almost 100% to a  $B\bar{B}$  pair, and this pair is practically at rest in the  $\Upsilon(4S)$  center of mass system (CMS). Due to almost equal mass of charged and neutral  $B$  mesons they are produced in almost equal measure.

---

<sup>1</sup>Throughout this work we use a system of natural units, with  $c$  set to 1. See appendix B.1.

- The  $B\bar{B}$  meson pair from  $Y(4S)$  decay is produced in a quantum coherent state. The mesons then undergo  $B^0 - \bar{B}^0$  mixing and both gain a component of the opposite flavor, but the coherence between the two is preserved until one meson decays. If we observe one of them, lets call it  $B_{tag}$ , to decay into a flavor specific final state (i.e. a final state into which only  $B^0$  or  $\bar{B}^0$  can decay) at some time  $t_{tag}$ , this means that at this time its wave function collapsed into a flavor eigenstate. By quantum coherence we know that the other  $B$  meson of a pair, lets call it  $B_{CP}$ , was in the opposite flavor eigenstate at time  $t_{tag}$ . From then on,  $B_{CP}$  evolves as  $B^0(t - t_{tag})$  if  $B_{tag}$  decayed into  $\bar{B}^0$  specific state, and as  $\bar{B}^0(t - t_{tag})$  if  $B_{tag}$  decayed into  $B^0$  specific state. One then reconstructs  $B_{CP}$  decay into  $\eta'K_S^0$  at time  $t_{tag} + \Delta t$ , and since its flavor at  $t_{tag}$  is known, we are able to obtain the decay rates  $\Gamma(B^0(\Delta t) \rightarrow \eta'K_S^0)$  and  $\Gamma(\bar{B}^0(\Delta t) \rightarrow \eta'K_S^0)$ , as given in (3.20) and (3.21). We are therefore also able to obtain the asymmetry  $a_{\eta'K_S^0}(\Delta t)$ . Note that the same expressions for the decay rates (3.20),(3.21) can be applied also when  $B_{CP}$  decays at time  $\Delta t$  before  $B_{tag}$  decays, resulting in a negative  $\Delta t$ .
- The use of asymmetric beam energies at  $B$  factories allows to infer  $\Delta t$  from the spatial distance between the decay vertices of  $B_{tag}$  and  $B_{CP}$ . At the KEKB collider, the electron beam energy is 8 GeV, while the positron beam energy is 3.5 GeV. The resulting  $Y(4S)$  resonance is boosted along the beam direction with the boost factor  $\gamma\beta = 0.425$ . The already mentioned fact that a  $B$  meson pair is practically at rest in the  $Y(4S)$  CMS, gives an easy conversion between the spatial and temporal distance between the decay vertices

$$\Delta t \simeq \frac{\Delta z}{\gamma\beta c}, \quad (4.1)$$

where  $\Delta z$  is the distance between the vertices in the beam direction<sup>2</sup>. With the  $B$  meson lifetime  $\tau_{B^0} \sim 1.5$  ps,  $|\Delta z| = \gamma\beta c\tau_B$  is about 200  $\mu\text{m}$ . To measure the time dependent CP violation  $\Delta z$  has to be determined with the resolution of about 200  $\mu\text{m}$ , or better.

- To measure the time dependent asymmetries in decays with the branching fraction  $\mathcal{O}(10^{-5})$ , a large number of  $B$  mesons is needed. For this reason, the  $B$  factories were designed as very high luminosity machines, with the KEKB holding world record at peak luminosity of  $2 \times 10^{34} \text{ s}^{-1}\text{cm}^{-2}$ .

---

<sup>2</sup>The distance traveled by  $B$  meson in a plane perpendicular to the beam direction is small and taken into account in the resolution function as described later.

The described principle of measurement is summarized in figure 4.1 and it offers a strategy to measure  $a_{\eta'K_S^0}(\Delta t)$ . We therefore need to:

1. determine (tag) the flavor of one of the  $B$  mesons ( $B_{tag}$ ),
2. reconstruct its associated  $B$  meson ( $B_{CP}$ ) decaying into  $\eta'K_S^0$ ,
3. measure the distance between the decay vertices of  $B_{tag}$  and  $B_{CP}$ , and
4. extract the values of CPV parameters from the obtained decay time distributions.

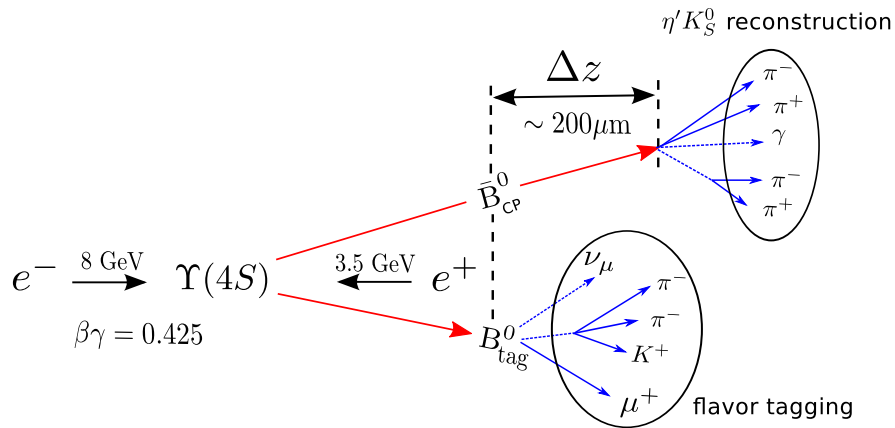


Figure 4.1: Principle of time dependent CP violation measurement at  $B$  factories.

## 4.1 From principle to reality

The principle presented in the previous section is nice, but the real world is not ideal. Each of the points given before has a caveat that we must be aware of, and these are discussed in the following text.

### 1. Flavor tagging

The determination of  $B_{tag}$  flavor is based on its relation to the charge of the decay products. If, for example, we find a high momentum positively (negatively) charged kaon among the decay products, we conclude that the decay proceeded through  $\bar{b} \rightarrow \bar{c} \rightarrow \bar{s}$  ( $b \rightarrow c \rightarrow s$ ) quark conversion, and that the decaying particle was  $B^0$  ( $\bar{B}^0$ ). But this is not always true due to possible particle misidentification (experimentally we only know the probability that particle was a kaon), or maybe the kaon came from some other rarer process. Having a detector with good particle identification

systems is crucial for efficient flavor tagging. Presence of wrongly tagged  $B$  mesons dilutes the asymmetry  $a_{\eta'K_S^0}$ , as given in (3.24), to

$$a_{\eta'K_S^0}^{wt}(\Delta t) = (1 - 2w)a_{\eta'K_S^0}(\Delta t) - \Delta w, \quad (4.2)$$

where  $w = (w_{B^0} + w_{\bar{B}^0})/2$  and  $\Delta w = w_{B^0} - w_{\bar{B}^0}$ , with  $w_{B^0}$  ( $w_{\bar{B}^0}$ ) being the fraction of wrongly tagged  $B^0$  ( $\bar{B}^0$ ) mesons.

## 2. Decay reconstruction

Experimentally, we can only detect particles that live long enough to produce signals in tracking detectors (charged particles) or calorimeters (neutral particles). For  $B \rightarrow \eta'K_S^0$  decay these particles are charged pions and photons. They come either from the decay of  $\eta'$ , that decays immediately at the interaction point<sup>3</sup>, or from the  $K_S^0$  decay, which can happen a few cm from the interaction point due to relatively long lifetime of  $K_S^0$  ( $\sim 10^{-10}$  s). To reconstruct the  $B \rightarrow \eta'K_S^0$  decay, we take the decay final state particles and combine them to first obtain the intermediate states and finally the  $B$  meson candidate. Several conditions are imposed in the reconstruction to select as many signal candidates as possible (i.e.  $B^0$  mesons that have actually decayed into  $\eta'K_S^0$ ), while keeping the amount of background candidates (all non signal candidates) as low as possible. But since we always have some irreducible fraction of background candidates, this dilutes the asymmetry  $a_{\eta'K_S^0}$  to

$$a_{\eta'K_S^0}^{bg}(\Delta t) = f_{sig}a_{\eta'K_S^0}(\Delta t), \quad (4.3)$$

where  $f_{sig}$  is the fraction of signal candidates among all reconstructed candidates (and we assume that background candidates possess no asymmetry).

## 3. Decay vertex reconstruction

In reality, we can only determine the time difference  $\Delta t$  with finite precision. The decay vertex position is mainly determined by the number and position of charged particle hits (in our case pions from  $\eta'$  decay) in the detector closest to the interaction point. The detector has finite granularity and is placed at some distance from the interaction point. The fact that a  $B$  meson pair is only approximately at rest in the Y(4S) CMS also limits the precision of determining  $\Delta t$ . The effect of finite  $\Delta t$  resolution on the asymmetry  $a_{\eta'K_S^0}$  can be written as

$$a_{\eta'K_S^0}^{rf}(\Delta t) = a_{\eta'K_S^0}(\Delta t) \otimes \mathcal{R}(\Delta t), \quad (4.4)$$

where  $\mathcal{R}(\Delta t)$  is the detector  $\Delta t$  resolution function, and  $\otimes$  denotes convolution.

---

<sup>3</sup>Lifetime of  $\eta'$  is about  $10^{-21}$  s.

---

#### 4. Extraction of CP violating parameters

Neglecting the discussed experimental effects, we are able to extract the values of the CPV parameters,  $\mathcal{A}_{\eta'K_S^0}$  and  $\mathcal{S}_{\eta'K_S^0}$ , by fitting the following probability density function (PDF), obtained from the rates (3.20) and (3.21), to the measured decay rates

$$\mathcal{P}(\Delta t, q) = \frac{e^{-|\Delta t|/\tau_{B^0}}}{4\tau_{B^0}} \left[ 1 + q \left( \mathcal{A}_{\eta'K_S^0} \cos \Delta M \Delta t + \mathcal{S}_{\eta'K_S^0} \sin \Delta M \Delta t \right) \right], \quad (4.5)$$

where  $q = +1$  when  $B_{tag} = B^0$  and  $q = -1$  when  $B_{tag} = \bar{B}^0$  mesons<sup>4</sup>. As we have seen, the measured decay rates differ from this PDF. To be still able to obtain the correct values of  $\mathcal{A}_{\eta'K_S^0}$  and  $\mathcal{S}_{\eta'K_S^0}$ , we have to include the experimental effects in  $\mathcal{P}(\Delta t, q)$ . The PDF that includes all three effects presented in the previous points is given by

$$\begin{aligned} \mathcal{P}(\Delta t, q) = & \\ & f_{sig} \frac{e^{-|\Delta t|/\tau_{B^0}}}{4\tau_{B^0}} \left[ 1 - q\Delta w + (1 - 2w)q \left( \mathcal{A}_{\eta'K_S^0} \cos \Delta M \Delta t + \mathcal{S}_{\eta'K_S^0} \sin \Delta M \Delta t \right) \right] \otimes \mathcal{R}_{sig}(\Delta t) \\ & + (1 - f_{sig}) \mathcal{P}_{bkg}(\Delta t) \otimes \mathcal{R}_{bkg}(\Delta t), \end{aligned} \quad (4.6)$$

where  $\mathcal{P}_{bkg}(\Delta t)$  is the PDF describing  $\Delta t$  distribution of background candidates, and  $\mathcal{R}_{sig}(\Delta t)$  and  $\mathcal{R}_{bkg}(\Delta t)$  are  $\Delta t$  resolution functions for signal and background candidates, respectively. In figure 4.2, the  $q = +1$  and  $q = -1$  components of the original (C.12) and modified PDF (4.6) are plotted, for some selected values of parameters  $\mathcal{A}_{\eta'K_S^0}$  and  $\mathcal{S}_{\eta'K_S^0}$ . For the modified PDF we used  $f_{sig} = 0.8$ ,  $w = 0.2$ ,  $\Delta w = 0$ , a Gaussian function with the width of 0.7 ps for the signal and background resolution function, and a delta function for the background  $\Delta t$  distribution. It nicely illustrates how the asymmetry between the distributions of  $B^0$  and  $\bar{B}^0$  gets less pronounced due to experimental limitations.

In order to obtain unbiased values of CPV parameters, it is of prime importance to have good understanding and estimations of  $f_{sig}$ ,  $w$ ,  $\Delta w$ ,  $\mathcal{P}_{bkg}$ ,  $\mathcal{R}_{sig}$  and  $\mathcal{R}_{bkg}$ . Furthermore, it is a well known fact that dividing data sample into subsamples, with different PDF parameters (based on some observable property), increases the fit sensitivity. In principle, the best sensitivity is achieved with the highest number of subsamples, which is obviously when each candidate is a subsample. This principle is utilized by unbinned maximum likelihood fit, a fit method that we use in the analysis. We determine the values of  $f_{sig}$ ,  $w$ ,  $\Delta w$ , and the shape of  $\mathcal{R}_{sig}$  and  $\mathcal{R}_{bkg}$ , for each candidate individually, based on the properties of the event. Then we construct a likelihood function and maximize it to obtain the best estimates for  $\mathcal{A}_{\eta'K_S^0}$  and  $\mathcal{S}_{\eta'K_S^0}$ .

In the next chapter we describe the experimental apparatus used to perform the measurement.

---

<sup>4</sup>Note that  $\mathcal{P}(\Delta t, q)$  is a two dimensional PDF with  $q$  being a discrete variable.  $\mathcal{P}(\Delta t, q)$  predicts the distribution of  $B^0$  mesons in  $\Delta t$  and  $q$ , and is normalized as a whole, over both variables.

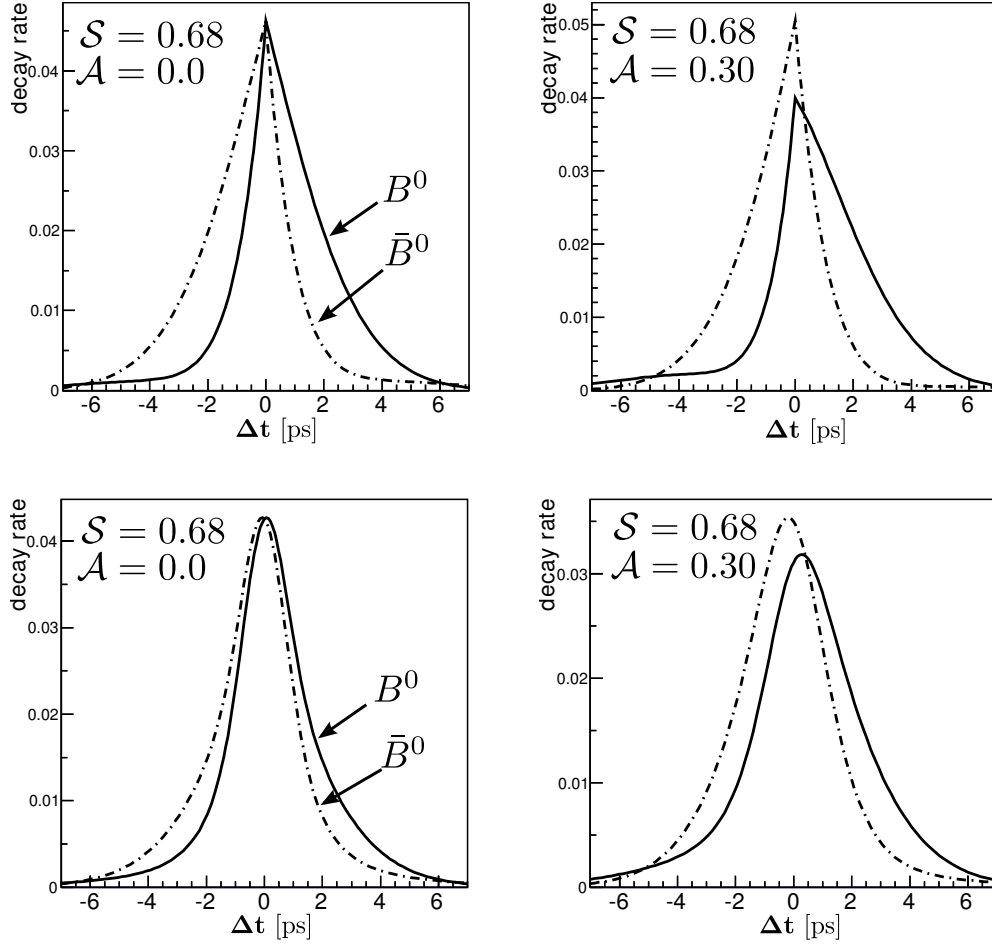


Figure 4.2: Time dependent decay rates of  $B^0$  and  $\bar{B}^0$  mesons in the case of  $\mathcal{S}_{\eta'K_S^0} = 0.68$  and  $\mathcal{A}_{\eta'K_S^0} = 0.0$  on the left, and in the case of  $\mathcal{S}_{\eta'K_S^0} = 0.68$  and  $\mathcal{A}_{\eta'K_S^0} = 0.3$  on the right. The top two plots show decay rates as theoretically predicted, and the bottom two plots show the decay rates modified by experimental limitations (presence of background ( $f_{sig} = 0.8$ ) and wrongly tagged candidates ( $w = 0.2$ ), finite detector resolution ( $\sigma_t = 0.7$  ps)).

# 5

## The Belle experiment

The Belle experiment is one of the world's two experiments operating on the so-called  $B$  factories. It is located in KEK, High Energy Accelerator Research Organization center in Tsukuba, Japan. It was designed in the 1990s, to exploit the properties of  $B$  mesons produced in  $e^+e^-$  collisions at the KEKB collider. The Belle collaboration consists of about 440 people from over 70 institutes, working on the experiment. In this chapter we describe in short the KEKB accelerator and the Belle detector, the experimental apparatus used to record  $B$  meson decays <sup>1</sup>.

### 5.1 The KEKB collider

The KEKB collider is an asymmetric energy  $e^+e^-$  collider [37], designed to produce a large number of  $B\bar{B}$  pairs. The energies of electron and positron beams are 8 GeV and 3.5 GeV, respectively. The electrons and positrons are first accelerated to their final energies in a linear accelerator (linac) and then injected into two separate storage rings of about 3 km in circumference, residing in a tunnel 11 m underground. There are about 1000 bunches of electrons and positrons in each ring, corresponding to the distance of about 3 m between them. The two rings intersect at a single point on the orbital trajectory, called the *interaction point* (IP), where the bunches collide and where the Belle detector is placed. The electron and positron beams collide at a finite angle of  $\pm 11$  mrad, to avoid parasitic collisions. On average

---

<sup>1</sup>The other  $B$  factory experiment is BaBar at the PEP-II collider at Stanford Linear Accelerator Laboratory (SLAC).

on approximately every  $10^5$  bunch collisions an  $e^+e^-$  interaction occurs, resulting in an outflow of particles produced in the collision, which are then detected in the Belle detector (in jargon we call this simply an *event*). The figure 5.1 illustrates the KEKB configuration.

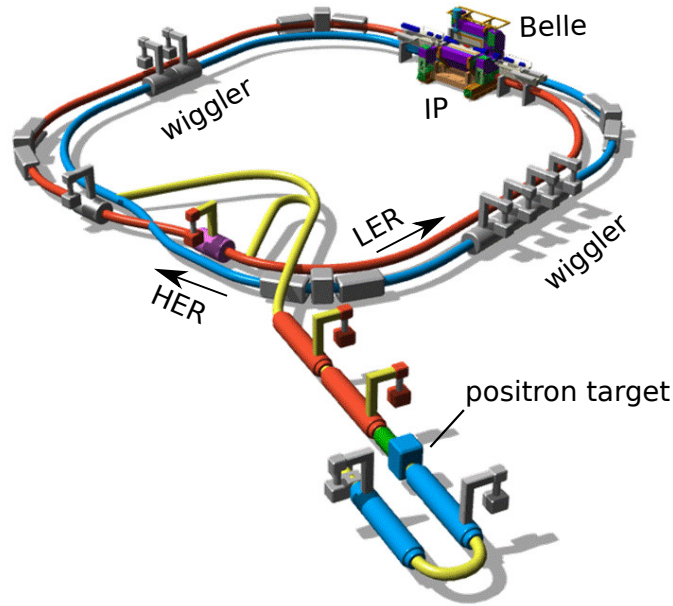


Figure 5.1: Configuration of the KEKB collider and the Belle detector.

The energy of the colliding beams is such, that the available energy in the CMS is equal to the mass of  $Y(4S)$  resonance, which is a bound state of a  $b$  and  $\bar{b}$  quark. However, in most events instead of the  $Y(4S)$  production, a lighter pair of quarks is produced in  $e^+e^- \rightarrow q\bar{q}$ , where  $q$  stands for  $u, d, s, c$ . In the studies of  $B$  mesons these events represent the background component. On the other hand, when the  $Y(4S)$  resonance is produced, it immediately decays into a  $B\bar{B}$  pair. As already argued in the previous chapter, this pair is approximately at rest in the CMS, since  $2M_B = 10.56$  GeV and  $M_{Y(4S)} = 10.58$  GeV. In combination with asymmetric beam energies this simplifies the kinematics of a  $B\bar{B}$  pair to a single dimension, makes the  $B$  meson flight distance measurable ( $\sim 200$   $\mu\text{m}$ ), and therefore allows for time dependent studies.

Beside asymmetric beam energies, a high luminosity is another property defining a  $B$  factory. To perform precision measurements it is crucial to collect a large sample of  $B$  decays. The design luminosity of the KEKB collider was  $\mathcal{L} = 1.0 \times 10^{34} \text{ cm}^{-2}\text{s}^{-1}$ . By the end of its operation in 2010 the peak luminosity reached the record value of  $\mathcal{L} = 2.1 \times 10^{34} \text{ cm}^{-2}\text{s}^{-1}$ , well exceeding the design value. The evolution of the KEKB luminosity, as well as its time integrated value, are shown in figure 5.2. From the

time integrated luminosity we can obtain the number of produced  $B$  meson pairs as

$$N_{B\bar{B}} = \sigma_{B\bar{B}} \int \mathcal{L} dt, \quad (5.1)$$

with  $\sigma_{B\bar{B}} \simeq 1$  nb being the cross section for  $B\bar{B}$  pair production at the energy of  $Y(4S)$  resonance. The integrated luminosity of the KEKB reached  $702 \text{ fb}^{-1}$  (at the energy of  $Y(4S)$  resonance), resulting in about 772 millions of  $B\bar{B}$  decays recorded by the Belle detector. This is the world's largest sample of  $B$  mesons.

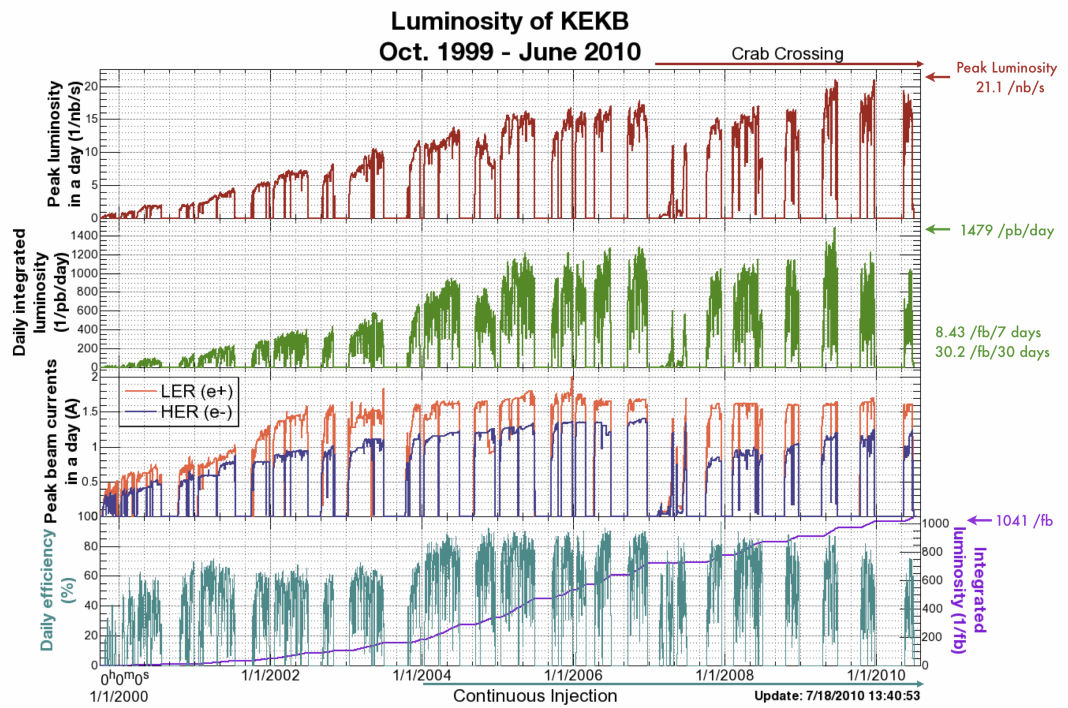


Figure 5.2: Time evolution of the KEKB luminosity. In the very bottom plot the purple line shows time integrated luminosity.

## 5.2 The Belle detector

The Belle detector is a large-solid-angle magnetic spectrometer that is able to detect long-lived particles produced in  $e^+e^-$  collisions. These are

Charged particles:  $e^\pm, \mu^\pm, \pi^\pm, K^\pm, p^\pm$

Neutral particles:  $\gamma, K_L^0$ .

These particles are commonly produced in decays of heavier particles, such as  $B$  or  $D$  mesons, or other short-lived hadrons, that decay practically at the interaction point and cannot be directly detected. From these long-lived remnants the decay has to be reconstructed, to explore the underlying physical processes. The basic demand for the detector is therefore to detect, measure the momentum, and determine the identity of mentioned particles with high efficiency. In addition to this, a good precision at determining the position of the decay vertex is crucial for time dependent studies. The Belle detector consists of several sub-detectors placed in cylindrically symmetric configuration around the IP, with some forward-backward asymmetries, following the asymmetry of  $e^+e^-$  collisions. The configuration of sub-detectors is illustrated in figure 5.3. We now briefly summarize how the information from each of them is utilized to fulfill the above demands, while more technical description is given in the following subsections.

In its essence the Belle detector is a magnetic spectrometer, allowing to measure charged particle momentum from the radius of curvature of its helix in a magnetic field. Large part of the Belle detector is inside the large superconducting solenoid, producing a homogeneous magnetic field of 1.5 T. Particle's helix is tracked in the central drift chamber through the ionisation of gas that it is filled with. In addition to momentum, the particle's charge is determined from the orientation of its helix. The information about identity of low momentum particles ( $< 1$  GeV) can also be obtained from the central drift chamber, by measuring their energy loss due to ionisation. Sub-detectors on the outer side of the drift chamber are used to provide an additional information on particle identity. Two main principles are used. Measuring the velocity of the particle, and the nature of its interaction with the material. By measuring the velocity and knowing the momentum one can determine particle's mass, as they are related with  $p = \gamma mv$ , and therefore its identity. The velocity is measured by aerogel Cherenkov counters, providing a good separation between high momentum ( $\sim 1.2 - 3.5$  GeV) pions and kaons, and by time of flight detector for separation at lower momenta. The nature of the interaction with the material is used in two calorimeters, the electromagnetic calorimeter to detect photons and identify electrons, and the KLM detector that is used to detect neutral kaons  $K_L^0$  and identify muons.

As it was argued in the previous chapter, for studies of time dependent asymmetries the decay vertex of  $B$  meson needs to be determined with the resolution of

about  $200 \mu\text{m}$ , or less. This would be impossible without a dedicated silicon vertex detector that is placed at the inner most region, closest to the IP. In the following sub-sections we describe each sub-detector.

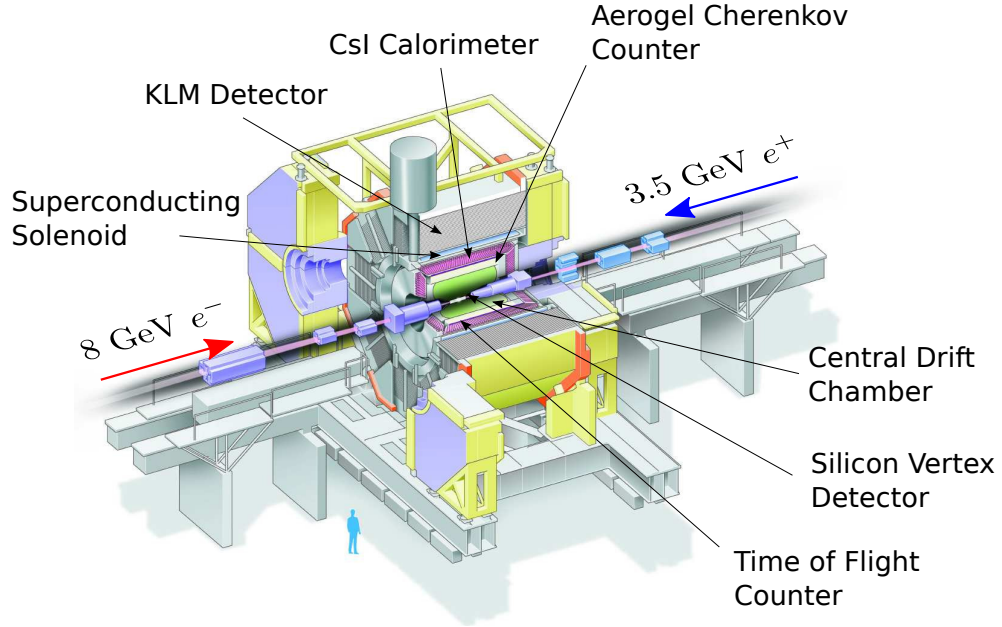


Figure 5.3: Illustration of the Belle detector with main sub-detector systems.

### Coordinate system

The coordinate system used throughout this work is the following. The origin is placed at the interaction point,  $z$  axis is pointed in the opposite direction of the positron beam,  $y$  axis points vertically upward, and  $x$  axis shows in the direction of  $\hat{x} = \hat{y} \times \hat{z}$ . Due to the finite angle between the electron and positron beam, the  $z$  axis and the electron beam direction are at an angle of  $22 \text{ mrad}$ . Most commonly we use the cylindrical coordinates  $(r, \phi, z)$ , where  $r = \sqrt{x^2 + y^2}$  and  $\phi$  is the polar angle around the  $z$  axis. In some cases we also use a spherical coordinate system with  $(r, \theta, \phi)$  coordinates, where  $\theta$  measures the inclination angle from the  $z$  axis. These definitions are illustrated in figure 5.4.

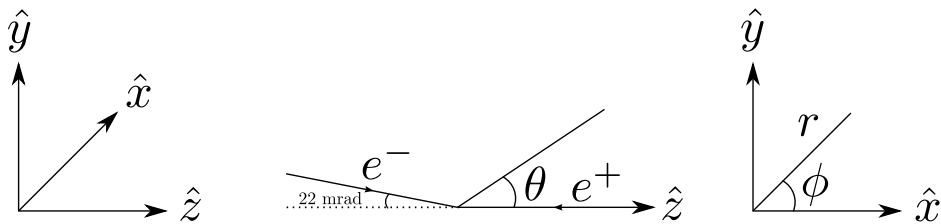


Figure 5.4: Definition of the coordinate system used throughout this work.

### 5.2.1 Silicon Vertex Detector

The Silicon Vertex Detector (SVD) plays a central role in measurements of time dependent CP violation, as it provides a precise measurements of  $B$  meson decay vertex position. Besides a good spatial resolution, it is also important for this sub-detector that the amount of material placed inside the detector acceptance is kept sufficiently low (to reduce the multiple scattering of particles). The most natural choice that meets this criteria is the use of double-sided silicon strip detectors (DSSDs).

The DSSD is basically a  $p$ - $n$  junction. A bias voltage is supplied to the  $n$ -side, while the  $p$ -side is grounded. When a charged particle passes through  $n$ -bulk silicon, it creates electron-hole pairs. These are then separated due to external field and collected at the strip electrodes on the opposite sides of DSSD, as illustrated in figure 5.5. Since the strips on one side are perpendicular to the strips on the other, collecting the charge from both layers makes it possible to determine the position of the particle crossing the DSSD plane.

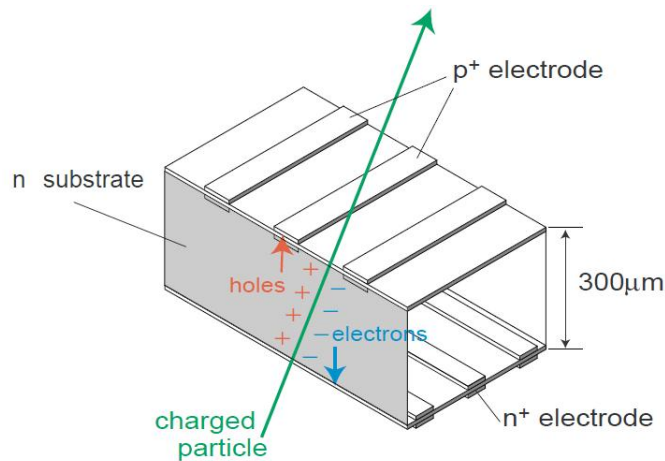


Figure 5.5: Principle of charged particle position determination with DSSDs.

In the SVD as initially implemented at Belle, the DSSD units were arranged in three cylindrical layers around the beampipe, as shown in figure 5.6. The modules in each layer are of different lengths, to cover the polar angle  $23^\circ < \theta < 139^\circ$ , corresponding to 86% of the full solid angle. Each DSSD module consists of 1280 sensitive strips. On the side that is oriented perpendicularly to the beam direction (to measure  $z$  position of vertex) they are separated by  $42 \mu\text{m}$ , while on the other side, with strips in the beam direction (to measure  $r - \phi$  position), the separation is  $25 \mu\text{m}$ . On the  $z$  side of the strips only every second channel is read (to reduce the number of readout channels) making the effective separation of strips  $84 \mu\text{m}$ .

After the accumulation of  $152 \times 10^6 B\bar{B}$  pairs the SVD was replaced with the re-designed and improved four layer SVD. The first one became commonly referred to as SVD1 and the second as SVD2, this notation is also used throughout this

work. Part of the reason for replacing it were the radiation damaged detectors and beampipe, but also the performance and the radiation tolerance improvements were aimed and achieved. Among several improvements were that the innermost layer was placed 1 cm closer to the IP, to the radius of 2 cm, and that the angular acceptance increased to  $17^\circ < \theta < 150^\circ$ . The position of the first SVD layer is indeed very important, because the resolution of the vertex position improves roughly as the inverse of its distance from the IP. In addition, the use of a smaller beampipe resulted in smaller degradation of the vertex resolution due to scattering.

The performance of the SVD can be characterized by its resolution on charged tracks hits, which is measured to be [5]

$$\sigma_{xy} = 21.9 \oplus \frac{32.5}{p\beta \sin^{3/2} \theta} \mu\text{m}, \quad \sigma_z = 27.8 \oplus \frac{31.9}{p\beta \sin^{5/2} \theta} \mu\text{m}, \quad (5.2)$$

where  $p$  is the particle's momentum in GeV and  $\theta$  its polar angle.

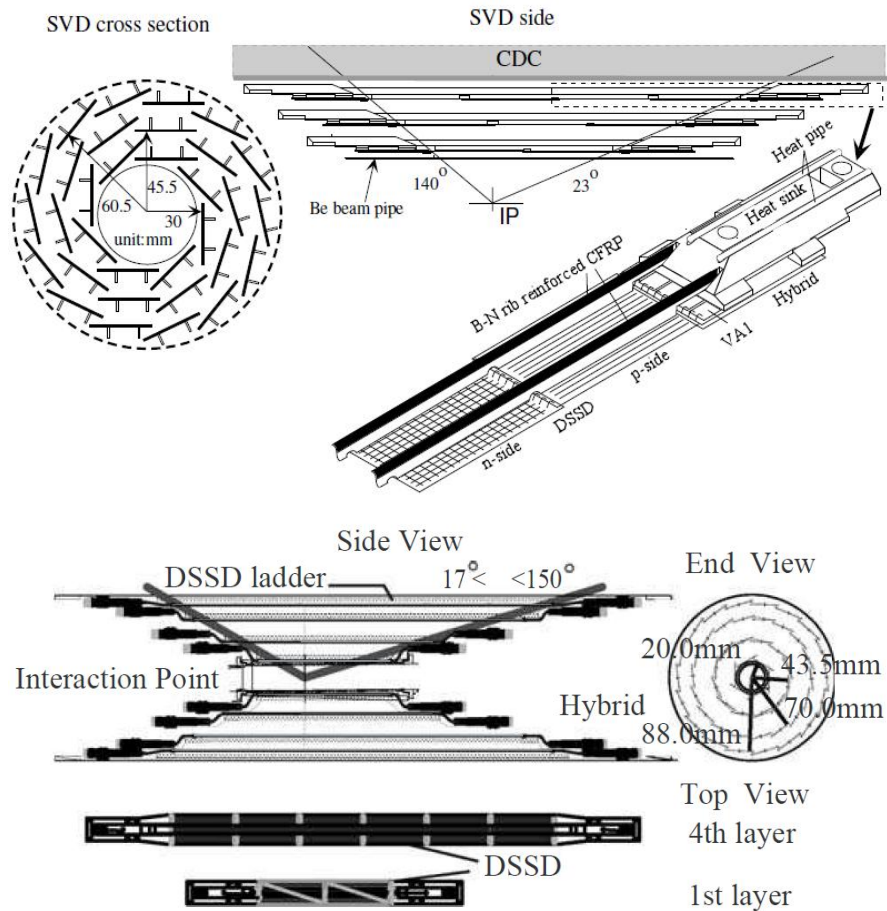


Figure 5.6: Two different SVD configurations. The top three images show configuration of the SVD as initially implemented (SVD1) and the bottom three images show configuration of the upgraded SVD (SVD2) [5].

### 5.2.2 Central Drift Chamber

The Central Drift Chamber (CDC) is used to determine the particle's momentum by measuring its track in the external magnetic field of 1.5 T, provided by the superconducting solenoid. The CDC consists of drift cells (8400 of them) that are made of eight negatively biased field wires, providing a drift field and surrounding a positively biased sense wire. The wires are aligned in the beam direction and join the aluminum endplates of the chamber that is filled with gas. The geometric configuration of the CDC is shown in figure 5.7. The longest wires are 2.4 m long, and the inner and outer radii of the CDC are 83 and 874 mm, respectively. The polar angle covered is  $17^\circ < \theta < 150^\circ$ . When a charged particle passes through the drift cell, it ionizes the gas and the electrons drift towards the nearest sense wire, with the specific velocity. Measuring the drift time gives the distance of the track from the sense wire. In the last millimeters from the wire the field increases as  $\propto 1/r$ , and electrons gain enough energy to cause secondary ionisation. This chain is then repeated, resulting in a cascade of charge, making a measurable signal. To obtain three dimensional information, the set of wires is at a small angle of  $\pm 50$  mrad to the  $z$  direction.

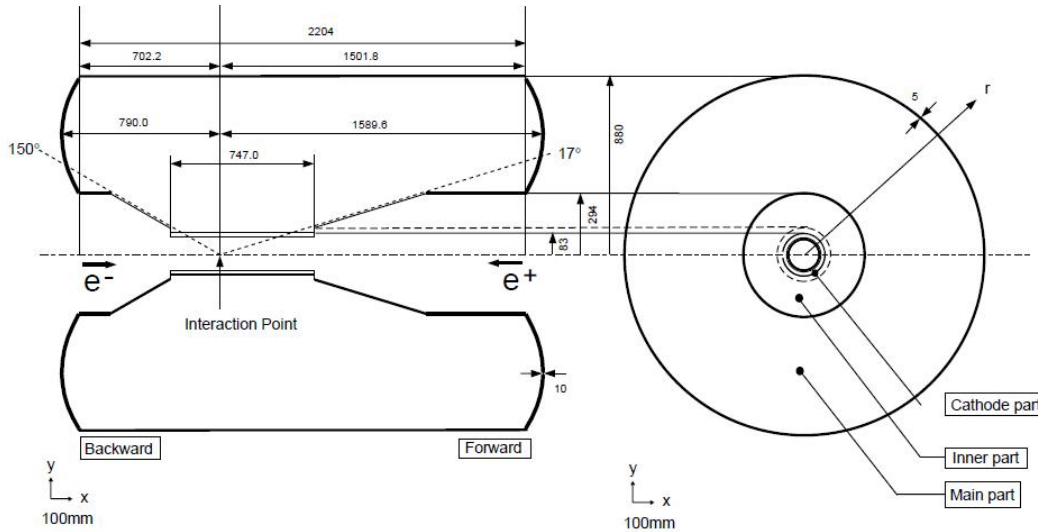


Figure 5.7: Geometric configuration of the CDC. The side and front view are shown [5].

Since the majority of particles produced in  $B$  decays have momenta lower than  $\sim 1$  GeV, the CDC is filled with a mixture of low- $Z$  gas (50% helium, 50% ethane), to reduce multiple Coulomb scattering contributions to momentum resolution. The relative resolution of the CDC on the transverse momentum  $p_T$  is given by [5]

$$\sigma(p_T) = \left( 0.19 p_T \oplus \frac{0.30}{\beta} \right) \%, \quad (5.3)$$

showing that the resolution varies from about 0.5% - 1% for particles with 1 - 5 GeV, respectively.

The size of the signal in the CDC is used to provide information on the identity of the particle, as it is related to the energy deposit of the particle per unit length ( $dE/dx$ ). Particle's energy loss due to ionisation of gas is related to its momentum in a way that depends on the particle's mass (the Bethe-Bloch formula). This is shown in figure 5.8, where the separation between pions, kaons, protons and electrons at momentum below 1 GeV can be clearly seen.

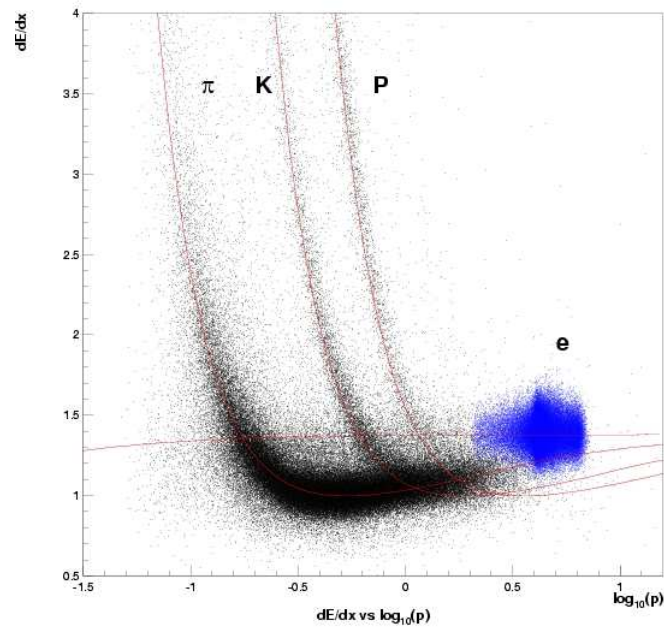


Figure 5.8: Energy loss of different particles in CDC as a function of particle's momentum [5].

### 5.2.3 Aerogel Cherenkov Counter

The Aerogel Cherenkov Counter (ACC) is used to provide separation between charged kaons and pions with high momenta (from 1.2 GeV to 3.5 GeV). A good separation between pions and kaons is crucial for efficient flavor tagging.

When a charged particle travels through a medium with a velocity that exceeds the speed of light in that medium, it emits Cherenkov photons. In a medium with the refractive index  $n$  a particle of mass  $m$  and given momentum  $p$  emits Cherenkov photons only if

$$m < p\sqrt{n^2 - 1} \quad (5.4)$$

is satisfied. By selecting appropriate  $n$  one can ensure that pions of given momentum are below that threshold, while kaons are not. On this basis they are separated in the ACC.

The ACC consists of counter modules, each being built from five silica aerogel tiles (used as a radiator) stacked in a thin aluminum box (0.2 mm thick), and one or two fine-mesh photomultiplier tubes (FM-PMTs) that can operate in a high magnetic field. The modules are configured as shown in figure 5.9. In the barrel part of the ACC, 960 modules are segmented into 60 cells in the  $\phi$  direction, while the endcap part consists of 228 modules arranged in 5 concentric rings. Five aerogel tiles in each counter have different refractive indices, ranging from 1.01 to 1.03, in order to provide good pion/kaon separation in the full kinematic range.

In figure 5.10, the number of detected photoelectrons for pions and kaons from  $D^{*\pm} \rightarrow D^0(K^-\pi^+)\pi^+$  decay is shown. A clear separation between the two is seen.

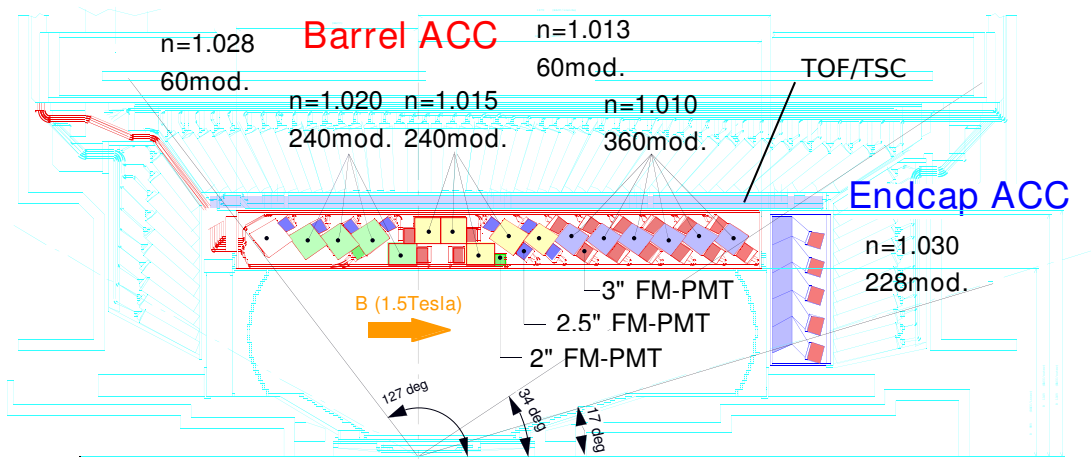


Figure 5.9: Geometric configuration of the ACC counter modules [5].

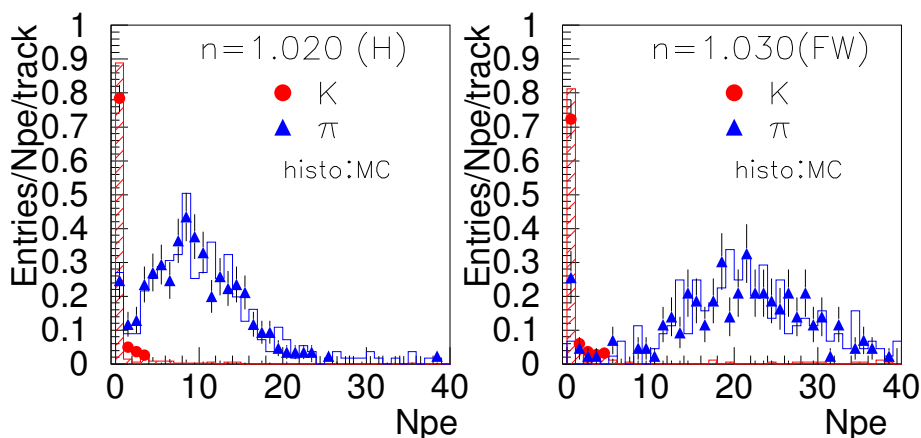


Figure 5.10: Number of detected photoelectrons in the ACC for pions and kaons from  $D^{*\pm}$  decays.

## 5.2.4 Time of Flight Counter

The Time of Flight Counter (TOF) gives particle identification information in order to separate charged pions and kaons with low momenta, below 1.2 GeV.

By measuring the time  $T$  that particle needs from the IP to the TOF ( $\sim 1.2$  m), and knowing its momentum  $p$ , particle's mass can be inferred by

$$m = p \sqrt{\frac{c^2 T^2}{L^2} - 1}. \quad (5.5)$$

Basic building blocks of the TOF are photomultiplier tubes with attached plastic scintillation counters. They provide a timing resolution of 100 ps, allowing the separation between kaons and pions at 1.0 GeV with  $3\sigma$  significance. The TOF also provides fast timing signals for the data acquisition trigger system. For this purpose, a thin trigger scintillation counter (TSC) is placed directly in front of two basic units to form a TOF module. The geometric configuration of a TOF module is shown in figure 5.11. In total there are 64 TOF modules placed in the barrel region at the radius of 1.2 m from the IP. The polar angle covered is  $34^\circ < \theta < 120^\circ$ .

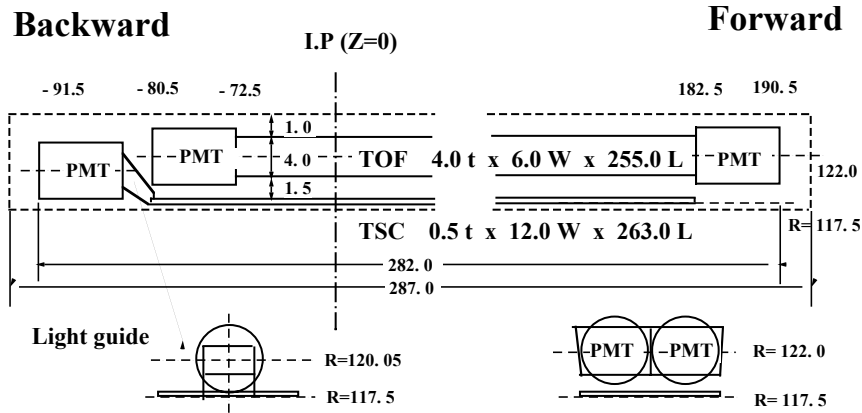


Figure 5.11: Geometric configuration of a TOF module [5]. All dimensions are in cm.

Figure 5.12 shows the mass distribution of particles with momentum below 1.2 GeV, as obtained from the TOF measurements. Separated peaks at masses of kaon, pion, and proton can be seen. Also the expected distribution obtained from the detector simulation is shown, and matches the measured data well.

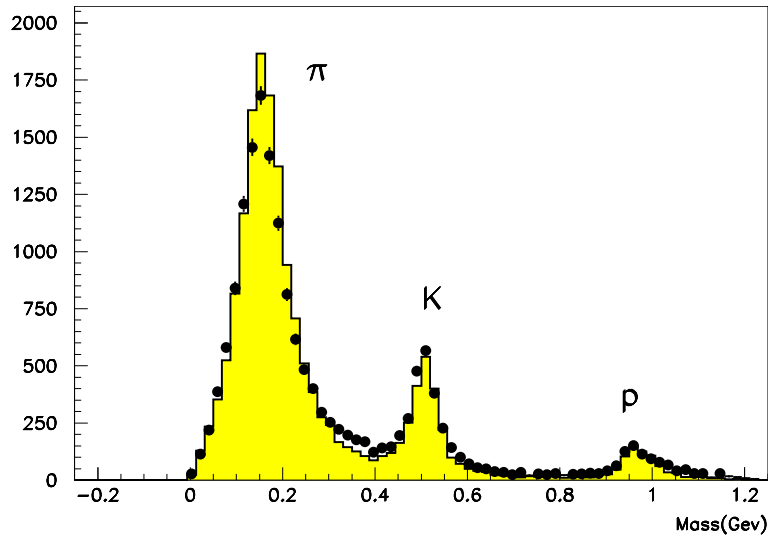


Figure 5.12: Particle mass distribution as obtained from time of flight measurements. The yellow histogram shows the distribution expected from detector simulation studies [5].

### 5.2.5 Electromagnetic Calorimeter

The Electromagnetic Calorimeter (ECL) is used to detect electrons and photons with high efficiency and with good energy and position resolution. In our analysis photons are used in the reconstruction of the  $\eta'$  meson, while electrons contribute to efficient flavor tagging.

A basic unit of ECL is a thallium doped CsI crystal block with two  $10 \times 20$  mm photodiodes attached. A crystal block has a tower shape and is 30 cm long, which corresponds to 16.2 radiation lengths. When an electron or a photon hits a crystal, its energy is deposited in electromagnetic showers, produced by bremsstrahlung and pair production. Fraction of the deposited energy in CsI converted to scintillation light detected by the attached photodiodes. On the contrary, hadrons and muons do not make electromagnetic showers and deposit only a small fraction of their energy through ionisation. Therefore, the ratio between deposited energy in crystal and particle momentum ( $E/p$ ) will be close to unity for electrons, and small for other particles. In this way electrons and photons can be identified, with photons having no associated track from the CDC.

In total the ECL consists of 8736 thallium doped CsI crystals. They are arranged in the configuration as shown in figure 5.13. The barrel part contains 6624 of them, where 144 are needed to fill the structure in the  $\phi$  direction, and 46 in the  $\theta$  direction. The forward (backward) endcap part contains 1152 (960) crystals, arranged into 13 (10) rings in  $\phi$ , each having 48-144 (64-144) crystals, depending on the  $\theta$  position. All crystals point toward the IP.

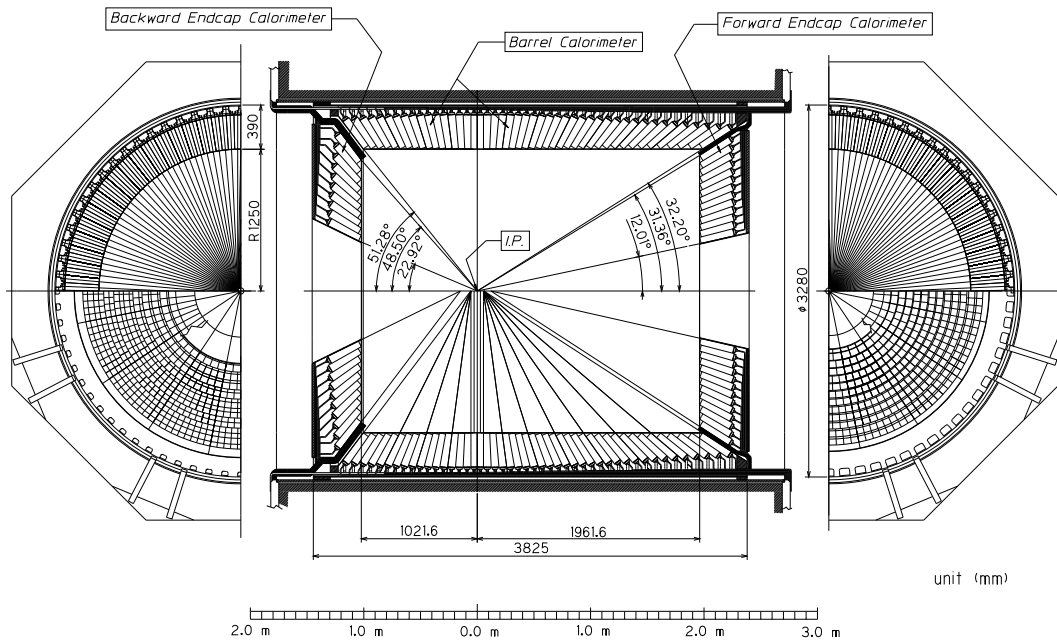


Figure 5.13: Geometric configuration of the ECL detector [5].

The energy resolution of the ECL [5] is given by  $\sigma_E/E = 1.34 \oplus 0.066/E \oplus 0.81/E^{1/4}$ , where  $E$  is in units of GeV. This resolution was measured in beam tests before the ECL was installed. The position resolution is given by  $\sigma_{pos} = 0.27 \oplus 3.4/E^{1/2} \oplus 1.8/E^{1/4}$ . Figure 5.14 shows photon energy and position resolution for different photon energies.

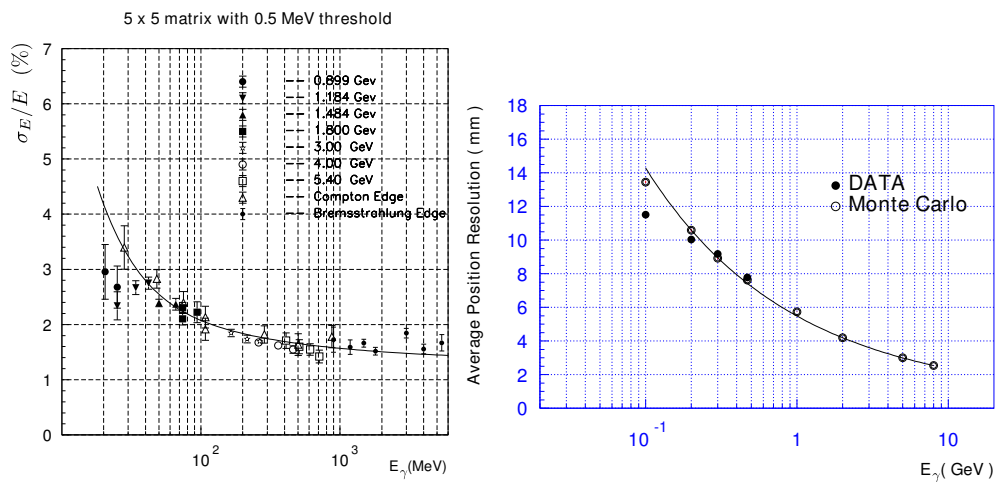


Figure 5.14: Energy and position resolution of the ECL detector as measured in beamtests [5].

### 5.2.6 Solenoid Magnet

The superconducting solenoid provides a magnetic field of 1.5 T in the cylindrical volume of 3.4 m in diameter and 4.4 m in length. The magnetic field bends charged particle tracks, allowing for momentum determination. The superconducting coil consists of a single layer niobium-titanium-copper alloy that is embedded in the high purity aluminum stabiliser. It is wound around the inner surface of the aluminum support cylinder, as shown in figure 5.15. Liquid helium, circulating through the colling tubes on the inner side of the support cylinder, is used for cooling.

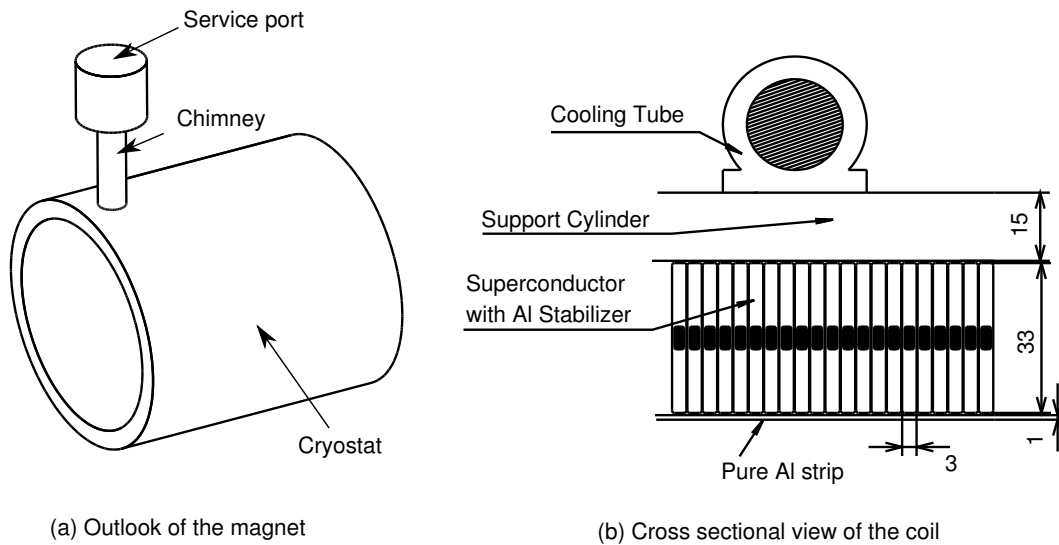


Figure 5.15: Geometric configuration of Belle superconducting solenoid magnet [5].

### 5.2.7 $K_L^0$ and muon detector

The  $K_L^0$  and muon detector (KLM) was designed to identify  $K_L^0$ 's and muons in a wide momentum range (at  $p_T > 0.6$  GeV, since only these can reach the KLM) and with high efficiency. For our analysis muon identification is important because it contributes to the efficiency of flavor tagging.

The KLM consists of alternating layers of charged particle detectors and 4.7 cm thick iron plates. When a  $K_L^0$  travels through the detector, it interacts with the iron and produces a shower of ionizing particles, that are detected in the detector layers. This allows us to obtain the direction of the  $K_L^0$ , while the measurement of its energy is not useful, due to large fluctuations of shower size.  $K_L^0$  can be separated from charged hadrons ( $\pi^\pm, K^\pm$ ) because it does not have an associated track in the CDC. Muons on the other hand, having a CDC track, can be discriminated from hadrons based on the different nature of the interaction with iron. Since muons interact only electromagnetically, they penetrate much further into the detector and with smaller deflections than hadrons, which are already stopped in the first few iron layers.

Overall the KLM consists of 15 detector and 14 iron layers in the octagonal barrel region and 14 detector and iron layers in each endcap (forward and backward). This corresponds to 3.9 interaction lengths for particles traveling in the normal direction to detector planes. Each of the detector layers is built from two glass resistive plate counters (RPCs). The RPCs have two parallel plate electrodes with high resistivity, separated by a gas-filled gap. An ionizing particle that passes the gap initiates a streamer discharge, resulting in a local discharge of the plates. The position of the discharge is read out by pickup strips attached to the plate. To obtain two dimensional position information two RPCs are used, one with the strips in the  $\theta$ , and other in the  $\phi$  direction.

In figure 5.16, the muon detection efficiency and fake rate (mainly from pions and kaons misidentified as muons) as a function of momentum are plotted.

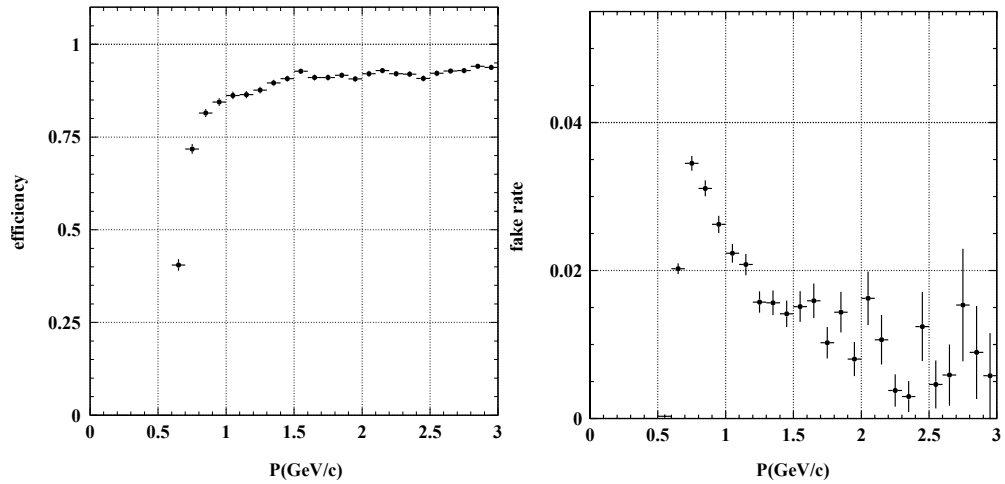


Figure 5.16: Muon detection efficiency and fake rate as a function of momentum in the KLM [5].

### 5.2.8 Trigger and Data acquisition

The purpose of the trigger system is to distinguish the events of interest ( $B\bar{B}$  production, for example) from a large amount of beam-induced backgrounds, as well as some physics processes in  $e^+e^-$  interactions (e.g. Bhabha events) having cross sections much larger than the processes of main interest. The cross sections for several physical processes and their expected contribution to the trigger rate at the KEKB design luminosity of  $10^{34} \text{ cm}^{-2}\text{s}^{-1}$  are given in table 5.1. The cross section for events of interest is small, but by imposing appropriate restrictive conditions the rate of background events can be significantly reduced. Due to high luminosity a high beam background<sup>2</sup> is expected, dominated by spent electrons and positrons. Since its rate is very sensitive to accelerator conditions, it is necessary for the trigger system to be robust against unexpected high background rates. The trigger rate is limited by the rate of data acquisition system. To maintain high trigger efficiency for the events of interest at high backgrounds, redundant triggers are necessary.

Physics proces	Cross section (nb)	Rate (Hz)
$\Upsilon(4S) \rightarrow B\bar{B}$	1.2	12
Hadron production from continuum	2.8	28
$\mu^+\mu^- + \tau^+\tau^-$	1.6	16
Bhabha ( $\theta_{lab} > 17^\circ$ )	44	4.4 <sup>a</sup>
$\gamma\gamma$ ( $\theta_{lab} > 17^\circ$ )	2.4	0.24 <sup>a</sup>
$2\gamma$ processes ( $\theta_{lab} > 17^\circ, p_t > 0.1\text{GeV}$ )	$\sim 15$	$\sim 35^b$
Total	$\sim 67$	$\sim 96$

<sup>a</sup> Indicates values prescaled by factor 1/100

<sup>b</sup> Indicates the restricted condition of  $p_t > 0.3 \text{ GeV}$

Table 5.1: Cross sections and trigger rates of physical processes in  $e^+e^-$  collisions at the KEKB energies and luminosity [5]. Backgrounds from Bhabha scattering and  $\gamma\gamma$  events are large, but they can be significantly reduced due to their distinct signatures. A small fraction is kept and used for luminosity monitoring and detector calibrations.

The Belle trigger system consists of a Level-1 hardware trigger and a Level-3 software trigger, that are operating in real-time during data taking. The Level-4 trigger, event reconstruction, and event classification, are done off-line. This flow is schematically shown in figure 5.17. In addition, the shematic view of Level-1 trigger is shown in figure 5.18. The central trigger, called the global decision logic (GDL), combines the trigger information from several sub-detector triggers and makes the final decision about triggering the data acquisition (DAQ). Triggering is mainly based on the information about the presence of charged tracks, provided by the CDC and TOF, and the total energy deposit in the ECL. The typical trigger rate is 200-250 Hz and

<sup>2</sup>Background coming from scattering of electrons and positrons in the beam.

the efficiency for triggering  $B\bar{B}$  events is greater than 99.5%.

When GDL triggers the DAQ, the event builder combines the signal from sub-detectors into a single event and passes it to the online computer farm. There, a basic track and cluster reconstruction is done. The Level-3 trigger then imposes additional restrictions and if not rejected, the event is sent to the computer center for offline processing.

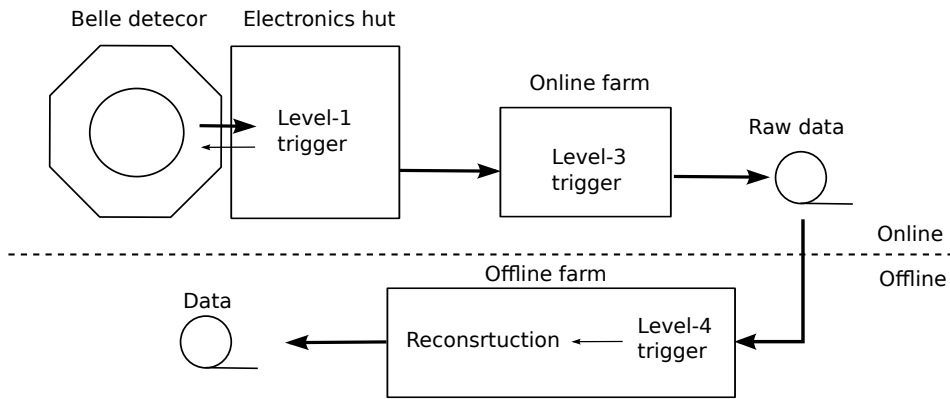


Figure 5.17: Diagram of Belle triggering system.

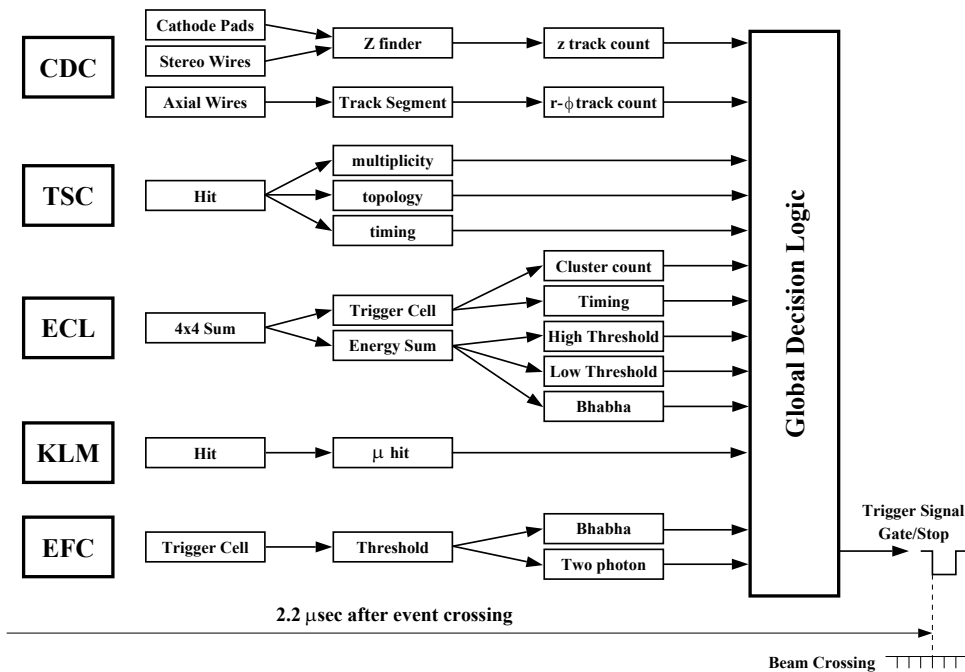


Figure 5.18: Belle Level-1 triggering scheme [5].

## 5.3 Offline computing

In the offline processing first the Level-4 triggering is performed, and the events passing it undergo full event reconstruction. Tracks are reconstructed from the CDC hits and extrapolated to the IP to search for the associated SVD hits, as well as to the outer detectors, to obtain and append the information on particle identity. The latter is given in the form of a likelihood value for different particle hypotheses, where the likelihood is formed by combining the information of different sub-detectors [38]. Finally, the event is formed as a collection of all tracks and neutral showers in the event, and available for the user performing the analysis.

### 5.3.1 Monte Carlo simulation

Another important task of offline computing is to generate a Monte Carlo simulation (MC) data, which is used to study the expected detector response and to prepare the analysis procedure. The MC data production is divided into two main parts, event generation and detector simulation. Simulated events are generated by event generator, according to the distributions from known underlying physical processes. Two event generator software packages are used: QQ and EvtGen [39,40], originally developed by CLEO and BaBar experiments, but adapted for the use in the Belle analysis. The generated particles are then tracked through the detector in the Belle full detector simulation (GSIM), based on the GEANT platform [41]. GEANT is a toolkit for the simulation of particle interaction with matter, developed at CERN and commonly used in high energy physics experiments. In the simulation the full Belle detector is implemented, providing each subdetector's response to the passage of a particle. The obtained output of the simulation is stored in the same event format as the real output from the measurements.

### 5.3.2 Analysis software

The first stage of the analysis, which includes the event reconstruction, reconstruction of vertices and flavor tagging, is done with software routines fully developed by the Belle collaboration. The analysis code runs within the event processing framework, called BASF (Belle Analysis Framework), where the event-by-event data is read from the data base and processed. The output, containing all the information needed for further analysis, is written in the format of ROOT files [42]. All further analysis steps are done within the ROOT framework, with the use of RooFit package, that provides a toolkit for modeling the expected distributions and performing maximum likelihood fits.

# 6

## Preparation of measurement procedure

In this chapter we describe the analysis procedure in detail. To prepare and validate the procedure a large dataset of simulated events is used, beside the nominal dataset of the measured events. On both datasets we reconstruct  $B$  candidates from the  $B^0 \rightarrow \eta' K_S^0$  and  $B^+ \rightarrow \eta' K^+$  decays. The candidates from the latter are used as the control sample. During the preparation of the analysis procedure we blind the flavor information of  $B^0$  candidates reconstructed from the measured events. Only when the analysis procedure is fully prepared and validated by studying the simulated data and the control sample, we unblind the flavor information, and use the prepared procedure to extract the CPV parameters from the candidates reconstructed from the measured events. This so-called *blind analysis* technique is applied in order not to bias the results of the measurement which could arise, for example, by determination of the selection criteria and other details of the method using measured data, or by the subjective observer induced biases.

The basic idea of the measurement procedure was already presented in chapter 4. The values of the CPV parameters can be extracted from the  $\Delta t, q$  distribution of reconstructed  $B$  candidates by fitting the PDF

$$\begin{aligned} \mathcal{P}(\Delta t, q) = & \\ & f_{sig} \frac{e^{-\Delta t/\tau_{B^0}}}{4\pi} \left[ 1 - q\Delta w + (1 - 2w)q \left( \mathcal{A}_{\eta' K_S^0} \cos \Delta M \Delta t + \mathcal{S}_{\eta' K_S^0} \sin \Delta M \Delta t \right) \right] \otimes \mathcal{R}_{sig}(\Delta t) \\ & + (1 - f_{sig}) \mathcal{P}_{bkg}(\Delta t) \otimes \mathcal{R}_{bkg}(\Delta t), \end{aligned} \quad (6.1)$$

to the measured  $\Delta t, q$  distribution. To be able to perform this fit, and obtain unbiased

values of the CPV parameters, the following points have to be done first:

1.  $B^0$  meson candidates decaying into  $\eta'K_S^0$  final state have to be reconstructed from a set of events.
2. Selection criteria need to be applied to reduce the number of  $B^0$  candidates coming from background events (events not containing  $B^0 \rightarrow \eta'K_S^0$  decay).
3. The fraction of candidates from signal events ( $f_{sig}$ ), among all the candidates surviving selection criteria, needs to be estimated.
4. The flavor of each  $B^0$  candidate needs to be determined ( $q = +1$  or  $q = -1$ ).
5. The  $\Delta t$  has to be determined by measuring a spatial distance between the decay vertices of both  $B$  mesons in the event.
6. The  $\Delta t$  resolution function of the signal candidates ( $\mathcal{R}^{sig}(\Delta t)$ ) has to be determined.
7. The  $\Delta t$  distribution of the candidates from the background events has to be studied to obtain  $\mathcal{P}_{bkg}(\Delta t) \otimes \mathcal{R}_{bkg}(\Delta t)$ .
8. Finally, the CPV parameters can be extracted by fitting the PDF (6.1) to the  $\Delta t, q$  distribution of the reconstructed  $B^0$  candidates.

In this chapter each of the points given above is described in its own section, following the same order.

We now name and describe different datasets that are used to prepare the analysis procedure. The terminology given is used through this work.

## Datasets

**Signal MC:** dataset of simulated signal events. Signal events contain  $e^+e^- \rightarrow Y(4S) \rightarrow B^0\bar{B}^0$  process, with one  $B$  meson of a pair decaying into  $\eta'K_S^0$  and the other decaying generically, according to all known and measured branching fractions.

**Generic BB MC:** dataset of simulated events containing  $e^+e^- \rightarrow Y(4S) \rightarrow B^+B^-$  or  $B^0\bar{B}^0$  process, with both  $B$  mesons decaying generically, but excluding our signal decay. These events represent background for our analysis.

**Continuum MC:** dataset of simulated  $e^+e^- \rightarrow q\bar{q}$  ( $q = u, d, s, c$ ) events. No  $B$  mesons are produced in these events and they represent background for our analysis.

**Measured data:** our nominal dataset of measured events from the Belle detector. This is the Belle final dataset, accumulated during the years of its operation (1999-2010). It contains about 772 millions  $B\bar{B}$  events, half of them being  $B^+B^-$  and half  $B^0\bar{B}^0$  events.

---

**Full MC:** dataset of simulated events obtained by merging signal MC, generic BB MC, and continuum MC, with the fractions as expected in the measured data. It contains a signal and all expected backgrounds, so this set is equivalent to the measured data.

To express the number of events contained in a dataset, we usually compare it with the expected number of events of specified type in the measured data. A term *stream* is used for the latter. For example, if we state that some study was done on 2 streams of signal MC, this means that the number of signal events in the dataset used was twice the number of signal events expected in the measured data.

## 6.1 $B^0 \rightarrow \eta' K_S^0$ decay

Here we trace the  $B^0 \rightarrow \eta' K_S^0$  decay to the final state long-lived particles, that can be detected with the Belle detector. The neutral  $B$  meson decays into  $\eta'$  and  $K^0$  meson with the branching fraction of [24]

$$\mathcal{B}(B^0 \rightarrow \eta' K^0) = (6.6 \pm 0.4) \times 10^{-5}. \quad (6.2)$$

After the decay,  $K^0$  undergoes  $K^0 - \bar{K}^0$  mixing and in 50% of cases decays as  $K_S^0$  and in other 50% as  $K_L^0$ . In this analysis only the  $K_S^0$  is used<sup>1</sup>.  $K_S^0$  decays into  $\pi^0\pi^0$  in roughly 30%, and into  $\pi^+\pi^-$  in roughly 70% of the cases. A neutral pion decays into two photons, while charged pions are long-lived (compared to the time they need to cross the detector).

The  $\eta'$  meson has three relevant decay modes, with the branching fraction larger than 3%. Two of them contain the intermediate  $\eta$  meson, which further decays into states of three pions or two photons, and one contains the intermediate  $\rho^0$  meson, which decays into two charged pions. The branching fractions of all decays in this chain are summarized in table 6.1. In table 6.2 we give some basic properties of the particles involved.

## 6.2 Event reconstruction and selection

In this section we describe how the  $B^0 \rightarrow \eta' K_S^0$  decay is reconstructed, and the criteria used to reduce the number of  $B$  candidates coming from the background events.

To reconstruct the  $B^0 \rightarrow \eta' K_S^0$  decay we use two  $\eta'$  decay modes,  $\eta' \rightarrow \rho^0\gamma$  and  $\eta' \rightarrow \pi^+\pi^-\eta$ , and both  $K_S^0$  decay modes,  $K_S^0 \rightarrow \pi^+\pi^-$  and  $K_S^0 \rightarrow \pi^0\pi^0$ . To

---

<sup>1</sup>Reconstruction of  $K_L^0$  demands quite a different technique, as  $K_L^0$  leaves no traces in the CDC. The measurement of  $B \rightarrow \eta' K_L^0$  is a subject of another study.

particle	decay mode	$\mathcal{B}$ in %
$\eta'$	$\pi^+\pi^-\eta$	$43.4 \pm 0.7$
	$\rho^0\gamma$	$29.3 \pm 0.6$
	$\pi^0\pi^0\eta$	$21.6 \pm 0.8$
$\eta$	$\gamma\gamma$	$39.3 \pm 0.2$
	$\pi^0\pi^0\pi^0$	$32.6 \pm 0.2$
	$\pi^+\pi^-\pi^0$	$22.7 \pm 0.3$
$\rho^0$	$\pi^+\pi^-$	$\sim 100$

Table 6.1: Current world average values of branching fractions for the  $\eta'$ ,  $\eta$  and  $\rho^0$  decays [24]. In the table all the decay modes with  $\mathcal{B} > 5\%$  are given.

particle	quark content	mass [MeV]	$I(J^P)$	lifetime [s]
$B^0$	$d\bar{b}$	$5279.58 \pm 0.17$	$\frac{1}{2}(0^-)$	$(1.519 \pm 0.007) \times 10^{-12}$
$\eta'$	$\frac{1}{\sqrt{3}}(u\bar{u} + d\bar{d} + s\bar{s})$	$957.78 \pm 0.06$	$0(0^-)$	$(3.39 \pm 0.16) \times 10^{-21}$
$\rho^0$	$\frac{1}{\sqrt{2}}(u\bar{u} - d\bar{d})$	$775.49 \pm 0.34$	$1(1^-)$	$(4.41 \pm 0.02) \times 10^{-24}$
$\eta$	$\frac{1}{\sqrt{6}}(u\bar{u} + d\bar{d} - 2s\bar{s})$	$547.86 \pm 0.02$	$0(0^-)$	$(5.02 \pm 0.18) \times 10^{-19}$
$K_S^0$	$\frac{1}{\sqrt{2}}(d\bar{s} - s\bar{d})$	$497.61 \pm 0.02$	$\frac{1}{2}(0^-)$	$(8.954 \pm 0.004) \times 10^{-11}$
$\pi^+$	$u\bar{d}$	$139.5702 \pm 0.0004$	$1(0^-)$	$(2.603 \pm 0.001) \times 10^{-8}$
$\pi^0$	$\frac{1}{2}(u\bar{u} - d\bar{d})$	$134.9766 \pm 0.0006$	$1(0^-)$	$(8.52 \pm 0.18) \times 10^{-17}$
$\gamma$	-	0	$0(1^-)$	stable

Table 6.2: Basic properties of all particle species involved in the  $B^0 \rightarrow \eta' K_S^0$  decay chain, relevant for our analysis [24].

reconstruct the  $\eta$  meson we use  $\eta \rightarrow \gamma\gamma$  and  $\eta \rightarrow \pi^+\pi^-\pi^0$  decay, and for the  $\rho^0$  its decay into  $\pi^+\pi^-$  is used. Other decay modes are not used because of low reconstruction efficiency and high background rates, mainly due to many neutral pions involved. Modes used for the analysis together account for about 57% of all  $B^0 \rightarrow \eta' K_S^0$  decays. In the main part of this work we describe only the analysis with  $K^0 \rightarrow \pi^+\pi^-$ . The reconstruction of  $B$  candidates with  $K^0 \rightarrow \pi^0\pi^0$  brings a small contribution to the analysis (about 10% of signal  $B$  candidates, with significantly higher background fraction), and we describe it in appendix A. Three distinct decay chains are therefore described in this work, and throughout it we use the following notation

$$\begin{aligned}
 \rho^0 \text{ mode: } & \eta' \rightarrow \rho^0\gamma & \text{with } \rho^0 \rightarrow \pi^+\pi^- \\
 \eta \rightarrow \gamma\gamma \text{ mode: } & \eta' \rightarrow \pi^+\pi^-\eta & \text{with } \eta \rightarrow \gamma\gamma \\
 \eta \rightarrow 3\pi \text{ mode: } & \eta' \rightarrow \pi^+\pi^-\eta & \text{with } \eta \rightarrow \pi^+\pi^-\pi^0.
 \end{aligned}$$

Each of the decay modes is reconstructed by combining the event charged pion tracks and photon candidates, as these are the only final state particle species in our decay.

Blindly combining particles would be useless, since there is an abundance of events containing charged tracks and photon hits. However, by examining the properties of candidates reconstructed from the MC samples (where we can separate signal and background events), we can determine the selection criteria that best separate signal and background events. We impose the selection criteria that will be satisfied by a large fraction of signal candidates, and at the same time reject a significant amount of background candidates. Having a large amount of background candidates, even if correctly described in the PDF used for the fit, results in a lower sensitivity to the fitted parameters (larger statistical uncertainty). On the other hand, since there is no distribution in which the signal and background candidates are completely separated, by imposing the selection criteria we are also losing some fraction of signal candidates. Because the goal of this analysis is to obtain the values of CPV parameters with the smallest possible uncertainty, we optimize the selection criteria to achieve this goal. After the full analysis procedure is prepared, we optimize each of the criteria by examining the statistical uncertainty of the CPV parameters extracted from the fit. This procedure has to be applied iteratively, because changing one criteria changes the optimal value of all others. As an example, in figure 6.1 the energy distributions of photons arising from simulated  $\eta' \rightarrow \rho\gamma$  decay (signal) and photons from simulated background events are shown. In addition, we show the statistical uncertainty ( $\sigma_{stat}$ ) on  $S_{\eta'K_S^0}$ , obtained from the fit of the CPV parameters on the full MC sample, for different values of criteria on photon minimal energy<sup>2</sup>. We find our result to have the smallest  $\sigma_{stat}$  if we require the photons to have energy larger than 0.1 GeV. Using the presented approach, all selection criteria introduced in the next section were optimized.

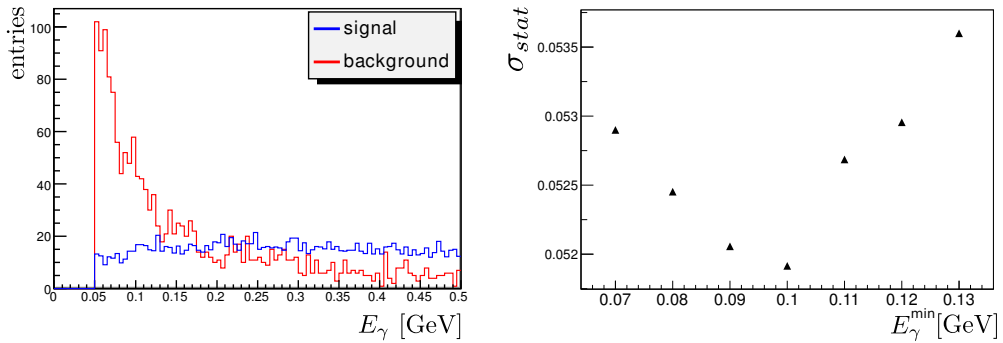


Figure 6.1: **Left:** Energy distribution of photons from simulated  $\eta' \rightarrow \rho^0\gamma$  decays (signal) and from MC background events (background), surviving all other selection criteria imposed (in the event pre-selection  $E_\gamma > 0.05$  GeV was required). **Right:** Statistical uncertainty of  $S_{\eta'K_S}$  for different values of photon minimal energy requirement.

<sup>2</sup>All other selection criteria used (introduced in the next sections) are here set to their optimized values.

The most efficient selection criteria in this analysis are based on the invariant masses of  $\eta'$ ,  $K_S^0$ ,  $\eta$ , and  $\rho^0$  mesons. We calculate the invariant mass of these intermediate mesons by

$$M^2 = \left| \sum_i E_i \right|^2 - \left| \sum_i \vec{p}_i \right|^2, \quad (6.3)$$

where the sums run over all decay products of the reconstructed meson,  $E_i = \sqrt{M_i^2 + |\vec{p}_i|^2}$  is the energy,  $M_i$  mass, and  $\vec{p}_i$  momentum of the  $i$ -th particle among the decay products. For example, when we combine two pion tracks to reconstruct the  $\rho^0$  meson, we expect the obtained invariant mass to be close to the  $\rho^0$  nominal mass ( $775.4 \pm 0.4$  MeV [24]) if the two pion tracks indeed arise from the  $\rho^0$  decay. On the other hand, if we combine two random pion tracks, we expect the obtained invariant mass to be random as well. For the signal candidates the distribution of the invariant mass of reconstructed  $\rho^0$  meson should form a peak around 775 MeV, smeared for the  $\rho^0$  natural width and the detector resolution, and for the background candidates this distribution should be approximately flat. Constraining the invariant mass of two pions to be in the selected mass window around the nominal  $\rho^0$  mass significantly reduces the number of reconstructed  $B$  candidates from the background events. In figure 6.2, the invariant mass of two pions from the simulated  $\rho^0$  decays, and from the MC events containing no  $\rho^0$  meson are shown. Similarly, we plot the invariant mass distribution of  $\eta'$ , reconstructed by combining the  $\rho^0$  meson and  $\gamma$ .

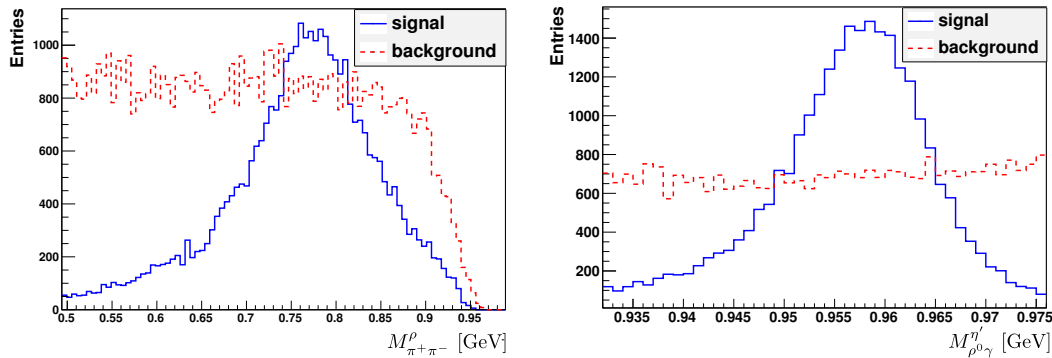


Figure 6.2: Simulated invariant mass distributions of the reconstructed  $\rho^0$  (left) and  $\eta'$  (right) mesons, for the case when the tracks used for the reconstruction are really coming from the  $\rho^0$  ( $\eta'$ ) decay (signal, blue line), and for the case when random tracks are combined (background, red line). The cutoff at the high end of  $\rho^0$  background distribution is due to already applied cut on the reconstructed  $\eta'$  invariant mass.

## 6.2.1 Charged track selection

Tracks of charged particles are obtained by track fitting algorithm, that fits a helix to the CDC and the SVD hits. To reconstruct our signal decay only pion tracks are needed, but as it was already pointed out, we are not able to unambiguously distinguish pions and kaons. Based on the information from the ECL, TOF, and ACC subdetectors, we form the likelihood functions  $\mathcal{L}_K$  and  $\mathcal{L}_\pi$  of particle being a kaon or a pion, respectively. Then we define a kaon/pion separation likelihood ratio as

$$\mathcal{L}_{K/\pi} = \frac{\mathcal{L}_K}{\mathcal{L}_K + \mathcal{L}_\pi}, \quad (6.4)$$

which is close to 1 for kaons and close to 0 for pions. In figure 6.3 the  $\mathcal{L}_{K/\pi}$  distribution of pion and kaon tracks from the MC sample is shown. For the tracks used in our analysis we demand  $\mathcal{L}_{K/\pi} < 0.9$ , to remove tracks that very likely belong to kaons. In addition, for the tracks used to reconstruct the  $\eta'$ ,  $\eta$  and  $\rho^0$  meson we demand to originate from the IP, as the flight length of these mesons is negligible due to short lifetimes. The track impact parameter, which is the smallest distance between the IP and the track in the  $r - \phi$  plane, has to be below 0.15 cm.

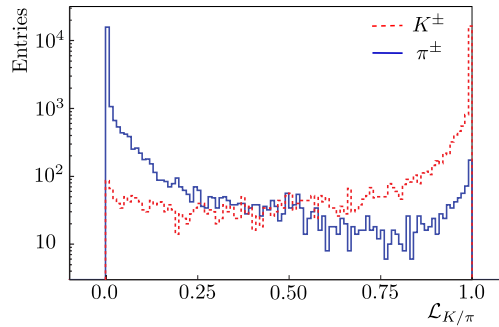


Figure 6.3: Distribution of  $\mathcal{L}_{K/\pi}$  for charged pion and kaon tracks, obtained from the MC sample. Note the logarithmic scale.

## 6.2.2 Kinematic fit

Before describing the decay reconstruction and selection, we briefly describe kinematic fits that are used at several points to reduce the effects of the detector resolution. Two kinds of kinematic fits are used, a mass-constrained and a vertex-constrained fit.

In the mass-constrained fit we fix the mass of the reconstructed particle to its nominal mass, and recalculate the momenta of the particles used for the reconstruction, to satisfy this requirement. Such a fit improves the finite resolution on the invariant mass, calculated from the reconstructed final state particles (the finite resolution is a consequence of finite accuracy in the final state particles momenta). This

allows us to put more stringent criteria on the masses of reconstructed mesons, and therefore improve the background reduction.

In the vertex-constrained fit all particles used in the reconstruction are constrained to originate from the same vertex. The fitting algorithm determines the most probable vertex position, and adjusts the momenta of the daughter particles to originate from this position. Such a fit improves the mass resolution, and is used to obtain the vertex position when needed.

The kinematic fit technique is based on a least squares method with Lagrangian multipliers and is described in detail in [43].

### 6.2.3 Reconstruction of $\eta'$ meson

To reconstruct the  $\eta'$  meson two main submodes are used,  $\eta' \rightarrow \rho^0\gamma$  and  $\eta' \rightarrow \pi^+\pi^-\eta$ . First we reconstruct the  $\rho^0$  or  $\eta$  meson, and then add the remaining particles to obtain the  $\eta'$ .

#### Reconstruction of $\rho^0$

The  $\rho^0$  is reconstructed by combining  $\pi^+$  and  $\pi^-$  tracks. We perform vertex-constrained fit with these two tracks, and require the pair invariant mass to satisfy  $0.5 \text{ GeV} < M_{\pi^+\pi^-}^{\rho^0} < 0.95 \text{ GeV}$ .

#### Reconstruction of $\eta$

The  $\eta$  is reconstructed either by combining two photons or three pions. Photons are obtained from clusters in the ECL that have no associated charged tracks in the CDC. Assuming that photons originate from the IP, we are able to obtain their momentum vector from the measured energy and the cluster position. For photons we require them to have an energy larger than  $E_\gamma > 0.05 \text{ GeV}$ , and for a photon pair to be accepted as the  $\eta$  candidate its invariant mass must satisfy  $0.5 \text{ GeV} < M_{\gamma\gamma}^\eta < 0.58 \text{ GeV}$ .

For the  $\eta \rightarrow \pi^+\pi^-\pi^0$  decay we first reconstruct the  $\pi^0$  by combining two photons, which again must have  $E_\gamma > 0.05 \text{ GeV}$ . For this pair we require the invariant mass of  $0.118 \text{ GeV} < M_{\gamma\gamma}^{\pi^0} < 0.15 \text{ GeV}$ , and the momentum of the reconstructed  $\pi^0$  in the CMS to be  $p_{\pi^0}^{cms} > 0.1 \text{ GeV}$ . After these criteria, the mass constrained fit on the  $\pi^0$  candidate is performed. Finally the  $\pi^0$  candidate is combined with  $\pi^+$  and  $\pi^-$ , and triples with the invariant mass between  $0.535 \text{ GeV} < M_{\pi^+\pi^-\pi^0}^\eta < 0.558 \text{ MeV}$  are selected as  $\eta$  candidates. The mass constrained fit is performed on the  $\eta$  candidate. It improves the mass resolution of the  $\eta'$ .

## Reconstruction of $\eta'$

The  $\eta'$  is reconstructed by combining the  $\rho^0$  with a photon, or by combining the  $\eta$  with two charged pions. For the  $\eta' \rightarrow \rho^0\gamma$  mode we require the photons to have energy  $E_\gamma > 0.1$  GeV, and the invariant mass of the  $\rho^0\gamma$  pair to be  $0.932 \text{ GeV} < M_{\rho^0\gamma}^{\eta'} < 0.975 \text{ GeV}$ . For the  $\eta' \rightarrow \pi^+\pi^-\eta$  mode constraint on the  $\eta'$  invariant mass is  $0.942 \text{ GeV} < M_{\pi^+\pi^-\eta(\gamma\gamma)}^{\eta'} < 0.970 \text{ GeV}$  in the case when  $\eta$  is reconstructed from two photons, and  $0.945 \text{ GeV} < M_{\pi^+\pi^-\eta(3\pi)}^{\eta'} < 0.970 \text{ GeV}$  when  $\eta$  is reconstructed from  $\pi^+\pi^-\pi^0$ . Different criteria are imposed because the width of the  $\eta'$  signal peak and the amount of background is different for these two modes. In figure 6.4, the invariant mass distributions of  $\eta'$ , reconstructed from the simulated signal events and from the measured data are shown, for all three decay modes.

After the  $\eta'$  reconstruction and selection, we perform the mass constrained fit, as it improves the energy resolution of the reconstructed  $B$  meson.

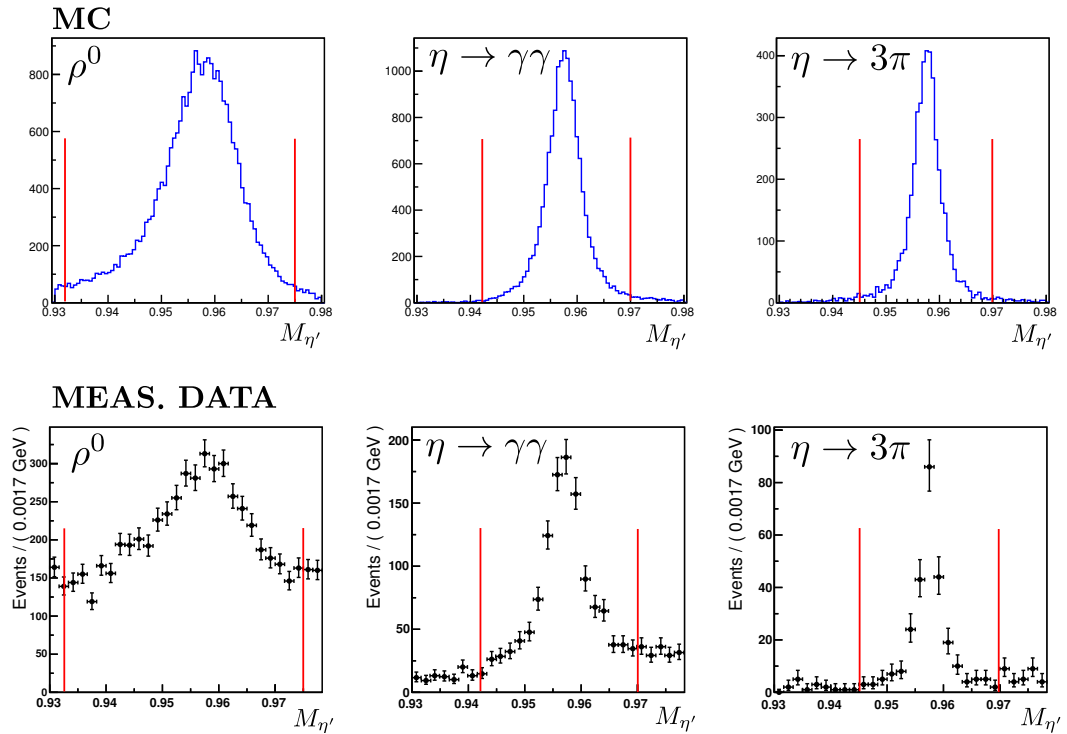


Figure 6.4: Invariant mass distribution of  $\eta'$  reconstructed from the signal MC (top), and from the measured data (bottom), for all three reconstructed modes. For the distribution from the measured data additional selection criteria on the reconstructed  $B$  meson kinematic variables were imposed, as explained in section 6.2.5. The red lines show imposed selection criteria on the  $\eta'$  invariant mass.

### 6.2.4 Reconstruction of $K_S^0$

To reconstruct the  $K_S^0$  two charged pion tracks are combined. The momentum of the reconstructed  $K_S^0$  is required to be greater than 0.06 GeV, and its invariant mass to differ less than 20 MeV from the  $K_S^0$  nominal mass. The number of background candidates can be further reduced by the fact that  $K_S^0$  travels a finite distance of about 3 cm ( $= c\tau_{K_S^0}$ ) before decaying. Because there are many correlated observables related to this fact, we use the NeuroBayes neural network package [44] to optimize the separation between the signal and background candidates. The NeuroBayes package is a tool for multivariate analysis of correlated data, based on Bayesian statistics. A neural network is first trained to differentiate between signal and background candidates on a large MC sample, utilizing the differences of signal and background distributions in several input variables, given in table 6.3. An example of such distribution is shown in figure 6.5. Once trained, the neural network transforms the values of input variables of each reconstructed candidate into a single output value, used to classify the candidate. The distribution of output value for signal and background  $K_S^0$  candidates is shown in figure 6.6. By imposing a criteria on the neural network output value, we are able to achieve above 90% efficiency of the  $K_S^0$  reconstruction<sup>3</sup>, at purity level of 93% (having only 7% of fake candidates). In figure 6.7 the invariant mass distributions of selected  $K_S^0$  candidates from the MC and from the measured data are shown.

Input variable
- $K_S^0$ momentum
- Distance between $\pi^+$ and $\pi^-$ helices in the z direction
- Distance between $K_S^0$ decay vertex and IP in the $x - y$ plane
- Angle between the $K_S^0$ momentum and direction
- Shorter and longer distance between the IP and the pion helices
- Angle between the $K_S^0$ momentum (in lab. system) and the pion momentum in the $K_S^0$ CMS
- $\pi^+$ and $\pi^-$ have SVD hits or not
- Number of $\pi^+$ and $\pi^-$ hits in the CDC

Table 6.3: Variables used by the neural network to optimize the separation between the signal and background  $K_S^0$  candidates.

<sup>3</sup>95% of initially reconstructed  $K_S^0$  candidates are retained.

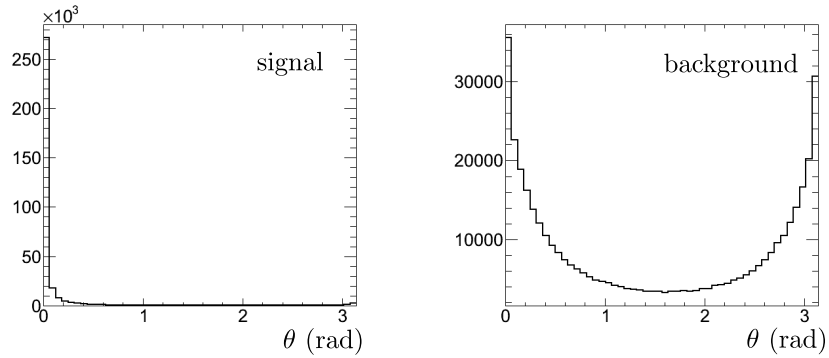


Figure 6.5: Distribution of the angle between  $K_S^0$  candidate flight direction and momentum, for the signal and background  $K_S^0$  candidates from the MC sample. Assuming that  $K_S^0$  originates from the IP, its flight direction is given by its decay vertex position, which is obtained from the vertex fit of charged pion tracks used for the reconstruction. For true  $K_S^0$  candidates direction and momentum vectors are aligned, while this only holds for a small fraction of background candidates.

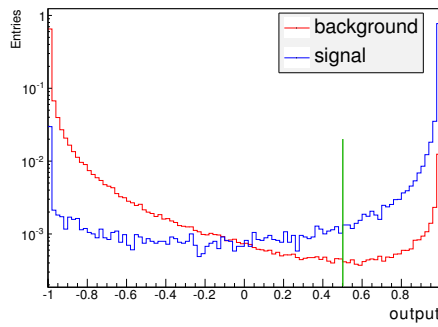


Figure 6.6: Normalized distributions of neural network output value for signal (blue) and background (red)  $K_S^0$  candidates, from the MC sample. The green line shows the criteria imposed to select signal candidates (output > 0.5). Note the logarithmic scale.

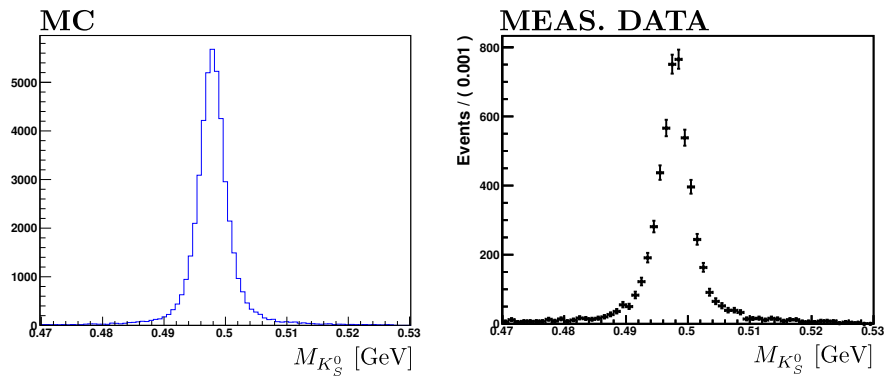


Figure 6.7: Invariant mass distribution of selected  $K_S^0$  candidates reconstructed from the MC and from the measured data.

### 6.2.5 Reconstruction of $B^0$ meson

Finally the  $B^0$  candidates are reconstructed by combining  $\eta'$  and  $K_S^0$  candidates. Sometimes we reconstruct more than one  $B$  candidate in a single event. This happens in about 10% of events that contain at least one  $B$  candidate, mainly because of the multiplicity of photons used in the  $\eta'$  reconstruction. In such a case, we select the candidate with the lowest  $\chi^2$  from the  $\eta'$  mass constrained fit, and reject the others. We find from the signal MC study that in 75% of cases, the selected candidate is the correct one.

Among the reconstructed  $B$  candidates there is still a significant fraction of background events. From the study of the MC sample it can be seen that these are mainly arising from continuum events, i.e. events with  $e^+e^- \rightarrow u\bar{u}, d\bar{d}, s\bar{s}, c\bar{c}$  processes. For the candidates reconstructed with the  $\rho^0$  decay mode, a few percent of the background candidates are coming from the generic  $B\bar{B}$  decays, while for the  $\eta \rightarrow \gamma\gamma$  and  $\eta \rightarrow 3\pi$  modes their contribution is negligible. We still have two kinematic variables of the reconstructed  $B$  meson candidate available, and one variable based on the event shape, to be used to separate the signal from the remaining background:

- **Energy difference**  $\Delta E = E_B^{cms} - E_{beam}^{cms}$ , where  $E_{beam}^{cms}$  is the beam energy and  $E_B^{cms}$  is the  $B$  candidate energy, both calculated in the CMS. For the signal candidates these two energies are the same, as only a  $B$  meson pair is produced in event. They form a peak around  $\Delta E = 0$ , smeared by the detector energy resolution.
- **Beam energy constrained mass**  $M_{bc} \equiv \sqrt{(E_{beam}^{cms})^2 - (p_B^{cms})^2}$ , where  $p_B^{cms}$  is the  $B$  candidate momentum in the CMS. The signal candidates form a peak around  $M_{bc} = m_B$ , where  $m_B$  is the  $B$  meson mass ( $\simeq 5.279$  GeV).
- **Likelihood ratio**  $LR$ , composed mainly from the event shape variables. It is explained in detail in 6.2.6.

Distributions of the signal and background candidates in the space of these three variables are very different, they are shown in figure 6.8. For the time-dependent part of the analysis (final fit of CPV parameters), we only take the candidates that lie within a  $M_{bc} - \Delta E$  signal region, given by

$$\begin{aligned}
 M_{bc} > 5.27 \text{ GeV}, \quad -0.07 < \Delta E < 0.07 \text{ GeV} & \quad \text{for } \rho \text{ mode,} \\
 M_{bc} > 5.27 \text{ GeV}, \quad -0.10 < \Delta E < 0.08 \text{ GeV} & \quad \text{for } \eta \rightarrow \gamma\gamma \text{ mode,} \\
 M_{bc} > 5.27 \text{ GeV}, \quad -0.08 < \Delta E < 0.06 \text{ GeV} & \quad \text{for } \eta \rightarrow 3\pi \text{ mode.} \quad (6.5)
 \end{aligned}$$

The signal regions were optimized using the same principle as other selection criteria, and are mode dependent due to the difference in energy resolution. The candidates outside the signal region, in a so-called  $M_{bc} - \Delta E$  sideband, are however still used in the next steps of the analysis to determine the properties of background candidates in the signal region.

For the  $\rho^0$  mode candidates we in addition require  $LR > 0.1$ , by which we reject 44% of background and retain 97.5% of signal candidates. This is done for a practical reason, of easier data handling.

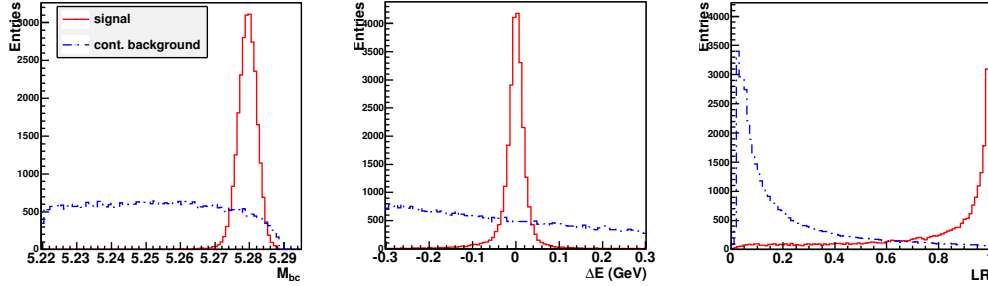


Figure 6.8: Distributions of candidates from signal and continuum background events in  $M_{bc}$ ,  $\Delta E$  and  $LR$ , reconstructed from the MC sample. Distribution of a small fraction of background candidates from the generic  $B\bar{B}$  decays is discussed later.

### 6.2.6 $LR$ - event shape variable

To distinguish between the  $B$  candidates coming from true  $B^0$  decays and the candidates from continuum events, we use the fact that these events have different shapes when looked from the CMS. Because a  $B$  meson pair is produced approximately at rest, its decay products tend to fly randomly in all directions, resulting in a spherical geometry of the events. On the other hand, when a light quark pair is produced in the  $e^+e^-$  collisions, the hadronization products have a large momenta in two opposite directions, resulting in the jet-like shape of the event. This is sketched in figure 6.9. In the following text all the quantities used are calculated in the CMS.

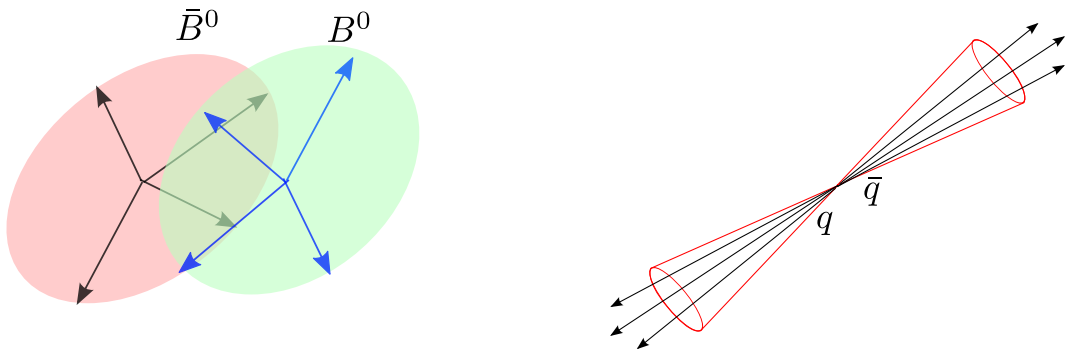


Figure 6.9: Decay products of  $B$  mesons are distributed isotropically, forming the event with spherical geometry. Particles from continuum events form the jet-like geometry of an event.

To mathematically describe and quantify the event shape we define Super-Fox-Wolfram (SFW) moments [45]

$$R_l^{SO,OO} = \frac{\sum_{i,j} |\vec{p}_i| |\vec{p}_j| P_l(\cos \theta_{i,j})}{\sum_{i,j} |\vec{p}_i| |\vec{p}_j|}, \quad (6.6)$$

where  $\vec{p}_i$  is the  $i$ -th particle momentum vector,  $P_l(x)$  is the  $l$ -th Legendre polynomial, and  $\theta_{i,j}$  is the angle between  $\vec{p}_i$  and  $\vec{p}_j$ . By  $SO$  or  $OO$  we denote a group of particles over which the indices  $i, j$  run. For  $SO$  the index  $i$  runs over all particles used to reconstruct the signal candidate, and the index  $j$  runs over all other particles in the event. For  $OO$  both indices run over particles that are not used for the signal candidate reconstruction. Beside the SFW moments, two additional variables, a thrust angle  $\theta_T$  and a transverse sphericity  $S_\perp$  are used. The thrust angle is the angle between the thrust axis of the reconstructed  $B$  meson and the thrust axis of all other particles. The thrust axis is the vector along which the longitudinal projection of normalized momenta,  $\sum_i p_i^L / \sum_i |\vec{p}_i|$ , is maximal. In figure 6.10 we plot the distribution of  $|\cos \theta_T|$  for the signal and continuum background candidates. The transverse sphericity is defined as

$$S_\perp = \frac{\sum_i p_i^\perp}{\sum_i |\vec{p}_i|}, \quad (6.7)$$

where  $p_i^\perp$  is the component of  $\vec{p}_i$  perpendicular to the thrust axis.

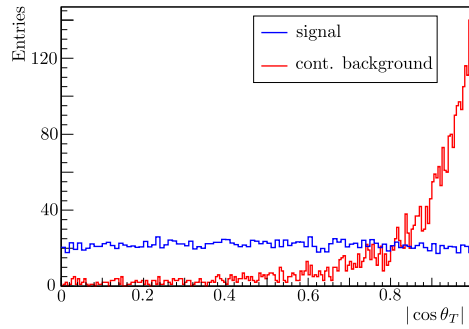


Figure 6.10: Distribution of  $|\cos \theta_T|$  for the signal and continuum background candidates, reconstructed from the MC sample.

Seven of the presented variables are included in the Fisher discriminant [46,47], defined as

$$\mathcal{F} \equiv \sum_{n=2,4} a_n R_n^{SO} + \sum_{n=2,3,4} b_n R_n^{OO} + c |\cos \theta_T| + d S_\perp, \quad (6.8)$$

where only five SFW moments with the greatest  $B\bar{B}$ /continuum separation power are used. The parameters  $a_n, b_n, c$  and  $d$  are optimized with the use of the signal and continuum MC to give the best separation between the candidates from true  $B$  decays and candidates from the continuum events.

---

Besides the Fischer discriminant, the cosines of two additional angles, that utilize characteristic angular distributions of two pseudoscalar mesons from a vector meson decay, are used to form the final  $LR$  variable. One is  $\cos\theta_B$ , where  $\theta_B$  is the angle between  $B$  candidate flight direction and the beam axis ( $z$ ). The other one, used only for the  $\rho^0$  mode, is  $\cos\theta_H$ , where  $\theta_H$  is the angle between  $\pi^+$  direction in the  $\rho^0$  rest frame, and  $\rho^0$  direction in the  $\eta'$  rest frame. For both angles the signal candidates follow a  $(1 - \cos^2\theta)$  distribution, while the background candidates have a flat distribution. The likelihood ratio  $LR$  is formed as

$$LR = \frac{\mathcal{L}_S}{\mathcal{L}_S + \mathcal{L}_B}, \quad \text{with} \quad (6.9)$$

$$\mathcal{L}_{S,B} = \mathcal{P}_{S,B}^{\mathcal{F}} \times \mathcal{P}_{S,B}^{\cos\theta_B} \times \mathcal{P}_{S,B}^{\cos\theta_H} \quad \text{for } \eta' \rightarrow \rho^0\gamma,$$

$$\mathcal{L}_{S,B} = \mathcal{P}_{S,B}^{\mathcal{F}} \times \mathcal{P}_{S,B}^{\cos\theta_B} \quad \text{for } \eta' \rightarrow \pi^+\pi^-\eta,$$

where  $\mathcal{P}_{S,B}^x$  are PDFs for the signal and background candidates in variable  $x$ . The distribution of an  $LR$  composed in this way is shown in figure 6.8.

### 6.3 Signal to background fraction fit

After all the selection criteria imposed, in simulated events we find the purity of selected candidates in the signal region of around 50%. In order to obtain unbiased values of CPV parameters, we have to include this irreducible background in the fit model. To be able to do this, we need to estimate the fraction of signal candidates among all candidates reconstructed from the measured data. As already argued in section 4.1, the best fit sensitivity is achieved if we calculate the signal probability on event-by-event basis. To do this, we study the distribution of the reconstructed  $B$  candidates in the three dimensional  $M_{bc} - \Delta E - LR$  space. In this space the distributions of signal and background candidates differ greatly, demonstrated using simulated distributions in figure 6.8.

First we model the distributions of signal and background candidates in the  $M_{bc} - \Delta E - LR$  space, based on the distributions from the MC sample. Then we build a PDF as a sum of these two models

$$\mathcal{F}(M_{bc}, \Delta E, LR) = f_{sig}\mathcal{F}^{sig}(M_{bc}, \Delta E, LR) + (1 - f_{sig})\mathcal{F}^{bkg}(M_{bc}, \Delta E, LR), \quad (6.10)$$

and determine the signal fraction ( $f_{sig}$ ) by fitting  $\mathcal{F}$  to the  $M_{bc} - \Delta E - LR$  distribution of  $B$  candidates, reconstructed from the measured data. Finally, for each individual candidate with given  $M_{bc}, \Delta E$  and  $LR$ , the signal part of the PDF  $\mathcal{F}$ ,  $f_{sig}\mathcal{F}^{sig}/\mathcal{F}$ , gives the candidate's signal probability.

We now describe the models used for the signal and background distributions. Because the background candidates from the continuum events have a very different distribution from the  $B\bar{B}$  background candidates, we treat them separately.

### 6.3.1 Signal model

To model the distribution of the signal candidates, we use the following PDFs:

- $M_{bc}$  distribution: Gaussian function  $G$ , with mean  $\mu^{mbc}$  and width  $\sigma^{mbc}$  being free parameters,

$$\mathcal{F}^{sig}(M_{bc}) = G(M_{bc}, \mu^{mbc}, \sigma^{mbc}) \quad (6.11)$$

- $\Delta E$  distribution: a sum of a Gaussian function for the main peak, a bifurcated Gaussian function for the tails, and an additional wide Gaussian function for the outliers,

$$\begin{aligned} \mathcal{F}^{sig}(\Delta E) = (1 - f_{out}) & \left[ f_{main} G(\Delta E, \mu_{main}, \sigma_{main}) + (1 - f_{main}) G^{bif}(\Delta E, \mu_{tail}, \sigma_{tail}^L, \sigma_{tail}^R) \right] \\ & + f_{out} G(\Delta E, \mu_{out}, \sigma_{out}), \end{aligned} \quad (6.12)$$

where the fractions  $f_{main}$  and  $f_{out}$ , mean values  $\mu_{main}, \mu_{tail}$  and  $\mu_{out}$ , widths  $\sigma_{main}, \sigma_{tail}$  and  $\sigma_{out}$ , are free parameters.

- $LR$  distribution: for  $\mathcal{F}^{sig}(LR)$  a histogram PDF, obtained from the distribution of signal candidates from the signal MC, is used.

The Gaussian and bifurcated Gaussian functions used are defined as

$$G(x, \mu, \sigma) \equiv \frac{1}{\sqrt{2\pi}\sigma} \exp\left(-\frac{(x-\mu)^2}{2\sigma^2}\right), \quad (6.13)$$

$$G^{bif}(x, \mu, \sigma^L, \sigma^R) \equiv \begin{cases} \frac{2}{\sqrt{2\pi}(\sigma^L + \sigma^R)} \exp\left(-\frac{(x-\mu)^2}{2(\sigma^L)^2}\right), & x \leq \mu \\ \frac{2}{\sqrt{2\pi}(\sigma^L + \sigma^R)} \exp\left(-\frac{(x-\mu)^2}{2(\sigma^R)^2}\right), & x > \mu \end{cases}. \quad (6.14)$$

Reconstruction of all three decay modes involves photons which make the  $\Delta E$  distribution asymmetric, with a stronger tail in the negative side. This is due to the electromagnetic shower leakage in the ECL. For this reason the asymmetric bifurcated Gaussian function is used to model the tails of the  $\Delta E$  distribution.

The final three dimensional PDF is obtained as a product

$$\mathcal{F}^{sig}(M_{bc}, \Delta E, LR) = \mathcal{F}^{sig}(M_{bc}) \times \mathcal{F}^{sig}(\Delta E) \times \mathcal{F}^{sig}(LR), \quad (6.15)$$

as we find no significant correlations between the three distributions. The free parameters of  $\mathcal{F}^{sig}(M_{bc}, \Delta E, LR)$  are determined by a fit of  $\mathcal{F}$  to the distribution of the signal candidates, reconstructed from a large signal MC sample (15 streams). We fit each decay mode ( $\rho^0, \eta \rightarrow \gamma\gamma$  and  $\eta \rightarrow 3\pi$ ) separately, using three different sets of PDF parameters, because the energy resolution of the candidates from each mode is different. The fit results are shown in figure 6.11. One can see that the PDF describes the data distribution well, even at much higher statistics than available from measured data. The values of all parameters, obtained from the fit, are summarized in appendix B.3.

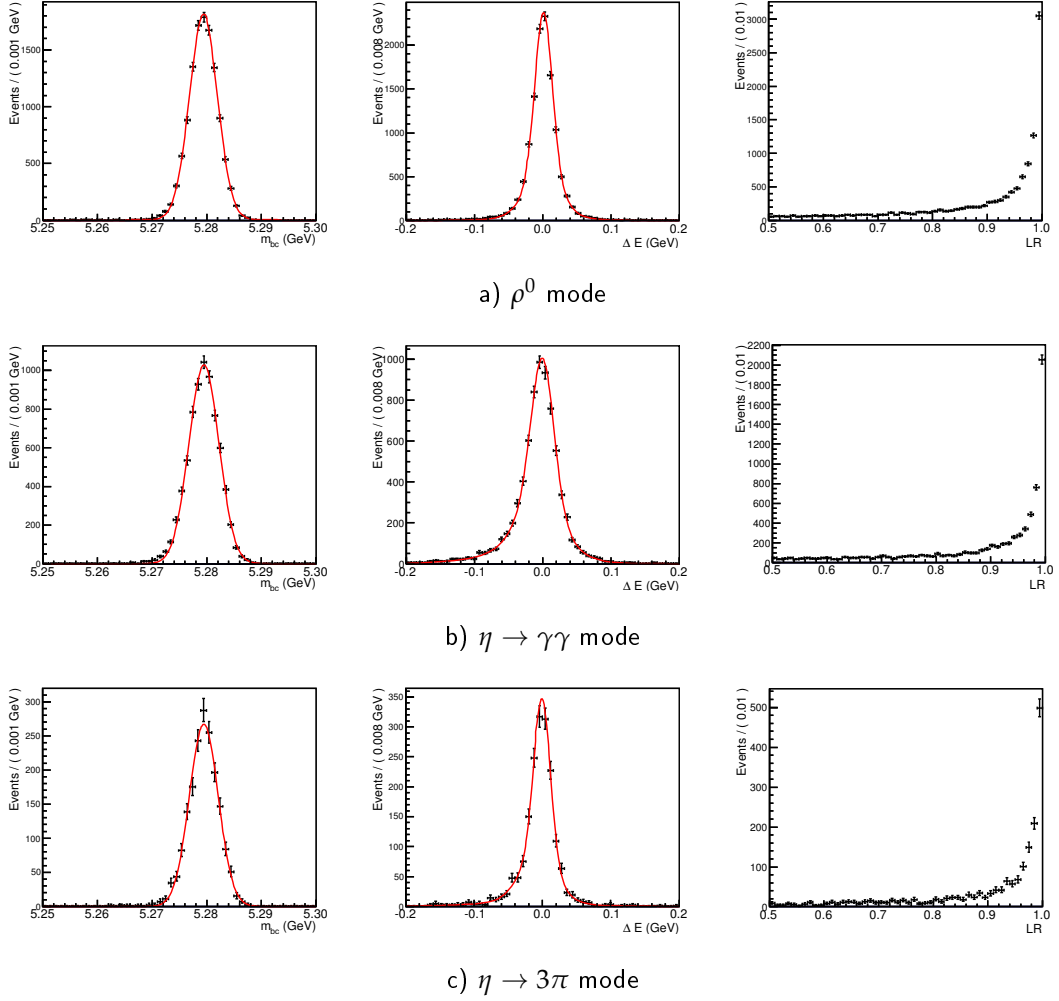


Figure 6.11: One dimensional projections of the fitted  $\mathcal{F}^{sig}(M_{bc}, \Delta E, LR)$  (red line) and the signal candidates distributions (black points), from the signal MC sample. The first column shows projection on the  $M_{bc}$ , the second on the  $\Delta E$ , and the third on the  $LR$ . For the  $LR$  projection no PDF is plotted, because the data points give the PDF itself.

### 6.3.2 Continuum background model

To model the distribution of  $B$  candidates coming from the continuum events the following PDFs are used

- $M_{bc}$  distribution: an ARGUS function [48], defined as

$$\mathcal{F}^{cont}(M_{bc}) = M_{bc} \sqrt{1 - \left(\frac{M_{bc}}{E_{beam}}\right)^2} \exp\left(C \left[1 - \left(\frac{M_{bc}}{E_{beam}}\right)^2\right]\right), \quad (6.16)$$

where  $C$  is a free parameter.

- $\Delta E$  distribution: a first order polynomial is used

$$\mathcal{F}^{cont}(\Delta E) = N(1 + a\Delta E), \quad (6.17)$$

where  $a$  is a free parameter, and  $N$  is a normalization factor.

- $LR$  distribution: histogram PDF is used for  $\mathcal{F}^{cont}(LR)$ . It is obtained from the  $LR$  distribution of  $B$  candidates in the  $M_{bc} - \Delta E$  sideband of measured data events.

The use of the shapes introduced above is motivated by studying the continuum MC sample. While doing this, we also find a non-negligible correlation between the  $\Delta E$  slope ( $a$ ) and the value of  $LR$ . We divide the reconstructed candidates into nine bins, according to the value of  $LR$ , and fit the  $\Delta E$  slope in each bin separately. The results of these fits are shown in figure 6.12.

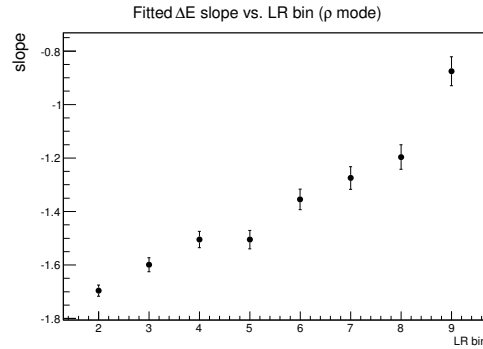


Figure 6.12:  $\Delta E$  slopes obtained from the fits of continuum background candidates (from the MC sample) divided in nine  $LR$  bins. A clear correlation between the slope and the  $LR$  bin number can be seen.

To account for the observed correlation, we parametrize the  $\Delta E$  slope dependency on  $LR$  by a first order polynomial, and correct the  $\Delta E$  PDF to

$$\mathcal{F}^{cont}(\Delta E|LR) = N(1 + a(1 + b LR)\Delta E), \quad (6.18)$$

where  $b$  is the newly introduced parameter. Afterwards, the three dimensional PDF is again obtained as a product

$$\mathcal{F}^{cont}(M_{bc}, \Delta E, LR) = \mathcal{F}^{cont}(M_{bc}) \times \mathcal{F}^{cont}(\Delta E|LR) \times \mathcal{F}^{cont}(LR). \quad (6.19)$$

The free parameters of  $\mathcal{F}^{cont}(M_{bc}, \Delta E, LR)$  are determined during the final signal / background fraction fit, simultaneously with the fraction  $f_{sig}$ .

### 6.3.3 $B\bar{B}$ background model

The  $M_{bc} \times \Delta E \times LR$  distribution of background candidates coming from the generic  $B\bar{B}$  decays does not follow any simple function. The distribution of  $B$  candidates reconstructed from the 10 streams of  $B\bar{B}$  MC sample is shown in figure 6.13. We do not parametrize this distribution, but rather take the tree dimensional histogram from the MC sample for  $\mathcal{F}^{BB}(M_{bc}, \Delta E, LR)$ . Since the number of these candidates is very small for the  $\eta \rightarrow \gamma\gamma$  and  $\eta \rightarrow 3\pi$  modes (even in the 10 streams of the MC sample), the same PDF is used for all three reconstructed modes.

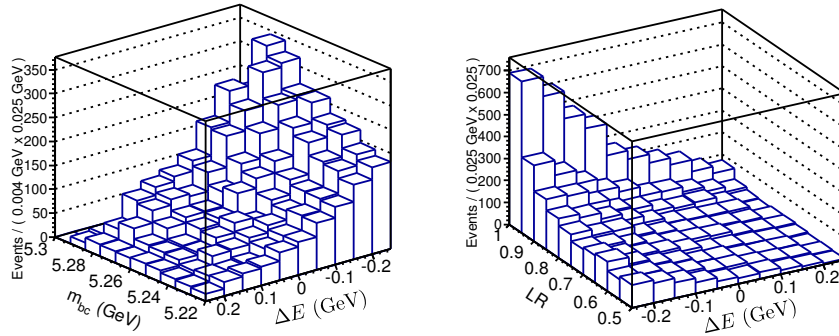


Figure 6.13: Distributions of  $B\bar{B}$  background candidates in the  $M_{bc} - \Delta E$  (left) and in the  $LR - \Delta E$  plane (right), obtained from the 10 streams of generic  $B\bar{B}$  MC sample. The plots show the distribution of candidates combined from all three reconstructed decay modes.

### 6.3.4 Fit procedure

To perform the signal/background fraction fit we divide the reconstructed  $B$  candidates into seven bins ( $r$  bins), according to the quality of the flavor tagging information. In the first  $r$  bin are the candidates with no flavor information, and in the seventh are the candidates with almost unambiguously determined flavor. The details of this binning are described in the flavor tagging section 6.4. As one might expect, a fraction of the signal candidates differs from bin to bin, since the events containing a  $B\bar{B}$  pair are preferred to have good flavor tagging information, compared to the continuum events. We fit the  $(M_{bc}, \Delta E, LR)$  distribution of candidates in each bin separately, and by this gain in the sensitivity for the price of increased fit complexity.

The PDF for the signal/background fraction fit is build as a sum of the signal, continuum background, and  $BB$  background contributions

$$\mathcal{F}^i = f_{sig}^i \mathcal{F}^{sig,i} + (1 - f_{sig}^i) \left[ f_{BB}^i \mathcal{F}^{BB} + (1 - f_{BB}^i) \mathcal{F}^{cont} \right], \quad (6.20)$$

where  $f_{sig}^i$  is the fraction of the signal candidates among all candidates in the  $i$ -th bin, and  $f_{BB}^i$  is the fraction of the candidates that come from the generic  $B\bar{B}$  decays,

among all background candidates in the  $i$ -th bin.  $\mathcal{F}^{sig,i}$ ,  $\mathcal{F}_{cont}$ , and  $\mathcal{F}_{BB}$  are three dimensional ( $M_{bc}, \Delta E, LR$ ) PDFs, as introduced in the previous sub-sections. We use the common  $\mathcal{F}_{cont}$  and  $\mathcal{F}_{BB}$  PDFs for all bins, while for  $\mathcal{F}^{sig,i}$  the  $LR$  part of the PDF is determined for each bin separately. The fractions  $f_{BB}^i$  are fixed to the values obtained from the number of reconstructed  $B$  candidates from the generic  $B\bar{B}$  and continuum MC samples, in each bin. The fit has to be performed simultaneously in all bins because the PDFs  $\mathcal{F}^i$  share common free parameters of the continuum background shape. Together there are twelve free parameters in the fit, three continuum background shape parameters, seven fractions  $f_{sig}^i$ , and we also set free the width and the mean of the  $\Delta E$  main Gaussian function. The latter is done in order to account for the possible difference between the energy resolution in the MC samples and the measured data. To increase the sensitivity of the fit to  $f_{sig}^i$ , the fit is not performed only in the  $M_{bc} - \Delta E$  signal region, but in an extended region defined by

$$M_{bc} > 5.22 \text{ GeV}, \quad -0.25 < \Delta E < 0.25 \text{ GeV} \quad \text{for all decay modes.} \quad (6.21)$$

The presented fit procedure is first tested on the candidates reconstructed from the four streams of the full MC sample. Performing such a test is important because in the fit of the MC sample the obtained signal fractions can be compared with the input (true) values. As an example we show the comparisons of  $f_{sig}^i$  from the fit of the  $\rho^0$  mode candidates, with the MC input values, for each flavor tagging quality bin, in figure 6.14. In addition to the signal fractions, we also plot the obtained number of signal candidates, which is given by  $f_{sig}^i N_B^i$ , where  $N_B^i$  is the number of all candidates in the  $i$ -th bin. We confirm that the numbers from the fit are consistent with the input values.

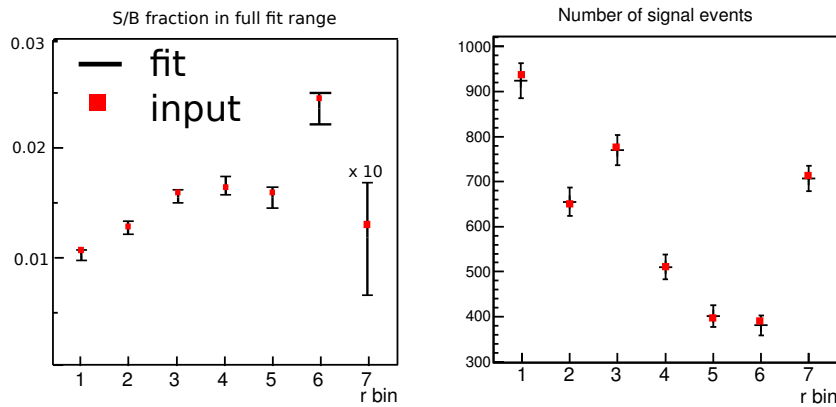


Figure 6.14: Comparison of fractions of the signal candidates in each  $r$  bin ( $f_{sig}^i$ , left plot) as obtained from the fit of the  $\rho^0$  mode candidates, with their true values (input to MC). In the 7th bin the actual fraction is 10 times higher than plotted. The right plot shows the corresponding numbers of the signal candidates in each bin.

### 6.3.5 Fit of the measured data

After the validation of the prepared procedure, we fit the distribution of  $B$  candidates reconstructed from the measured data. The projections of the fitted PDF and the data distribution, for all three reconstructed decay modes, are shown in figure 6.15. It can be seen from the residual plots that the selected PDF describes the data distribution well. The values of all parameters obtained from the fit are given in appendix B.3.2.

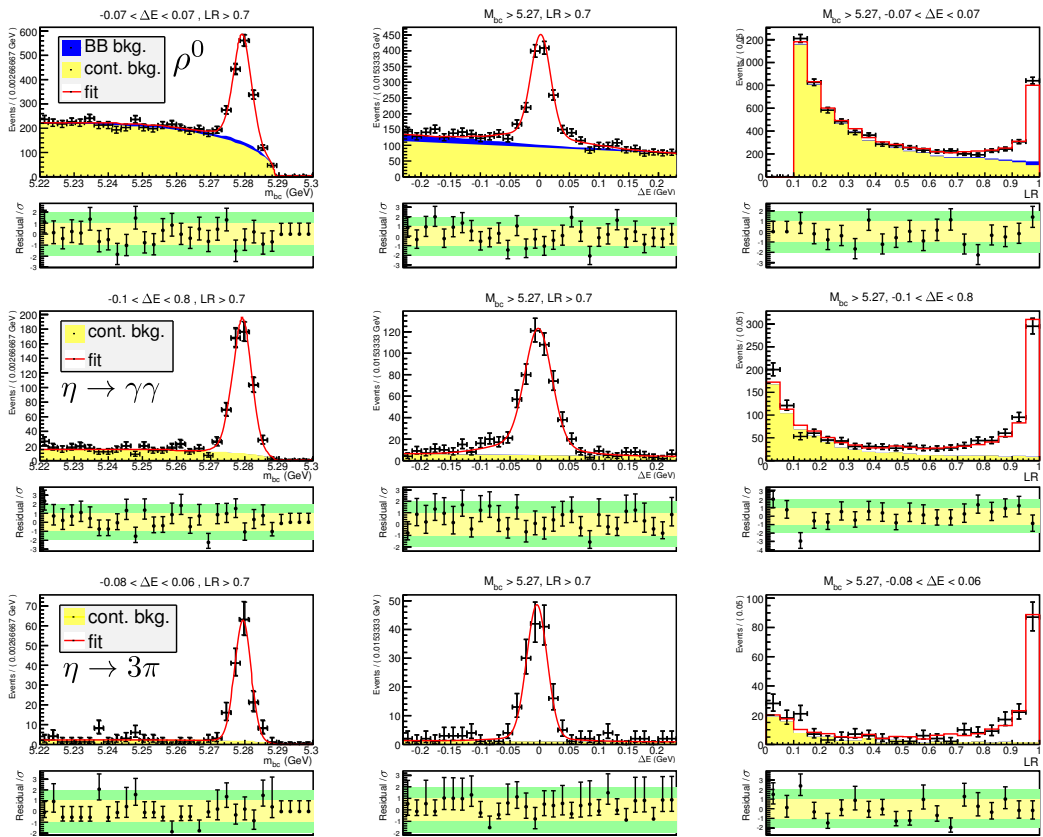


Figure 6.15: One dimensional projections of  $\mathcal{F}$  (red line) to the  $M_{bc}$  (left),  $\Delta E$  (middle), and  $LR$  (right), for all three reconstructed modes. The contributions of  $\mathcal{F}^{cont}$  and  $\mathcal{F}^{BB}$  to  $\mathcal{F}$  are colored in yellow and blue, respectively. Black points show the data distribution. The residual part of each plot shows the deviations of the data distribution from  $\mathcal{F}$ . The PDFs and data distributions plotted are summed over all seven  $r$  bins. The  $M_{bc}$  and  $\Delta E$  distributions are shown for  $LR > 0.7$ , and  $LR$  distribution for the  $M_{bc} - \Delta E$  signal region. The PDFs superimposed are integrated over the corresponding regions.

### Signal yield

To interpret the results of the signal/background fraction fit and describe the quality of our data sample, we calculate the number of signal events in  $M_{bc} - \Delta E$  signal region. This is done by integrating the signal PDF over the signal region as

$$N_{sig} = \sum_i N_B^i f_{sig}^i \iiint_{sig. region} \mathcal{F}^{sig,i}(M_{bc}, \Delta E, LR) dM_{bc} d\Delta E dLR, \quad (6.22)$$

where the sum runs over  $r$  bins, and  $N_B^i$  is the number of all candidates in the  $i$ -th bin. A similar thing is also done to obtain the number of background candidates in the signal region. In table 6.4 we summarize the obtained signal yields and fractions of the background candidates in the signal region, for each of the three reconstructed modes.

In total we have therefore managed to reconstruct about 2233  $B$  candidates in the defined  $M_{bc} - \Delta E$  signal region, coming from the  $B^0 \rightarrow \eta' K_S^0$  decay. We will extract the values of the CPV parameters from their  $\Delta t, q$  distribution. Although the data sample used in this analysis contains about 50% more  $B\bar{B}$  pairs (772 M) than the data sample used in the previous Belle analysis (534 M [35]), we have reconstructed nearly twice as much signal  $B^0$  candidates. This is mainly due to the improvement in the track and the  $K_S^0$  reconstruction efficiency.

mode	signal region				+LR > 0.75		
	$N_{sig}$	$\frac{N_{sig}}{N_B}$	$\frac{N_{cont}}{N_B}$	$\frac{N_{BB}}{N_B}$	$\frac{N_{sig}}{N_B}$	$\frac{N_{cont}}{N_B}$	$\frac{N_{BB}}{N_B}$
$\rho^0$	$1410.5 \pm 48.5$	0.19	0.79	0.02	0.59	0.37	0.04
$\eta \rightarrow \gamma\gamma$	$648.3 \pm 27.9$	0.49	0.50	< 0.01	0.89	0.11	< 0.01
$\eta \rightarrow 3\pi$	$174.3 \pm 13.5$	0.65	0.35	< 0.01	0.94	0.05	< 0.01
sum	$2233.1 \pm 57.6$						

Table 6.4: Obtained signal yields in the signal region for each mode.  $N_B$  is the number of all reconstructed candidates in the  $M_{bc} - \Delta E$  signal region, and  $N_{sig}, N_{cont}, N_{BB}$  are the numbers of candidates of the corresponding type in the signal region. For the right three columns, these numbers are calculated in the part of  $M_{bc} - \Delta E$  signal region with  $LR > 0.75$ . The uncertainties shown are statistical only.

## 6.4 Flavor tagging

The flavor of the reconstructed  $B$  meson ( $B_{CP}$ ) is opposite to the flavor of its accompanying  $B$  meson ( $B_{tag}$ ) in the initially produced  $B\bar{B}$  pair. The flavor of  $B_{tag}$  is determined from the tracks in the event, that are not used for  $B_{CP}$  reconstruction. The algorithm used is common to most of Belle measurements and is described in detail in [49]. It is based on a correlation between the charge of the decay products and the flavor of the decaying  $B$  mesons. In the algorithm several decays with this property are considered. The most important are high momentum lepton tracks from  $B^0 \rightarrow Xl^+\nu$  (or  $\bar{B}^0 \rightarrow Xl^-\nu$ ) decays, and  $K^+$  (or  $K^-$ ) tracks from  $\bar{b} \rightarrow \bar{c} \rightarrow \bar{s}$  ( $b \rightarrow c \rightarrow s$ ) cascade decays. The algorithm combines the results of all categories and tracks considered, and returns two parameters representing flavor information. Discrete parameter  $q$  has value  $+1$  if  $B_{tag}$  is preferably  $B^0$ , and  $-1$  if it is preferably  $\bar{B}^0$ . The second parameter  $r$  summarizes the quality of  $q$  information and can assume continuous value between 0 and 1. It is 0 for no flavor information and 1 for unambiguous flavor assignment.

Beside  $q$ , the fraction of wrongly tagged candidates ( $w$ ) and the difference in fraction of wrongly tagged  $B^0$ 's and  $\bar{B}^0$ 's ( $\Delta w$ ), is needed in the final PDF. We divide the reconstructed  $B$  candidates into seven bins, according to the value of  $r$  as given below, and obtain the  $w$  and  $\Delta w$  for each bin.

rbin	1	2	3	4	5	6	7
r range	0 – 0.1	0.1 – 0.25	0.25 – 0.5	0.5 – 0.625	0.625 – 0.75	0.75 – 0.875	0.875 – 1

For  $w$ 's and  $\Delta w$ 's we use the values obtained by other Belle studies [50–52], as we expect these to be decay mode independent (i.e. the tagging using  $B_{tag}$  decay products is almost independent of the decay product of  $B_{CP}$ ). Their estimation is based on the analysis of self-tagged decays, such as  $B^0 \rightarrow D^{*-}l^+\nu$ ,  $D^{*-}\pi^+$  and  $D^{*-}\rho^+$ . We describe the method of this estimation and give the values of  $w$ 's and  $\Delta w$ 's in appendix B.2. Nevertheless, we confirm using the candidates from the signal MC sample that used wrong tagged fractions are consistent with the values expected specifically for the decay modes under consideration. This comparison is shown in figure 6.16. Similar test for  $\Delta w$ 's (not presented here) also shows consistent values. The values of  $\Delta w$ 's are statistically consistent with zero in our signal MC sample, but measured from the large control sample to be of the order of 1%.

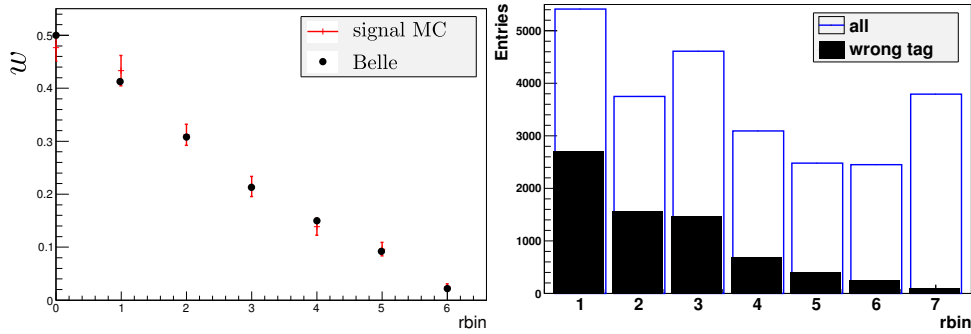


Figure 6.16: **Left:** Comparison of the fractions of wrongly tagged  $B$  candidates from our signal MC and from other Belle studies, in each  $r$  bin. **Right:** Distribution of candidates from the signal MC in  $r$  bins. The black area shows the fraction of wrongly tagged candidates.

## 6.5 Vertex reconstruction

To determine the time interval between the decays of reconstructed  $B$  meson ( $B_{CP}$ ) and accompanying  $B$  meson ( $B_{tag}$ ), we measure the distance between their decay vertices. This two quantities are related by

$$\Delta t \simeq \frac{z_{CP} - z_{tag}}{\gamma\beta c}, \quad (6.23)$$

where  $z_{CP}$  ( $z_{tag}$ ) is the  $z$  coordinate of the  $B_{CP}$  ( $B_{tag}$ ) decay vertex, and  $\gamma\beta = 0.425$  is the boost of the  $B$  meson pair. We first describe the reconstruction of  $B_{CP}$  and then of  $B_{tag}$  vertex.

### 6.5.1 Reconstruction of $B_{CP}$ vertex

To reconstruct the vertex of  $B_{CP}$  we use charged pion tracks, coming either from  $\rho^0$  or  $\eta'$  decay. The lifetime these two intermediate states is so short that their flight length is negligible, so the pion tracks essentially originate from the  $B$  meson decay vertex. The pions from  $K_S^0$  decay are not used because its flight length is of the order of few cm. The principle of the vertex reconstruction is illustrated in figure 6.17. Only well reconstructed tracks, having at least one SVD hit in  $r - \phi$  strips and at least two in the  $z$  strips, are used for vertex reconstruction. The spatial resolution of the tracks having only the CDC, and no associated SVD hits, is too poor to be used. The vertex fitter finds the best estimation for the common origin point of the tracks, by minimizing

$$\chi^2 = \sum_i \Delta x_i^T V_i^{-1} \Delta x_i, \quad (6.24)$$

where  $\Delta x$  is the vector containing the difference between the original and modified track parameters, matrix  $V$  is the corresponding covariance matrix, and the sum runs over all tracks used. To improve the resolution of the vertex fit an additional constraint, so-called *IP tube*, is used in the fit. The IP tube is a virtual tube extending

in the  $z$  direction around the IP. The tube has a Gaussian profile with the width of  $22 \mu\text{m}$  in the radial direction, which is the average flight distance of the  $B$  meson in the  $r - \phi$  plane. The use of IP tube allows us to reconstruct the vertex even in the cases when only one good track (satisfying the SVD hits requirement) is available. In the selected sample there are about 10% of so reconstructed vertices.

The reconstructed vertex position resolution depends on the  $B_{CP}$  decay mode, due to different momenta of the produced pions. In figure 6.18 we plot the distribution of a difference between the reconstructed vertex  $z_{CP}$  and the real vertex  $z_{CP}^{MC}$ , for the candidates reconstructed from the signal MC. We separate the candidates recorded with the use of SVD1 and SVD2, as these two detectors resolutions are different. The typical resolution (RMS) is about  $70 \mu\text{m}$  for  $\rho^0$ ,  $90 \mu\text{m}$  for  $\eta \rightarrow 3\pi$ , and  $100 \mu\text{m}$  for  $\eta \rightarrow \gamma\gamma$  decay mode. The resolution of SVD1 candidates is about 10% worse.

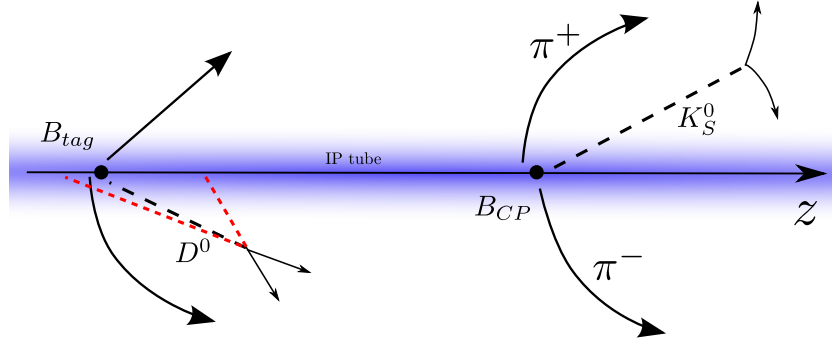


Figure 6.17: The principle of vertex reconstruction.

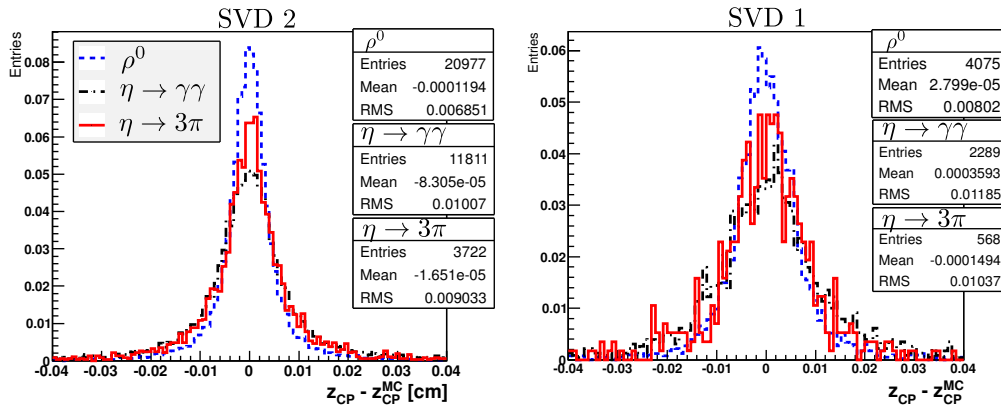


Figure 6.18: Distributions of the difference between  $B_{CP}$  reconstructed decay vertex  $z$  position ( $z_{CP}$ ) and the real decay vertex  $z$  position ( $z_{CP}^{MC}$ ), for candidates reconstructed from the signal MC sample. We separate each decay mode, and the SVD1 (right) and SVD2 (left) candidates.

### 6.5.2 Reconstruction of $B_{tag}$ vertex

To reconstruct the vertex of  $B_{tag}$  the tracks not associated with  $B_{CP}$  reconstruction are used [52]. The same SVD hit requirements as for the  $B_{CP}$  vertexing are imposed, but in addition we also require the track minimal distance from beam axis to be less than 0.5 mm, and the uncertainty of the track  $z$  position to be less than 0.5 mm. This is done to reduce the effect of tracks coming from the decays of secondary particles, like  $D$  and  $K_S^0$  mesons. As illustrated in figure 6.17, these tracks spoil  $B$  vertex resolution, because they originate from the secondary vertex. To further reduce this effect, the vertexing algorithm uses the following strategy. First, all tracks available are used in the vertex fit, and if the obtained reduced  $\chi^2$  is below 20 the vertex is accepted, otherwise the track giving the largest contribution to the  $\chi^2$  (and not being high momentum lepton<sup>4</sup>) is removed from the fit, and the fit is repeated. The procedure is repeated until the reduced  $\chi^2$  drops below 20. In figure 6.19 we plot the distribution of the difference between the reconstructed vertex  $z_{tag}$  and the real vertex  $z_{tag}^{MC}$ , for the candidates reconstructed from the signal MC. The typical resolution of the  $B_{tag}$  vertex is about 95  $\mu\text{m}$ .

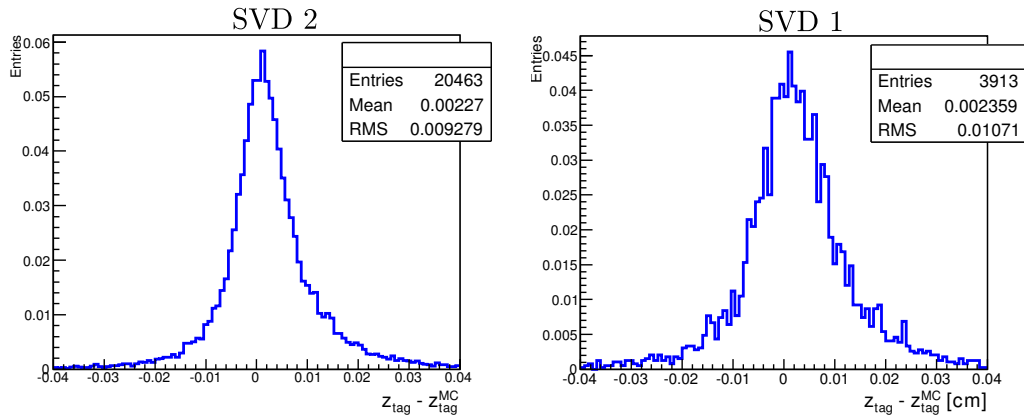


Figure 6.19: Distributions of the difference between the  $B_{tag}$  reconstructed decay vertex  $z$  position ( $z_{tag}$ ) and the real decay vertex  $z$  position ( $z_{tag}^{MC}$ ), for candidates reconstructed from the signal MC sample. We separate SVD1 (right) and SVD2 (left) candidates.

<sup>4</sup>High momentum leptons are very likely to come from  $B$  decay, so they are kept, and the track giving the second largest contribution to the  $\chi^2$  is removed.

---

### 6.5.3 Vertex quality requirements

To discard the candidates with badly reconstructed vertices, we impose the following vertex quality requirements for both  $B_{CP}$  and  $B_{tag}$  vertices:

- Vertex quality
  - $\chi^2/N_{dof} < 50$  (from vertex fit) for the vertices reconstructed with multiple tracks.
  - no selection for the vertices reconstructed with a single track.
- Estimated vertex position uncertainty ( $\sigma_z$ ), obtained from the vertex fit
  - $\sigma_z < 200\mu\text{m}$  for the vertices reconstructed with multiple tracks.
  - $\sigma_z < 500\mu\text{m}$  for the vertices reconstructed with a single track.
- Reconstructed  $|\Delta t| < 70$  ps.

With the above requirements, we find from the signal MC the total vertex reconstruction efficiency to be about 95% for  $B_{CP}$  vertex, and about 93% for  $B_{tag}$  vertex.

## 6.6 Signal $\Delta t$ resolution function

The  $B$  meson decay time is reconstructed with a finite accuracy which is determined by the resolution of the detectors, mainly the SVD detector resolution. The observed  $B$  meson decay time distribution is given by the physics distribution convolved with the  $\Delta t$  resolution function of our detector. A detailed knowledge of the resolution function is hence of outmost importance.

In this work we use the general Belle resolution function, also used in numerous other Belle analyses [53]. Since the resolution function is  $B$  decay mode dependent (it depends on the momentum and the number of tracks used to reconstruct the vertices) we perform several tests to validate the resolution function used. In this section we describe the main features of the resolution function and present the MC validation tests. Additional tests on the measured data are presented in chapter 7.

The resolution function we use is constructed as a convolution of four different contributions

$$\mathcal{R}^{sig}(\Delta t) = \mathcal{R}_{det}^{CP} \otimes \mathcal{R}_{det}^{tag} \otimes \mathcal{R}_{np} \otimes \mathcal{R}_k, \quad (6.25)$$

where  $\mathcal{R}_{det}^{CP}$  and  $\mathcal{R}_{det}^{tag}$  describe the detector resolutions for  $B_{CP}$  and  $B_{tag}$  respectively,  $\mathcal{R}_{np}$  describes the additional smearing of the  $B_{tag}$  vertex due to non-primary tracks, and  $\mathcal{R}_k$  is the contribution coming from the kinematical assumption that a  $B$  meson pair is at rest in the CMS. We present each of these contributions in the next points.

### Detector resolution

$\mathcal{R}_{det}^{CP}$  and  $\mathcal{R}_{det}^{tag}$  describe the resolution of the reconstructed  $z_{CP}$  and  $z_{tag}$ . The vertex position resolution is actually event dependent, because it depends on many event parameters, such as the number of SVD hits, momentum of the tracks, and the direction of the tracks. This motivates the use of event dependent resolution function, that is parametrized as a function of the vertex position uncertainty ( $\sigma_z$ ), obtained from the vertex fit. If  $\sigma_z$  would be the correct uncertainty estimator, a simple Gaussian function with the width  $\sigma_z$  would describe the resolution function. It turns out that this description is not sufficient, so the detector resolution function used is given by

$$\mathcal{R}_{det}^a(x) = G(x; 0, [s_a^0 + s_a^1 h] \sigma_z) \quad (a = CP, tag), \quad (6.26)$$

where  $h \equiv \chi^2 / N_{dof}$  is obtained from the vertex fit, and where we have introduced two scale factors  $s_a^0$  and  $s_a^1$ . The scale factors are determined from a lifetime fit<sup>5</sup>, using the measured  $\Delta t$  distribution of candidates from a large control sample. In such a fit, the full resolution function as given in (6.25) has to be used, but some of its parameters are set free and optimized to correctly describe the data. Different sets of scale factors are used for the resolution functions of candidates recorded with the SVD1 and SVD2 detectors. For the vertices reconstructed with a single track, a slightly modified resolution function is used. It is described in appendix B.2, where also the values of all resolution function parameters are given.

### Non-primary track smearing

The resolution function  $\mathcal{R}_{np}$  is introduced in order to describe the smearing of  $z_{tag}$ , due to tracks that originate from a point displaced from the  $B_{tag}$  vertex. It consists of a prompt component, described by Dirac delta function, and a smeared part. The functional form of the smeared part is obtained from the difference between  $z_{tag}$  reconstructed from the usual MC and a special MC sample, in which the lifetime of all charm and  $K_S^0$  mesons is set to zero. The shape used is given by a sum of Dirac delta function and two exponential components, for positive and negative  $\Delta t$  side,

$$\mathcal{R}_{np}(x) = f_\delta \delta(x) + (1 - f_\delta) \left[ (1 - f_n) E_p(x; \tau_{np}^p) + f_n E_n(x; \tau_{np}^n) \right], \quad (6.27)$$

where

$$E_{p(n)}(x; \tau) \equiv \frac{1}{\tau} \exp\left(\frac{-x}{\tau}\right), \quad \text{for } x > 0 \text{ (} x \leq 0 \text{) and 0 otherwise,} \quad (6.28)$$

$f_\delta$  and  $f_n$  are shape parameters. The effective lifetimes,  $\tau_{np}^p$  and  $\tau_{np}^n$ , are parametrized as functions of  $\sigma_z^{tag}$  and  $h$  from the vertex fit

$$\tau_{np}^{p(n)} = \tau_{p(n)}^0 + \tau_{p(n)}^h h + (\tau_{p(n)}^s + \tau_{p(n)}^{sh} h) \sigma_z^{tag} / (c\beta\gamma), \quad (6.29)$$

<sup>5</sup>The lifetime fit is described in detail in section 7.3.

where  $s_{tag}^0$  and  $s_{tag}^1$  are the scale factors introduced in the previous point, and we have introduced eight additional shape parameters,  $\tau_{p(n)}^0, \tau_{p(n)}^h, \tau_{p(n)}^s, \tau_{p(n)}^{sh}$ . The shape parameters of  $\mathcal{R}_{np}$  are determined by fitting the distribution of the difference between the mentioned MC samples. Again, different sets of parameters are used for the SVD1 and SVD2 candidates, and we show their values in the appendix B.2.

### Kinematic approximation

We calculate the time difference between the decays of  $B_{CP}$  and  $B_{tag}$  by measuring the distance between the decay vertices, and assuming that  $B$  mesons are at rest in the CMS. As this is not exactly true, the value of  $\Delta t$  calculated this way is smeared around its true value  $\Delta t_{true}$ . From the kinematics of  $Y(4S) \rightarrow B\bar{B}$  decay and known beam energies, one can obtain

$$\Delta t_{true} \sim \Delta t - 0.165 \cos \theta_B^{cms} (t_{CP} + t_{tag}), \quad (6.30)$$

where  $\theta_B^{cms}$  is the polar angle of  $B_{CP}$  in the CMS, and  $t_{CP}$  ( $t_{tag}$ ) is the decay time of  $B_{CP}$  ( $B_{tag}$ ). With some more effort the analytic formula for  $\mathcal{R}_k$  [53], which describes this smearing, can be obtained as a conditional probability of obtaining  $x$  given  $\Delta t_{true}$ ,

$$\mathcal{R}_k(x) = \begin{cases} E_{p(n)} \left( x - \left[ \left( \frac{E_B^{cms}}{m_B} - 1 \right) \Delta t_{true} + \frac{p_B^{cms} \cos \theta_B^{cms}}{\beta m_B} |\Delta t_{true}| \right] \right), & \cos \theta_B^{cms} > 0 \text{ } (< 0) \\ \delta^{dirac} \left( x - \left( \frac{E_B^{cms}}{m_B} - 1 \right) \Delta t_{true} \right) \end{cases} \quad (6.31)$$

where  $m_B = 5.279$  GeV,  $E_B^{cms} = 5.292$  GeV, and  $p_B^{cms} = 0.340$  GeV are  $B$  meson mass, energy and momentum in the CMS. Having the physical PDF  $\mathcal{P}^{phys}(\Delta t_{true})$ , we obtain the PDF of the measured distribution by convolution

$$\mathcal{P}^{meas}(\Delta t) = \int \mathcal{P}^{phys}(\Delta t_{true}) \mathcal{R}_k(\Delta t - \Delta t_{true}) d\Delta t_{true}, \quad (6.32)$$

which can be for the case of  $\mathcal{P}^{phys}$  as given in (C.12) calculated analytically.

### 6.6.1 MC validation test

By its definition the resolution function  $\mathcal{R}^{sig}$  should describe the distribution of the difference between the reconstructed  $\Delta t$  and its true value. This can easily be checked on the MC sample, where the information about generated  $\Delta t$  is available. We use  $\Delta t^{MC}$  to denote the generated  $\Delta t$  value. In figure 6.20 the distribution of  $\Delta t - \Delta t^{MC}$  is plotted for the candidates reconstructed from the 15 streams of signal MC. We separate the distributions of the SVD1 and SVD2 candidates. We superimpose the resolution function  $\mathcal{R}^{sig}$  on the simulated data distributions. From the residual plots below each distribution one can see that  $\mathcal{R}^{sig}$  describes the data very well. Note that the

plotted curve has a fixed shape (parameters of  $\mathcal{R}^{sig}$  are fixed from the control sample studies), and is not fitted to the data distribution.

Another important test of the resolution function is given by the lifetime fits. These are presented in chapter 7.

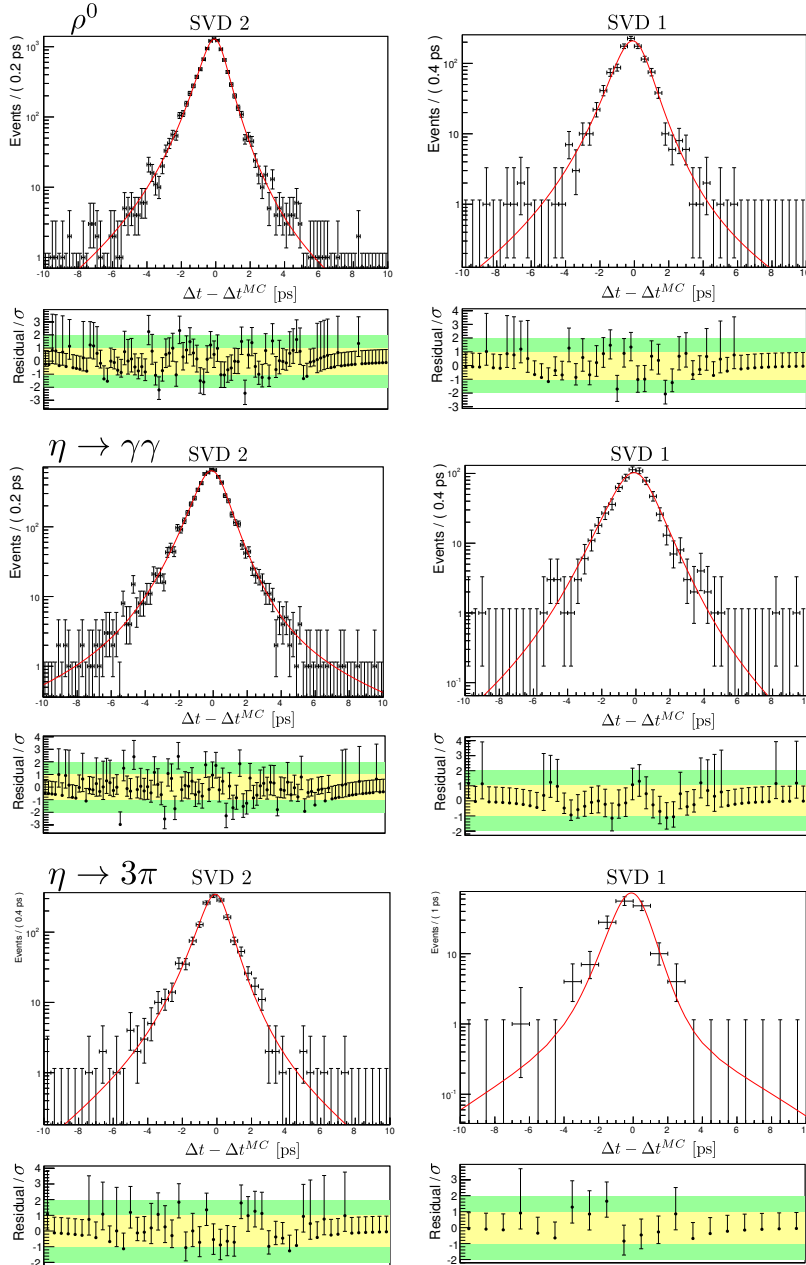


Figure 6.20: Distributions of the difference between reconstructed and generated  $\Delta t$ , for the candidates from the signal MC sample. Reconstructed decay modes, and the SVD 1 and SVD 2 candidates are plotted separately. Superimposed is the resolution function,  $\mathcal{R}^{sig}$ , projected on the data sample of the plotted candidates.

---

## Plotting a conditional PDF

The shape of  $\mathcal{R}^{sig}$  is determined on the event-by-event basis, because it depends on several candidate parameters, such as  $\sigma_z^{CP}$  and  $\sigma_z^{tag}$ . The resolution function plotted in figure 6.20 has to be obtained as a sum of normalized resolution functions of each candidate

$$\mathcal{R}^{plot}(\Delta t - \Delta t^{MC}) = \sum_i \mathcal{R}^{sig}(\Delta t - \Delta t^{MC} \mid (\sigma_z^{CP}, h^{CP}, \sigma_z^{tag}, h^{tag})^i), \quad (6.33)$$

where the sum runs over all candidates. More formally we say that  $\mathcal{R}^{sig}$  is a conditional PDF, depending on the candidate parameters, and normalized for each set of the parameters. When such a PDF is compared with the data distribution (as in figure 6.20) it is obtained as given in (6.33), and we say that it is projected on the data sample.

Basically all PDFs used in this analysis are of this type, and the above procedure is used for all.

## 6.7 Background $\Delta t$ shape

As described in section 6.3, there are three types of  $B$  candidates in the  $M_{bc} - \Delta E$  signal region. Some are signal candidates, but there are also background candidates coming from the continuum and generic  $B\bar{B}$  events. To obtain the correct  $\Delta t$  distribution of the signal candidates (and consequently the correct values of the CPV parameters) we have to know the fraction of background candidates (see section 6.3), as well as their  $\Delta t$  distribution. The determination of the latter is described in the following.

We compose the PDF to describe the background  $\Delta t$  distribution as a convolution of the physics-like part and the resolution function,  $\mathcal{P}^{bkg} = \mathcal{P}_{phys}^{bkg} \otimes \mathcal{R}^{bkg}$ . For the physics-like part we use a sum of the prompt component and the component with a finite (effective) lifetime

$$\mathcal{P}_{phys}^{bkg}(\Delta t) = f_\delta \delta(\Delta t - \mu_\delta) + (1 - f_\delta) \exp\left(-\frac{|\Delta t - \mu_\tau|}{\tau_{bkg}}\right), \quad (6.34)$$

where the fraction  $f_\delta$ , the mean of two components  $\mu_\delta$  and  $\mu_\tau$ , and the effective lifetime  $\tau_{bkg}$ , are the shape parameters. The prompt part describes the candidates from events with charged tracks originating from the IP, and the lifetime part describes the candidates from events containing some intermediate meson states with the effective lifetime  $\tau_{bkg}$ . For the resolution function of the background candidates we use a sum of three Gaussian functions

$$\begin{aligned} \mathcal{R}^{bkg}(\Delta t) = & (1 - f_{out}) [(1 - f_{tail})G(\Delta t, 0, s_{main}\sigma_t) + f_{tail}G(\Delta t, 0, s_{tail}\sigma_t)] \\ & + f_{out}G(\Delta t, 0, s_{out}\sigma_t), \end{aligned} \quad (6.35)$$

where  $\sigma_t = \frac{1}{\beta\gamma c} \sqrt{(\sigma_z^{CP})^2 + (\sigma_z^{tag})^2}$ , with  $\sigma_z^{CP}, \sigma_z^{tag}$  denoting the uncertainties from the vertex fit, and the fractions  $f_{tail}, f_{out}$  and scale factors  $s_{main}, s_{tail}, s_{out}$  are shape parameters. We treat the background from the continuum and generic  $B\bar{B}$  decays separately and compose the full background PDF as

$$\mathcal{P}^{bkg}(\Delta t) = (1 - f_{BB}) \underbrace{\mathcal{P}_{phys}^{cont} \otimes \mathcal{R}^{cont}}_{\mathcal{P}^{cont}} + f_{BB} \underbrace{\mathcal{P}_{phys}^{BB} \otimes \mathcal{R}^{BB}}_{\mathcal{P}^{BB}}, \quad (6.36)$$

where  $f_{BB}$  is the fraction of  $B\bar{B}$  background candidates obtained from the  $B\bar{B}$  and continuum MC samples. Both PDFs, for the continuum and the  $B\bar{B}$  background, have a functional form as given in (6.34) and (6.35), but different set of shape parameters.

Next we describe how the shape parameters of all PDFs that were introduced are determined.

### 6.7.1 $B\bar{B}$ background

For the background candidates from generic  $B\bar{B}$  decays we use the PDF as described above, but without the prompt component in the physics-like part (i.e. we set  $f_\delta = 0$ ). The shape parameters of  $\mathcal{P}^{BB}$  are determined by fitting the  $\Delta t$  distribution of candidates reconstructed from the 10 streams of  $B\bar{B}$  MC sample. Due to low statistics the same set of parameters is used to describe all three reconstructed modes, and the SVD1 and SVD2 candidates. The comparison of fitted  $\mathcal{P}^{BB}$  and the MC candidates distribution is shown in figure 6.21. From the residual plots one can see that  $\mathcal{P}^{BB}$  describes the simulated data well. For  $\eta \rightarrow \gamma\gamma$  and  $\eta \rightarrow 3\pi$  decay mode the description is not perfect, but due to the small number of expected candidates from this source the obtained function is sufficient. The values of all parameters, obtained from the fit, are given in appendix B.3.3.

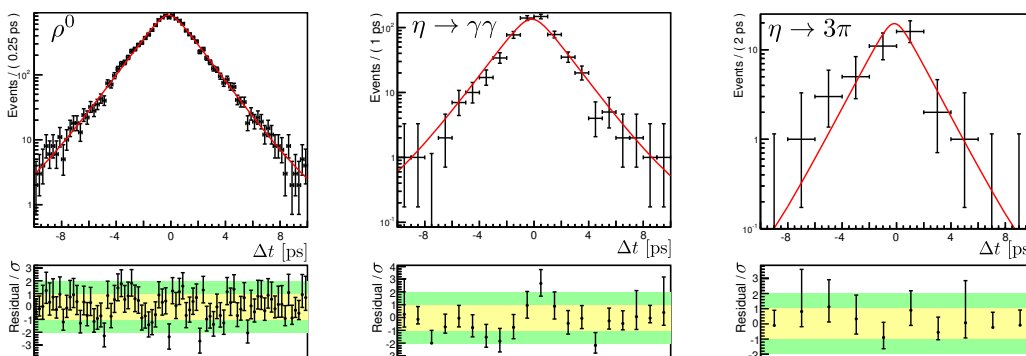


Figure 6.21: Fits of  $\Delta t$  distributions of background candidates from generic  $B\bar{B}$  decays, reconstructed from the generic  $B\bar{B}$  MC sample. The same PDF is used for the distributions of candidates from all three reconstructed decay modes.

## 6.7.2 Continuum background

The shape parameters of the continuum background PDF are determined from the fit of the full background PDF

$$\mathcal{P}^{bkg}(\Delta t) = (1 - f_{BB})\mathcal{P}^{cont} + f_{BB}\mathcal{P}^{BB} \quad (6.37)$$

to the reconstructed candidates in the  $M_{bc} - \Delta E - LR$  sideband of the measured data. In this fit the shape of  $\mathcal{P}^{BB}$  and the fraction  $f_{BB}$  are fixed from the MC (as described before). The sideband used for the fit is defined by  $M_{bc} < 5.265$  GeV,  $-0.1 < \Delta E < 0.25$  GeV and  $LR < 0.9$ , describing a region with very low fraction of  $B\bar{B}$  background candidates. For each reconstructed mode a different set of shape parameters is used, and a common one for the SVD1 and SVD2 candidates. The comparison of fitted  $\mathcal{P}^{bkg}$  and the distribution of candidates from the sideband is shown in figure 6.22. We obtain a good agreement between the PDF and the data distribution for all three decay modes. The obtained values of shape parameters are given in appendix B.3.3.

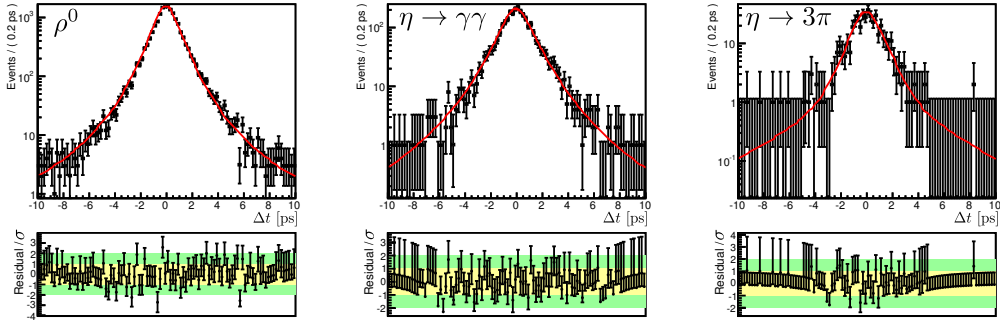


Figure 6.22: Fits of  $\Delta t$  distributions of the candidates from the  $M_{bc} - \Delta E - LR$  sideband of the measured data. These candidates are mainly coming from continuum events (according to MC there is a negligible ( $<1\%$ ) number of the background candidates from generic  $B\bar{B}$  decays and signal candidates ( $<0.1\%$ ) in the region used).

## 6.8 Extraction of CPV parameters

Now that we have all components of the PDF  $\mathcal{P}(\Delta t, q; \mathcal{A}_{\eta'K_S^0}, \mathcal{S}_{\eta'K_S^0})$ , as defined in (6.1), we can use it to extract the values of the CPV parameters. The constructed PDF depends on several observables determined on the event-by-event basis (the signal fraction depends on  $M_{bc}$ ,  $\Delta E$ ,  $LR$ , the shape of the resolution function depends on  $\sigma_z$ , and so on). By this, the available information is used much more efficiently than by using the event independent PDF, obtained by averaging all this information. In this way the fit of the PDF to the measured  $\Delta t, q$  distribution has the maximal sensitivity to the values of the CPV parameters.

The PDF  $\mathcal{P}(\Delta t, q; \mathcal{A}_{\eta'K_S^0}, \mathcal{S}_{\eta'K_S^0})$  gives the probability of obtaining  $\Delta t$  and  $q$ , for given  $\mathcal{A}_{\eta'K_S^0}$  and  $\mathcal{S}_{\eta'K_S^0}$ . However, now we need the opposite. We ask, what are the most likely values of  $\mathcal{A}_{\eta'K_S^0}$  and  $\mathcal{S}_{\eta'K_S^0}$ , given the measured distribution of  $\Delta t$  and  $q$ . To answer this question we construct a *likelihood function* as

$$\mathcal{L}(\mathcal{A}_{\eta'K_S^0}, \mathcal{S}_{\eta'K_S^0}; \{\Delta t_i, q_i\}) = \prod_i \mathcal{P}^i(\Delta t_i, q_i; \mathcal{A}_{\eta'K_S^0}, \mathcal{S}_{\eta'K_S^0}), \quad (6.38)$$

where  $\{\Delta t_i, q_i\}$  is the set of all reconstructed  $B$  candidates'  $\Delta t, q$  values, and the product runs over this set. With  $i$  on  $\mathcal{P}^i$  we stress that the shape of  $\mathcal{P}$  depends on candidate properties. The values of  $\mathcal{A}_{\eta'K_S^0}$  and  $\mathcal{S}_{\eta'K_S^0}$  for which the likelihood function  $\mathcal{L}$  is maximal, are best estimates for the values of these two parameters. In other words, for these values the probability of observing the measured distribution is maximized.

In practice it is usually more convenient to work with so-called *log-likelihood*, which is obtained as  $-2 \ln \mathcal{L}$ , turning the product in (6.38) into a sum. To minimize the log-likelihood function we use MIGRAD algorithm [54], commonly used in high energy physics experiments. Besides the estimated best values of the parameters, the minimizer also returns the statistical uncertainty of the estimation. It is calculated as a difference between the parameter value at minimum and the value at which  $-2 \ln \mathcal{L}$  is increased by one unit. In the limit of a large number of candidates, the likelihood function  $\mathcal{L}$  has a Gaussian shape in the vicinity of the minimum, and the uncertainty corresponds to the width (one standard deviation) of this Gaussian function.

### 6.8.1 Full PDF

In this subsection we summarize the full PDF that is used to extract the CPV parameters. Based on the PDF given in (6.1), and things introduced in this chapter, we can write

$$\begin{aligned} \mathcal{P}(\Delta t, q; \mathcal{A}_{\eta'K_S^0}, \mathcal{S}_{\eta'K_S^0}) &= f_{sig} \mathcal{F}^{sig} \mathcal{P}^{sig}(\Delta t, q; \mathcal{A}_{\eta'K_S^0}, \mathcal{S}_{\eta'K_S^0}) \otimes \mathcal{R}^{sig}(\Delta t) \\ &+ (1 - f_{sig}) \left[ f_{BB} \mathcal{F}^{BB} \mathcal{P}^{BB}(\Delta t) + (1 - f_{BB}) \mathcal{F}^{cont} \mathcal{P}^{cont}(\Delta t) \right], \end{aligned} \quad (6.39)$$

where  $f_{sig}$  is obtained from the signal/background fraction fit,  $f_{BB}$  is fixed from the MC sample, and all PDFs used were introduced in this chapter. Background PDFs  $\mathcal{P}^{BB}$  and  $\mathcal{P}^{cont}$ , defined in (6.36), already include the  $\Delta t$  resolution function, so it is not written explicitly. The PDF  $\mathcal{P}^{sig}$  contains two additional physical parameters beside  $\mathcal{A}_{\eta'K_S^0}$  and  $\mathcal{S}_{\eta'K_S^0}$ , namely  $B^0$  meson lifetime  $\tau_{B^0}$ , and the mass difference  $\Delta M$ . In the fit of the CPV parameters we fix the values of these two parameters to their world average values [24],  $\tau_B^0 = 1.519$  ps and  $\Delta M = 507$  ps<sup>-1</sup>.

---

The components of the PDF (6.39) depend on the following candidate parameters (excluding  $\Delta t, q$ )

$$f_{sig}(\text{r bin, mode}), f_{BB}(\text{r bin, mode}), \mathcal{F}^{sig(cont, BB)}(M_{bc}, \Delta E, LR, \text{r bin, mode}), \quad (6.40)$$

$$\mathcal{P}^{sig}(w), \mathcal{R}^{sig}(\sigma_z^{CP}, \sigma_z^{tag}, h^{CP}, h^{tag}, \cos \theta_B, \text{SVD}\#), \mathcal{P}^{cont(BB)}(\sigma_z^{CP}, \sigma_z^{tag}).$$

When studying the large sample of MC events, a very small fraction ( $\mathcal{O}(10^{-4})$ ) of candidates that cannot be described with the PDF (6.39) is observed. They form a very wide tail in the  $\Delta t$  distribution (with  $\sigma \sim 40$  ps). We describe these by adding the outlier term  $\mathcal{P}_{ol}$  to the PDF (6.39), given by a simple Gaussian function  $G(\Delta t; 0, \sigma_{ol})$ . These outlying candidates arise from badly reconstructed tracks, so we assume an equal fraction of them,  $f_{ol}$ , for the signal and background distributions. The final PDF used in the fit becomes

$$\mathcal{P}^{full}(\Delta t, q; \mathcal{A}_{\eta' K_S^0}, \mathcal{S}_{\eta' K_S^0}) = (1 - f_{ol})\mathcal{P}(\Delta t, q; \mathcal{A}_{\eta' K_S^0}, \mathcal{S}_{\eta' K_S^0}) + f_{ol}\mathcal{P}_{ol}(\Delta t). \quad (6.41)$$

The fraction  $f_{ol}$  and the width  $\sigma_{ol}$  are determined by the lifetime fit of a large control sample. The only free parameters of the PDF (6.41) are the CPV parameters  $\mathcal{A}_{\eta' K_S^0}$  and  $\mathcal{S}_{\eta' K_S^0}$ .

In next chapter we present the tests used to validate the described fit method.



# 7

## Validation tests

Before unblinding the flavor of the candidates reconstructed and selected from the measured dataset of events, we perform several tests of the prepared procedure. These are necessary in order to make sure that the values of the CPV parameters obtained from the fit are unbiased. We use two kinds of tests. First we test the procedure on the MC sample, where the values of the measured CPV parameters can be compared with the generated (true) values. However, due to the possible differences between the simulated and the measured data, it is even more important to test the procedure on the measured data sample. For this purpose we use the control sample and our nominal measured data sample, still being blind to flavor information. In this chapter we first present the tests done on the MC samples and later on the measured datasets.

### 7.1 Signal MC test

We generate six large samples of signal events with different values of generated  $\mathcal{S}_{\eta'K_S^0}^{gen} = (0.0, 0.3, 0.56, 0.67, 0.93, 0.97)$ , and all with  $\mathcal{A}_{\eta'K_S^0}^{gen} = 0.0$ . Each sample contains 15 streams of events. After the reconstruction of  $B$  candidates, flavor tagging and vertices reconstruction, we perform the maximum likelihood fit of the signal PDF  $\mathcal{P}^{sig} \otimes \mathcal{R}^{sig}$  to the obtained  $\Delta t, q$  distribution. We fit the candidates from each decay mode separately and also simultaneously. In figure 7.1, a comparison of the fitted PDF and the candidates distribution in the case of  $\mathcal{S}_{\eta'K_S^0}^{gen} = 0.67$  (which the value obtained from the previous Belle analysis [35]) is shown, for each decay mode. The  $\Delta t$  distribution of the reconstructed candidates with  $q = +1$  and  $q = -1$  is plotted

separately, and the corresponding component of the fitted PDF is superimposed. Below each plot the asymmetry  $a_{\eta'K_S^0}(\Delta t)$ , as defined in (3.18), is plotted. One can see that the distributions and the PDF match well. We commonly use this kind of plot, usually called *CP plot*, to present our results. More importantly, we summarize the results of all fits in figure 7.2. At each value of  $\mathcal{S}_{\eta'K_S^0}^{gen}$  we plot the difference between the CPV parameters obtained from the fit and their generated value, for four cases, separate fits of each decay mode candidates and their simultaneous fit. We then fit the points of the simultaneous fits with a linear function  $\mathcal{S}_{\eta'K_S^0}^{fit} - \mathcal{S}_{\eta'K_S^0}^{gen} = a + b\mathcal{S}_{\eta'K_S^0}^{gen}$  (and equivalently for  $\mathcal{A}_{\eta'K_S^0}^{gen}$ ) to check for the linear response of the fitter to  $\mathcal{S}_{\eta'K_S^0}^{gen}$ . The fit gives the following results

$$\mathcal{S}_{\eta'K_S^0} : a = -0.002 \pm 0.019; b = 0.002 \pm 0.024; \chi^2/N_{dof} = 4.1/4,$$

$$\mathcal{A}_{\eta'K_S^0} : a = -0.007 \pm 0.012; b = 0.014 \pm 0.018; \chi^2/N_{dof} = 2.5/4,$$

with all the values consistent with zero.

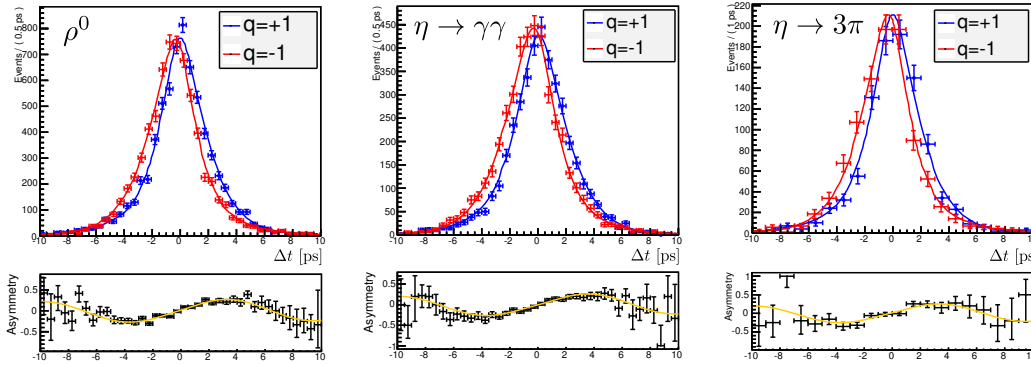


Figure 7.1:  $\Delta t$  distributions of candidates from the signal MC sample, for all three modes. The candidates with  $q = +1$  and the corresponding PDF component are shown in blue, and the candidates with  $q = -1$  are shown in red. Asymmetry  $a_{\eta'K_S^0}(\Delta t)$  is plotted under each plot. Points represent the asymmetry in the data distribution and the line shows the fitted asymmetry  $a_{\eta'K_S^0}(\Delta t) = \mathcal{A}_{\eta'K_S^0} \cos \Delta M \Delta t + \mathcal{S}_{\eta'K_S^0} \sin \Delta M \Delta t$ .

## 7.2 Full MC test

To test the full analysis procedure on a MC sample we prepare three independent MC samples for each generated value of  $\mathcal{S}_{\eta,K_S^0}$ . We add up the background (continuum +  $B\bar{B}$ ) and signal MC in the same ratio as we expect in the measured data. Each sample contains two streams of events.

All PDFs and fractions needed in  $\mathcal{P}^{full}(\Delta t, q)$  (these are  $\mathcal{F}^{sig}$ ,  $\mathcal{F}^{B\bar{B}}$ ,  $\mathcal{F}^{cont}$ ,  $\mathcal{P}^{B\bar{B}}$ ,  $\mathcal{P}^{cont}$ ,  $f_{sig}$  and  $f_{B\bar{B}}$ ) are obtained for each independent sample individually by procedures as described in chapter 6. The distributions that will be taken from the MC sample in

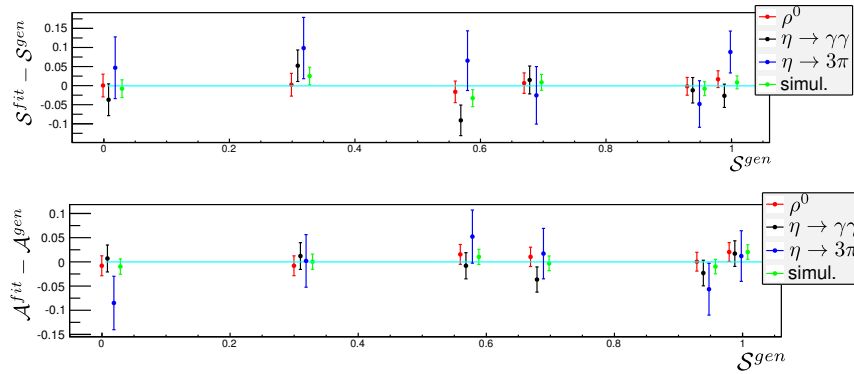


Figure 7.2: Differences between the values of the CPV parameters from the fit and their generated values, from the signal MC sample (15 streams). At each value of the generated  $S$  four results are shown, for separate fits of each decay mode and for the simultaneous fit.

the fit of the measured data (i.e. signal  $LR$ , all distributions for  $B\bar{B}$  background,  $f_{BB}$ ), are here taken from one stream of independent MC sample. This way we fully mimic the procedure that will be used for the measured data fit. The results of simultaneous fits of all decay modes, for all samples, are shown in figure 7.3. The largest deviation of the CPV parameters from the generated values, observed in an individual fit, is about two standard deviations, consistent with expectations.

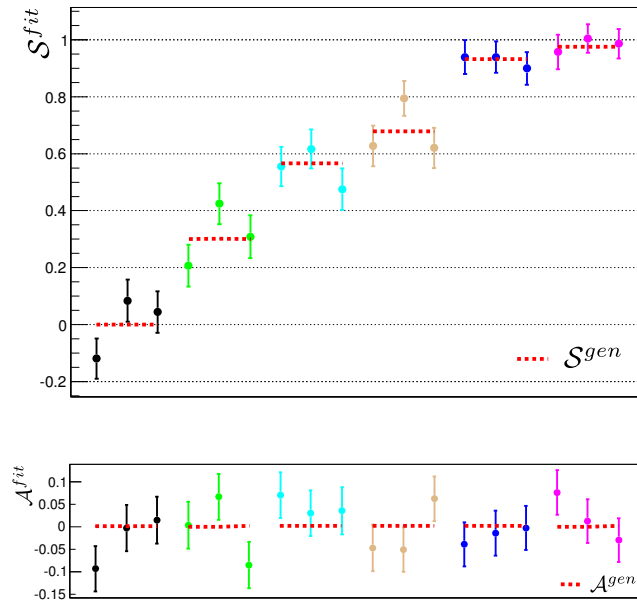


Figure 7.3: Results of fits on the full MC samples. The dotted red line shows the value of generated  $S$  and  $A$ . For each of generated  $S$ , fit is done on three independent samples, each containing two streams of events. The results of simultaneous fits of all three reconstructed modes are shown.

### 7.3 Control sample study

As a control sample we reconstruct the  $B^\pm \rightarrow \eta' K^\pm$  decay from the measured dataset. The reconstruction procedure and the event selection criteria are the same as the ones used for  $B^0 \rightarrow \eta' K_S^0$  decay, described in section 6.2. The only difference is that we take a charged track, for which we demand that  $\mathcal{L}_{K/\pi} > 0.6$ , instead of the reconstructed  $K_S^0$ . The number of reconstructed candidates from this decay is about three times larger than in the case of  $B^0 \rightarrow \eta' K_S^0$  <sup>(1)</sup>. The control sample allows us to test the full analysis procedure, apart from things associated with flavor tagging. Most importantly, the lifetime fit provides a test of the resolution function.

#### Signal/Background fraction fit

The procedure and the PDFs used for the fit are the same as presented in section 6.3. The comparison of the fitted PDFs and data distributions, for all reconstructed modes, is shown in figure 7.5 (next page). The number of signal events of each decay mode in the signal region is

$$\rho^0 : N_{sig} = 4120 \pm 84, \quad \eta \rightarrow \gamma\gamma : N_{sig} = 2169 \pm 53, \quad \eta \rightarrow 3\pi : N_{sig} = 548 \pm 25,$$

where the uncertainties are statistical only. In total we find 6837 signal events.

#### Background $\Delta t$ distribution fit

To determine the shape of the background  $\Delta t$  distribution, we fit the PDF presented in section 6.7 to the  $\Delta t$  distribution of the candidates from the generic  $B\bar{B}$  MC sample for  $\mathcal{P}^{BB}$ , and to the candidates in the  $M_{bc} - \Delta E - LR$  sideband for  $\mathcal{P}^{cont}$  ( $M_{bc} < 5.26$  GeV,  $|\Delta E| < 0.2$  GeV,  $LR < 0.9$ ). The comparisons of obtained PDFs and the data distributions are shown in figure 7.4.

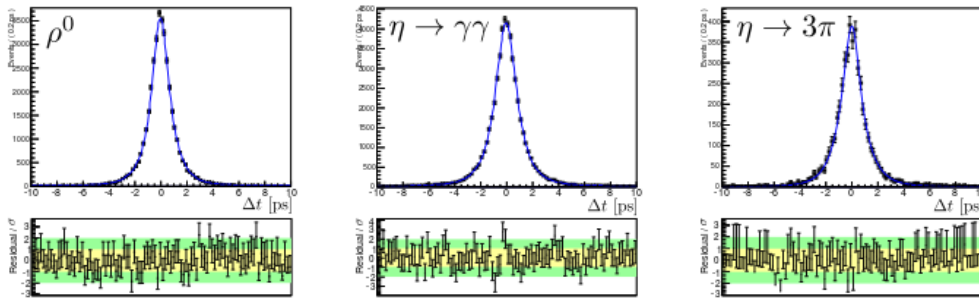


Figure 7.4: Fits of the control sample background  $\Delta t$  distribution of measured data in the sideband ( $M_{bc} < 5.26$  GeV,  $|\Delta E| < 0.2$  GeV,  $LR < 0.9$ ). The left plot is for  $\rho^0$ , middle for  $\eta \rightarrow \gamma\gamma$  and the right for  $\eta \rightarrow 3\pi$  mode.

<sup>1</sup> $K_S^0$  is only half of  $K^0$ , and the reconstruction efficiency is larger for  $K^\pm$  than for  $K_S^0$

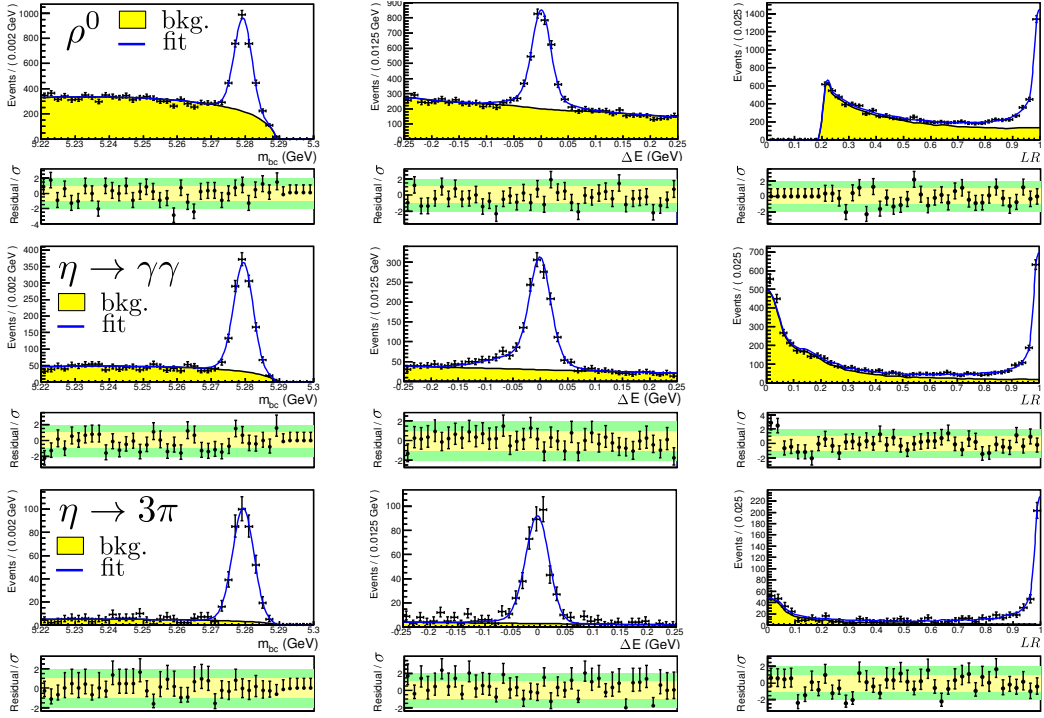


Figure 7.5: Signal/Background fraction fit of the control sample  $B^\pm \rightarrow \eta' K^\pm$ . One dimensional projections of the fitted PDFs (blue line) and measured data distributions (black point) are plotted. The areas colored in yellow show contributions of background events. The first column shows a projection on the  $M_{bc}$  (with  $|\Delta E| < 0.05$  GeV and  $LR > 0.7$ ), the second on the  $\Delta E$  (with  $M_{bc} > 5.27$  GeV and  $LR > 0.7$ ) and the third on the  $LR$  (with  $M_{bc} > 5.27$  GeV and  $|\Delta E| < 0.05$  GeV). The first row shows  $\rho^0$ , the second  $\eta \rightarrow \gamma\gamma$  and the third  $\eta \rightarrow 3\pi$  mode.

### Lifetime fit

Charged  $B$  mesons do not mix, so their  $\Delta t$  distribution is given by a simple exponential decay function, convolved with the  $\Delta t$  resolution function. To perform a lifetime fit we set the  $B^+$  lifetime as a free parameter and fit the measured  $\Delta t$  distribution. The only difference from the fit of the CPV parameters is the signal  $\Delta t$  PDF which is now given by

$$\mathcal{P}_{sig}(\Delta t; \tau_+) = \frac{1}{2\tau_{B^+}} e^{-|\Delta t|/\tau_{B^+}} \otimes R^{sig}(\Delta t), \quad (7.1)$$

with the lifetime  $\tau_{B^+}$  being the only free parameter. To reconstruct the vertex of the  $B^\pm$  meson decaying into  $\eta' K^\pm$ , we use the same tracks as used for  $B^0 \rightarrow \eta' K_S^0$  vertex (i.e. the  $K^\pm$  track is not used in the vertex reconstruction). To obtain the correct  $B$  meson lifetime, the fraction of the background candidates needs to be correctly estimated, the background candidates  $\Delta t$  distribution, and also the signal resolution function, all need to be described correctly. To determine all these things, we use exactly the same procedure as for  $B^0 \rightarrow \eta' K_S^0$ , and the resolution function is the

same in both cases, as the same tracks are used for vertexing. Lifetime fit therefore provides a test of all steps of the analysis, apart from the flavor tagging.

We fit each decay mode separately and do also a simultaneous fit of all modes. In addition, we separate the SVD1 and SVD2 candidates due to the different vertexing resolution. Obtained lifetimes are given in table 7.1. In figure 7.6 we plot the fitted PDF and the distribution of the candidates within the signal region. The lifetime obtained from the simultaneous fit of all reconstructed candidates is

$$\tau_{B^+} = 1.650 \pm 0.027 \text{ ps},$$

where the uncertainty is statistical only, to be compared to the world average value [24],  $\tau_{B^+} = 1.641 \pm 0.008$ .

mode	lifetime $\tau_{B^+}$ [ps]		
	SVD 1	SVD 2	SVD 1 + SVD 2
$\rho^0$	$1.551 \pm 0.085$	$1.638 \pm 0.038$	$1.625 \pm 0.034$
$\eta \rightarrow \gamma\gamma$	$1.880 \pm 0.131$	$1.673 \pm 0.051$	$1.705 \pm 0.048$
$\eta \rightarrow 3\pi$	$1.652 \pm 0.205$	$1.612 \pm 0.092$	$1.611 \pm 0.085$
simul.	$1.667 \pm 0.068$	$1.646 \pm 0.029$	$1.650 \pm 0.027$

Table 7.1: Lifetimes of  $B^\pm$ , obtained from the fit of control sample  $B^\pm \rightarrow \eta' K^\pm$  data. The uncertainties given are statistical only.

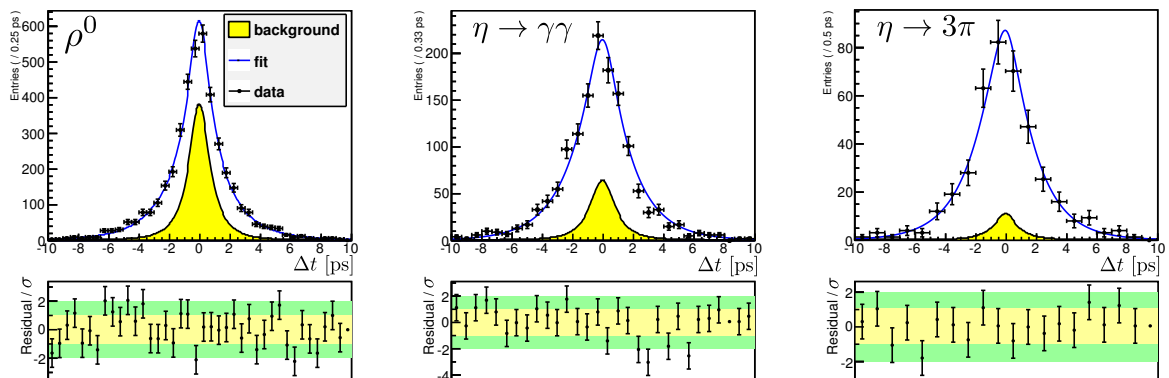


Figure 7.6: Lifetime fits of the control sample candidates. The left plot is for the  $\rho^0$ , the middle for the  $\eta \rightarrow \gamma\gamma$ , and the right one for the  $\eta \rightarrow 3\pi$  mode.

## 7.4 Lifetime fit of $B^0 \rightarrow \eta' K_S^0$ data

A sum of  $\Delta t$  distributions of the reconstructed  $B^0$  and  $\bar{B}^0$  candidates is given by a simple exponential decay function, as one can verify by summing  $\mathcal{P}^{sig}(\Delta t, q = +1)$  and  $\mathcal{P}^{sig}(\Delta t, q = -1)$ . Although still blind to flavor, we can perform the lifetime fit to test a major part of the analysis procedure. The results of signal to background fraction fit and the fit of background  $\Delta t$  distribution were already presented in sections 6.3 and 6.7, so only the results of the lifetime fit are given here. Again we perform individual fits of each decay mode, as well as a simultaneous fit of all candidates. The fit results are summarized in table 7.2. The comparison of fitted PDF and data distribution for each decay mode is plotted in figure 7.7. From the residual plots it can be seen that the PDF describes the data distribution well. From the simultaneous fit of all reconstructed candidates we obtain

$$\tau_{B^0} = 1.494 \pm 0.043 \text{ ps},$$

where the uncertainty is statistical only, and the world average value is  $\tau_{B^0} = 1.519 \pm 0.007 \text{ ps}$  [24].

mode	lifetime $\tau_{B^0}$ [ps]		
	SVD 1	SVD 2	SVD 1 + SVD 2
$\rho^0$	$1.394 \pm 0.128$	$1.558 \pm 0.063$	$1.530 \pm 0.057$
$\eta \rightarrow \gamma\gamma$	$1.374 \pm 0.200$	$1.474 \pm 0.084$	$1.460 \pm 0.077$
$\eta \rightarrow 3\pi$	$1.084 \pm 0.380$	$1.401 \pm 0.142$	$1.371 \pm 0.132$
simul.	$1.371 \pm 0.132$	$1.517 \pm 0.048$	$1.494 \pm 0.043$

Table 7.2: Lifetimes of  $B^0$  obtained from the fits of the measured data. The uncertainties given are statistical only.

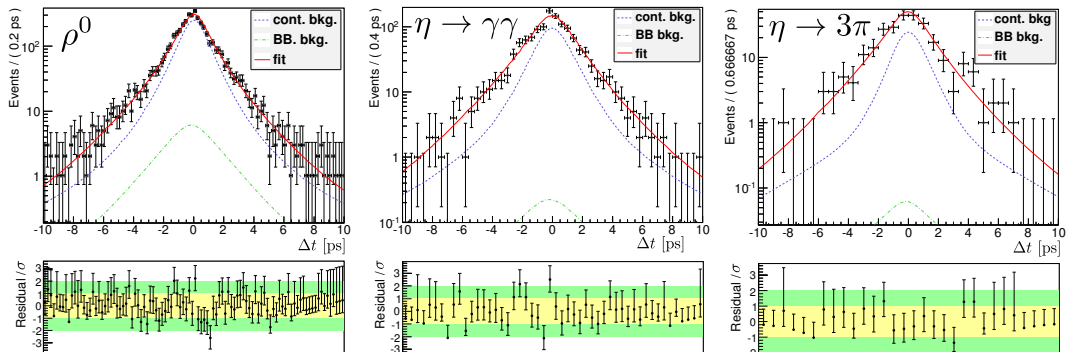


Figure 7.7: Lifetime fits of  $B^0$  candidates from the measured data. The left plot is for  $\rho^0$ , middle for  $\eta \rightarrow \gamma\gamma$  and the right one for  $\eta \rightarrow 3\pi$  mode.

Having done all the tests presented in this chapter, and finding all results consistent with expectations, we are ready perform a fit of the CPV parameters on the candidates reconstructed from the measured data. We present the results in the next chapter.

# 8

## Measurement results

In chapter 6 we have presented the method that allows us to extract the values of the CPV parameters from the  $\Delta t, q$  distribution of reconstructed  $B$  candidates in  $B^0 \rightarrow \eta' K_S^0$  decay. After the extensive validation tests, described in chapter 7, we fix the analysis procedure and apply it to the candidates reconstructed from the Belle final data sample, containing 772 millions  $B\bar{B}$  pairs. As shown in table 6.4, we reconstruct  $2233 \pm 90$  signal candidates (stat. error only). First we fit the candidates of each mode separately, to check the results consistency between the subsamples, and then the simultaneous fit to all candidates is performed. From the simultaneous fit we obtain

$$\begin{aligned}\mathcal{S}_{\eta' K_S^0(\pi^+\pi^-)} &= +0.728 \pm 0.079, \\ \mathcal{A}_{\eta' K_S^0(\pi^+\pi^-)} &= -0.002 \pm 0.054,\end{aligned}$$

where  $(\pi^+\pi^-)$  subscript denotes that  $K_S^0$  was reconstructed from  $\pi^+\pi^-$  pair only. The uncertainties shown are statistical only. We also reconstruct the candidates with  $K_S^0 \rightarrow \pi^0\pi^0$  and include them into the analysis. Details of this addition are given in appendix A. After the reconstruction, the analysis procedure is basically the same as the one used for the candidates with  $K_S^0 \rightarrow \pi^+\pi^-$ , except that we do not reconstruct  $\eta \rightarrow 3\pi$  decay mode (due to low statistics). In total we reconstruct 272 signal candidates with  $K_S^0 \rightarrow \pi^0\pi^0$ , representing about 10% of all reconstructed signal candidates.

The values of the CPV parameters extracted only from  $K_S^0 \rightarrow \pi^0\pi^0$  candidates are

$$\begin{aligned}\mathcal{S}_{\eta'K_S^0(\pi^0\pi^0)} &= +0.576 \pm 0.206, \\ \mathcal{A}_{\eta'K_S^0(\pi^0\pi^0)} &= +0.284 \pm 0.180.\end{aligned}$$

Finally, we perform the fit to all  $K_S^0 \rightarrow \pi^+\pi^+$  and  $K_S^0 \rightarrow \pi^0\pi^0$  candidates simultaneously, to extract the values of the CPV parameters in  $B^0 \rightarrow \eta'K_S^0$  decay, and obtain

$$\begin{aligned}\mathcal{S}_{\eta'K_S^0} &= +0.71 \pm 0.07, \\ \mathcal{A}_{\eta'K_S^0} &= +0.02 \pm 0.05,\end{aligned}$$

where the uncertainties given are statistical only. Estimation of systematic uncertainty is described in section 8.2. In figure 8.1 the background subtracted  $\Delta t$  distributions of the reconstructed  $B$  candidates with  $q = +1$  and  $q = -1$  are shown, with superimposed signal PDF  $\mathcal{P}^{sig}(\Delta t, q)$ . Below the plot, the resulting asymmetry in the distributions,  $a_{\eta'K_S^0}(\Delta t)$ , is shown. We summarize the results of all performed fits in table 8.1.

mode	772 M $B\bar{B}$	
	$\mathcal{S}_{\eta'K^0}$	$\mathcal{A}_{\eta'K^0}$
$B^0 \rightarrow \eta'K_S^0$	$0.711 \pm 0.074$	$+0.021 \pm 0.052$
$K_S^0 \rightarrow \pi^+\pi^-$	$0.728 \pm 0.079$	$-0.002 \pm 0.054$
$\rho^0$	$0.718 \pm 0.098$	$-0.071 \pm 0.069$
$\eta \rightarrow \gamma\gamma$	$0.724 \pm 0.151$	$+0.161 \pm 0.098$
$\eta \rightarrow 3\pi$	$0.800 \pm 0.259$	$-0.058 \pm 0.181$
$K_S^0 \rightarrow \pi^0\pi^0$	$0.576 \pm 0.206$	$+0.284 \pm 0.180$
$B^0 \rightarrow \eta'K_L^0$	$0.458 \pm 0.213$	$+0.088 \pm 0.139$
$B^0 \rightarrow \eta'K^0$	$0.682 \pm 0.070$	$+0.029 \pm 0.049$

Table 8.1: The results of the CPV parameters fits in  $B^0 \rightarrow \eta'K_S^0$  decay. The results of individual decay modes and simultaneous fits are given. Beside our results we show also the result from  $B^0 \rightarrow \eta'K_L^0$  analysis, done by other authors [56]. Expected values of the CPV parameters in this decay are the same as in our analysis, so we combine all the candidates reconstructed with  $K_S^0$  and  $K_L^0$ , and perform the simultaneous fit. We state this result as the values of the CPV parameters in  $B^0 \rightarrow \eta'K^0$  decays. The uncertainties given are statistical only.

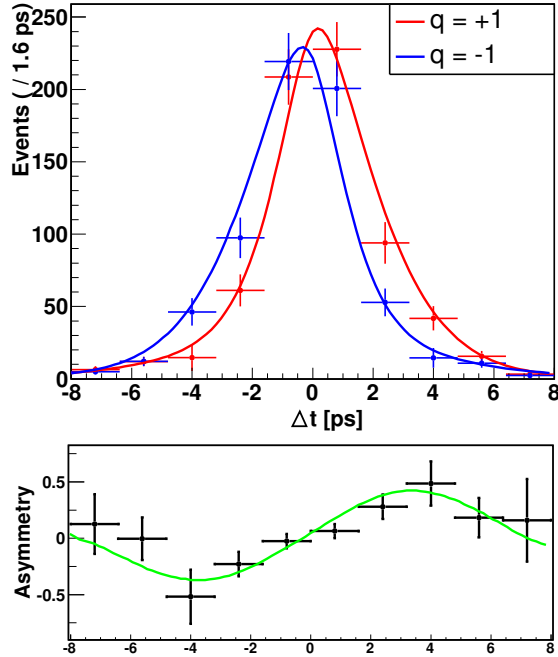


Figure 8.1: Background subtracted plot of the fitted PDF and  $B$  candidates decay time distribution. Blue (red) line and points show PDF and distribution of the reconstructed  $B$  candidates with  $q = -1$  ( $q = +1$ ). The bottom plot shows the asymmetry  $a_{\eta'K_S^0}(\Delta t)$  in the measured data (points) and the fitted theoretical asymmetry (line). All reconstructed decay modes are combined, and only the candidates with well determined flavor are included ( $r > 0.5$ ).

## 8.1 Toy MC ensemble test

To make sure that the statistical uncertainty obtained by the fitter reproduces the expected statistical fluctuation of the fit results<sup>1</sup>, we perform a toy MC study. Based on the sample of the measured  $B$  candidates, we generate a set of 1000 toy MC samples. In these samples, all candidate properties are the same as in the measured sample, but for each candidate its  $\Delta t$  and  $q$  are generated according to the  $\mathcal{P}^i(\Delta t, q; \mathcal{S}_{\eta'K_S^0}, \mathcal{A}_{\eta'K_S^0})$ , where  $i$  represents the  $i$ -th candidate, and the values of the CPV parameters are set to our nominal fit results. We then fit each MC sample separately. Pull distributions ( $(\mathcal{S}_{fit} - \mathcal{S}_{gen})/\sigma_{fit}$ , and equivalently for  $\mathcal{A}$ ) of the obtained fit results for  $\mathcal{S}$  and  $\mathcal{A}$  are shown in figure 8.2. Superimposed are the fits with a Gaussian function, which show that the fit of the CPV parameters is unbiased (Gaussian mean is consistent with zero), and that the uncertainty from the fit correctly estimates the statistical fluctuations of the results (Gaussian width is consistent with one). In figure 8.3 we plot the distribution of uncertainties from the toy MC fits. One can see that the statistical uncertainties from our nominal fit are well within the expected range.

<sup>1</sup>Expected for a fit to as many candidates as used in our nominal fit.

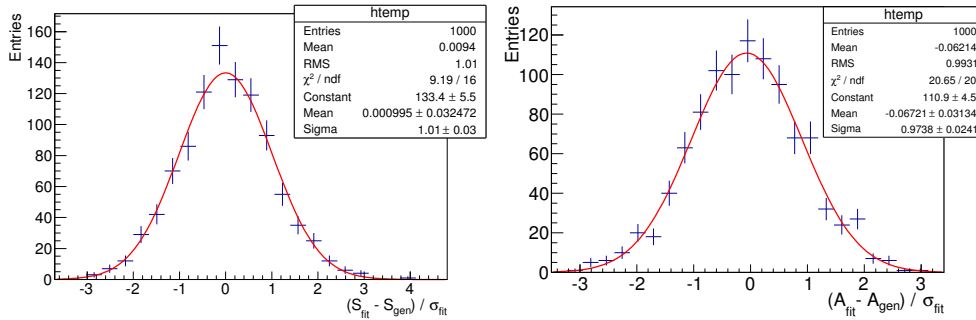


Figure 8.2: Pull distributions of  $\mathcal{S}$  (left) and  $\mathcal{A}$  (right) from the toy MC fits. Both distributions are fitted with a Gaussian function (red line), and parameters from the fit are shown in boxes.

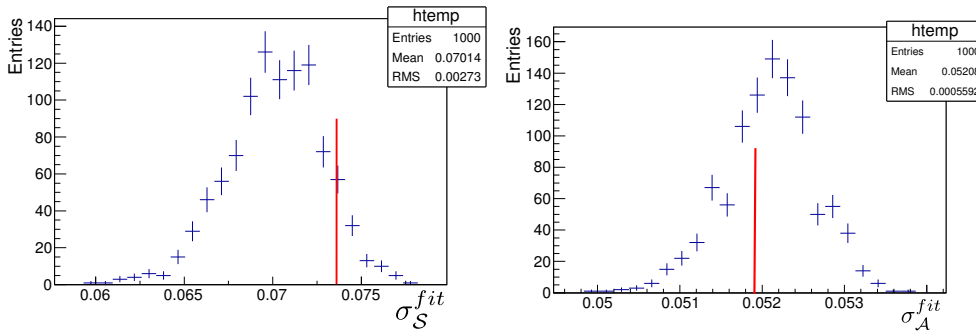


Figure 8.3: Distributions of uncertainties of  $\mathcal{S}$  (left) and  $\mathcal{A}$  (right) from the toy MC fits. The red lines show uncertainties obtained from our nominal fit.

## 8.2 Systematic uncertainty

Many parameters of the PDF  $\mathcal{P}(\Delta t, q; \mathcal{S}_{\eta'K_S^0}, \mathcal{A}_{\eta'K_S^0})$  used to extract the values of the CPV parameters, are fixed to the values obtained from the control sample, or even MC studies. Each of them is of course determined with finite accuracy. In this section we study the effects of these uncertainties on the extracted values of the CPV parameters, representing the systematic uncertainty of our measurement.

The contribution of each parameter's uncertainty is estimated by repeating the fit of the CPV parameters with the corresponding parameter varied for its uncertainty ( $\sigma_i$ ). The difference between the values the CPV parameters obtained this way and their nominal values is taken as a contribution to the systematic uncertainty. To obtain the total systematic uncertainty, all individual contributions are summed in quadrature,  $\sigma = \sum_i \sigma_i^2$ , ignoring possible correlations between them.

### Parameters of PDFs for signal/background fraction fit

- We vary each of the parameters of  $\mathcal{F}^{\text{sig}}$  and  $\mathcal{F}^{\text{cont}}$  for  $\pm\sigma_i$  if the parameter is obtained from the fit of the distribution of measured data, and for  $\pm 2\sigma_i$  if

the parameter is obtained from the fit of MC distributions <sup>2</sup>. Here  $\sigma_i$  is the uncertainty of the parameter from the fit. Altogether, the uncertainty from these parameters is  $\Delta\mathcal{S} = 0.004$  and  $\Delta\mathcal{A} = 0.002$ .

- Varying signal to background fraction  $f_{sig}$  in each flavor quality bin for  $\pm\sigma_i$  gives  $\Delta\mathcal{S} = 0.005$  and  $\Delta\mathcal{A} = 0.003$ .
- The fraction of background candidates coming from  $B\bar{B}$  decays is determined from the MC. To account for the possible difference between MC and measured data we repeat the fit, setting  $f_{B\bar{B}}$  to half and to twice its value from MC. Obtained uncertainty is  $\Delta\mathcal{S} = 0.015$  and  $\Delta\mathcal{A} = 0.004$ .
- The  $LR$  distribution of signal candidates is obtained from the signal MC. Possible difference between the MC and data is studied on the control sample. To obtain the signal candidates  $LR$  distribution from the control sample, we need the  $LR$  distribution of the background candidates, and the fraction of the background candidates in the signal region. For the first one we take the  $LR$  distribution of candidates in the  $M_{bc} - \Delta E$  sideband, and for the second one, we perform the signal/background fraction fit without using  $LR$  (only  $M_{bc}$  and  $\Delta E$  are used). Finally, the  $LR$  distribution of the signal candidates is obtained by subtracting a proper fraction of background  $LR$  from the  $LR$  distribution of all candidates in the signal region. In figure 8.4 the  $LR$  distributions of the signal candidates from signal MC and from control sample are plotted. We repeat the fit of the CPV parameters with the signal  $LR$  distribution modified for the difference between these two distributions. The fit results change for  $\Delta\mathcal{S} = 0.005$  and  $\Delta\mathcal{A} = 0.002$ .

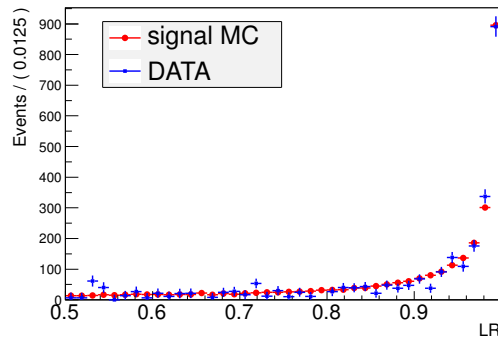


Figure 8.4: Comparison of signal  $LR$  distribution from the MC and the measured data.

<sup>2</sup>the latter is due to historical reasons, and has become a rule within the Belle collaboration in extraction of systematic uncertainties in time-dependent CPV studies of  $B$  mesons

**Background  $\Delta t$  PDF**

We vary each parameter of  $\mathcal{P}^{cont}(\Delta t)$  and  $\mathcal{P}^{BB}(\Delta t)$  for  $\pm\sigma_i$ , where  $\sigma_i$  is the uncertainty of the parameter from the background shape fit. Obtained uncertainty is  $\Delta\mathcal{S} = 0.002$  and  $\Delta\mathcal{A} = 0.001$ .

 **$\Delta t$  resolution function**

We vary each parameter of  $\mathcal{R}^{sig}$  for  $\pm 1\sigma_i$  if it is determined from the measured data study, and for  $\pm 2\sigma_i$  if determined from the MC study. Here  $\sigma_i$  is the uncertainty of the parameter from the fit of the control sample or MC, and includes its statistical and systematic error. Obtained difference is  $\Delta\mathcal{S} = 0.020$  and  $\Delta\mathcal{A} = 0.006$ .

**Flavor tagging**

We vary  $w$  and  $\Delta w$  in each of the tagging quality bins separately for  $\pm\sigma_i$ . Here  $\sigma_i$  is the uncertainty of each fraction, obtained from the fit of the control sample used to determine  $w$  and  $\Delta w$ . Contribution to the systematic uncertainty is  $\Delta\mathcal{S} = 0.006$  and  $\Delta\mathcal{A} = 0.005$ .

**Physics parameters**

We vary the physics parameters that are fixed in our analysis, namely  $\tau_{B^0}$  and  $\Delta m_B$ , for their uncertainties taken from PDG [24]. Obtained uncertainty is  $\Delta\mathcal{S} = 0.002$  and  $\Delta\mathcal{A} = 0.001$ .

**Vertex reconstruction**

- Poor quality vertex rejection: we change the criteria on the vertex fit  $\chi^2/N_{dof} < 50$  to  $\chi^2/N_{dof} < 25$  and  $\chi^2/N_{dof} < 100$ , and the criteria on the uncertainty of vertex  $z$  position from  $z_{err} < 0.02$  cm to no criteria. Obtained uncertainty is  $\Delta\mathcal{S} = 0.010$  and  $\Delta\mathcal{A} = 0.007$ .
- We change  $\Delta t$  fit range from  $|\Delta t| < 70$  ps to  $|\Delta t| < 40$  ps and  $|\Delta t| < 100$  ps. Obtained uncertainty is  $\Delta\mathcal{S} < 0.001$  and  $\Delta\mathcal{A} < 0.001$ .
- We change the radial smearing (in  $r - \phi$  plane) of the IP tube used in the vertex fit from 21  $\mu\text{m}$  to 11  $\mu\text{m}$  and 41  $\mu\text{m}$ . Obtained uncertainty is  $\Delta\mathcal{S} = 0.003$  and  $\mathcal{A} = 0.002$ .
- We change the track rejection criteria for  $B_{tag}$  vertex reconstruction from  $dr < 0.05$  cm to  $dr < 0.04$  cm and  $dr = 0.06$  cm, and from  $\sigma_z < 0.05$  cm to  $\sigma_z < 0.04$  cm and  $\sigma_z < 0.06$  cm. Obtained difference in fit results is  $\Delta\mathcal{S} = 0.003$  and  $\mathcal{A} = 0.001$ .

- 
- As an estimation of uncertainty due to imperfect SVD alignment we use the result of other Belle studies. This uncertainty is expected to be decay mode independent. It is obtained from a special MC sample, with the modified SVD alignment. We set  $\Delta\mathcal{S} = 0.006$  and  $\mathcal{A} = 0.004$ .
  - Small biases are observed in  $\Delta z$  measurements in  $e^+e^- \rightarrow \mu^+\mu^-$  and control samples. To account for the possible systematic uncertainty from this source we use the uncertainty obtained from other Belle studies. This uncertainty was estimated by applying special  $\Delta z$  correction functions, repeating the fit, and comparing the obtained results. Obtained values are  $\Delta\mathcal{S} = 0.005$  and  $\mathcal{A} = 0.007$ .

### Tag side interference

The interference between CKM-favored  $b \rightarrow c\bar{u}d$  and doubly CKM suppressed  $b \rightarrow u\bar{c}d$  amplitudes in the tagging side  $B$  can effect time dependent CPV measurements [55]. It introduces a small correction to the signal  $\Delta t$  PDF, which was neglected in  $\mathcal{P}^{sig}$ . To estimate the effect of this correction, we generate a large sample of toy MC pseudo-experiments with the corrected PDF. Then we fit the obtained  $\Delta t, q$  distributions with non-corrected PDF (same as used in nominal fit), and check for the difference between the generated and fitted values of the CPV parameters. This way we obtain  $\Delta\mathcal{S} = 0.002$  and  $\Delta\mathcal{A} = 0.020$ .

All above presented contributions are summarized in table 8.2. Summing all contributions in quadrature we obtain

$$\Delta\mathcal{S}^{syst} = 0.031 \quad \text{and} \quad \Delta\mathcal{A}^{syst} = 0.027, \quad (8.1)$$

which we state as the systematic uncertainty of our measurement.

source	$\Delta\mathcal{S}$	$\Delta\mathcal{A}$
$\mathcal{F}^{sig}, \mathcal{F}^{cont}$ parameters	0.004	0.002
fractions $f_{sig}^i$	0.005	0.003
fractions $f_{BB}^i$	0.015	0.004
signal $LR$ PDF	0.005	0.002
background $\Delta t$ PDF	0.002	0.001
$\Delta t$ resolution	0.020	0.006
flavor tagging	0.006	0.005
physics parameters	0.002	0.001
poor quality vertex rej.	0.010	0.007
$\Delta t$ range	< 0.001	< 0.001
IP tube	0.003	0.002
$B_{tag}$ track rej.	0.003	0.001
SVD missalignment	0.006	0.004
$\Delta z$ bias	0.005	0.007
tag-side interference	0.002	0.020
TOTAL	0.031	0.027

Table 8.2: Summary of systematic uncertainty contributions from different sources.

# 9

## Conclusion

We measured the values of the CPV parameters in  $B^0 \rightarrow \eta' K_S^0$  decays. The results were obtained from the Belle final data sample, containing  $772 \times 10^6$   $B\bar{B}$  pairs collected at the  $Y(4S)$  resonance with the Belle detector at the KEKB asymmetric  $e^+e^-$  collider. The final result of the measurement is

$$\begin{aligned} \mathcal{S}_{\eta' K_S^0} &= +0.71 \pm 0.07(stat) \pm 0.03(syst), \\ \mathcal{A}_{\eta' K_S^0} &= +0.02 \pm 0.05(stat) \pm 0.03(syst), \end{aligned}$$

including statistical and systematic uncertainty. Our measurement gives the world's most precise values of  $\mathcal{S}_{\eta' K_S^0}$  and  $\mathcal{A}_{\eta' K_S^0}$  to date, which are also the most precisely determined values of the CPV parameters among all  $b \rightarrow s\bar{q}q$  penguin dominated decay modes of  $B^0$  mesons. In figure 9.1 we compare the above result with the previous Belle and BaBar measurement results, and the world average values of the CPV parameters in  $B^0 \rightarrow c\bar{c}K^0$  decays. We find our result consistent with the previous Belle and BaBar measurements. There is no statistically significant deviation from the values of the CPV parameters in  $B \rightarrow c\bar{c}K^0$  decays, which is consistent with the SM predictions for  $\mathcal{S}_{\eta' K_S^0}$  and  $\mathcal{A}_{\eta' K_S^0}$ .

### Future prospects

In the past decade the KM mechanism, with a single irreducible CP violating complex phase, was experimentally firmly established as the main source of CP violation. After the great excitement in the early years of  $B$  factories operation, when some large deviations of the CPV parameters in  $b \rightarrow s\bar{q}q$  dominated modes from

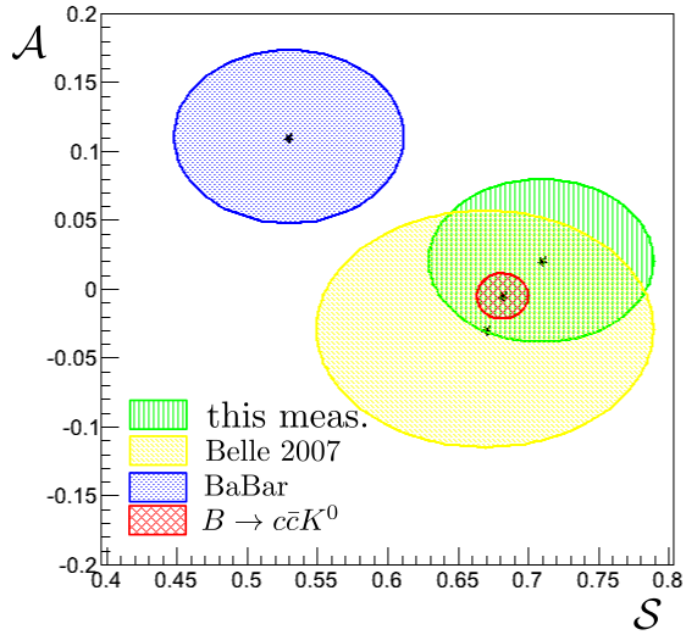


Figure 9.1: Comparison of our measurement result with the previous Belle [35] and BaBar [36] measurements. In addition we plot the value of the CPV parameters in charmed  $B \rightarrow c\bar{c}K^0$  decays, representing the SM expectation value for our result.

the predicted values were observed, we find today the former statement true not only for the tree dominated  $B^0$  decays, but also for these, to new physics sensitive decay modes. However, relatively large experimental uncertainties on the values of the CPV parameters in  $b \rightarrow s\bar{q}q$  modes still leave space for sizable new physics contributions. Beside the fact that in many models of new physics such contributions arise naturally at the few percent level, they are also necessary to explain the matter-antimatter asymmetry of the universe. This motivates further measurements of the CPV parameters in these modes, with the difference  $\Delta\mathcal{S} = \mathcal{S}_{b \rightarrow s\bar{q}q} - \mathcal{S}_{J/\psi K^0}$  as one of gold-plated observables to search for new CP violating phases, also at the future SuperKEKB collider and Belle II detector [57,58]. The SuperKEKB/Belle II (upgrade of the KEKB collider and the Belle detector) plan to start the operation in 2016, and achieve the integrated luminosity of  $50 \text{ ab}^{-1}$  by 2023. The planned peak and integrated luminosity curves are shown in figure 9.2. The uncertainties of the CPV parameters in most of the  $b \rightarrow s\bar{q}q$  decay modes are dominated by statistical uncertainties, so the luminosity increase is the only way to clarify the current experimental situation, either by discovering new CP violating phases, or further constraining and possibly rule out some new physics models. In figure 9.3 the projected  $\Delta\mathcal{S}$  uncertainty as a function of integrated luminosity is shown, for  $B^0 \rightarrow \eta'K^0, \phi K^0, K_S^0 K_S^0 K_S^0$  decay modes [59]. With an integrated luminosity of  $50 \text{ ab}^{-1}$  the  $\Delta\mathcal{S}$  in  $\eta'K_S^0$  can be

measured with an accuracy of  $\mathcal{O}(0.01)$ , i.e. at the level of the SM predictions.

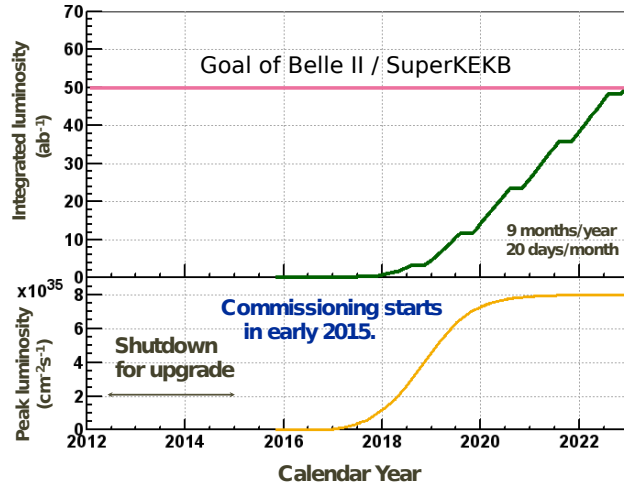


Figure 9.2: Planned peak and integrated luminosity curves of the SuperKEKB / Belle II project.

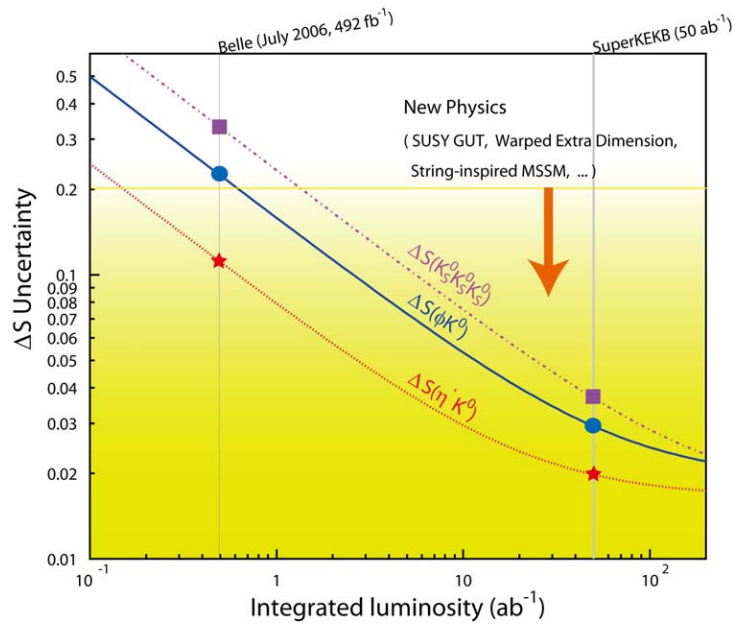


Figure 9.3:  $\Delta S$  uncertainty as a function of integrated luminosity at the Belle II experiment, for  $B^0 \rightarrow \eta' K^0, \phi K^0, K_S^0 K_S^0 K_S^0 K_S^0$  decays [59]. Statistical and systematic uncertainties are included.





## Analysis with $K_S^0 \rightarrow \pi^0\pi^0$

The  $K_S^0$  meson decays in about 70% to  $\pi^+\pi^-$  and in 30% to  $\pi^0\pi^0$ . To reduce the statistical uncertainty of fitted CPV parameters we also include the latter decay into the analysis. Here we describe the  $K_S^0 \rightarrow \pi^0\pi^0$  decay reconstruction and selection, and present the validation tests of the analysis with this decay mode.

### A.1 Event reconstruction and selection

To reconstruct  $K_S^0 \rightarrow \pi^0\pi^0$  decay we first reconstruct  $\pi^0$  candidates by combining two photons with  $E_\gamma > 0.05$  GeV. For a photon pair we require an invariant mass of  $0.08 < M_{\gamma\gamma}^{\pi^0} < 0.15$  GeV and a momentum above 0.1 GeV, to be used as a  $\pi^0$  candidate. At this point the decay vertex of  $\pi^0$  is assumed to be the IP. To obtain  $K_S^0$  candidates from pairs of  $\pi^0$ s we perform a kinematic fit that constrains the pion pair to arise from the common vertex (which can be displaced from the IP), the resulting  $K_S^0$  to originate from the IP, and the  $\pi^0$  invariant mass to its nominal value. After the fit, the candidates with the invariant mass  $0.48 < M_{\pi^0\pi^0}^{K_S^0} < 0.52$  GeV and  $\chi_{fit}^2/N_{dof} < 10$  are selected for further analysis.

To reconstruct  $\eta'$  the method and selection criteria are the same as presented in section 6.2, except that we do not reconstruct the  $\eta \rightarrow 3\pi$  decay mode, due to low statistics. The  $M_{bc} - \Delta E$  signal region is given by  $M_{bc} > 5.27$  GeV and  $-0.15 < \Delta E < 0.1$  GeV for both,  $\rho^0$  and  $\eta \rightarrow \gamma\gamma$ , decay modes.

## A.2 Signal to background fraction fit

The procedure for the signal/background fraction fit is the same as used in the  $K_S^0 \rightarrow \pi^+ \pi^-$  case, presented in 6.3. For all distributions we use the same models, but with different sets of shape parameters. The shape parameters of the signal candidates  $M_{bc} \times \Delta E \times LR$  distribution are obtained from the fit of the signal MC. The fit results are shown in figure A.1, and the obtained PDF parameters are given in appendix B.3. The shape parameters of the continuum background model are determined during the fit of candidates from the measured events, simultaneously with signal fraction. The model for background from the generic  $B\bar{B}$  decays is obtained from the MC sample. The results of signal/background fraction fit of candidates from the measured events are shown in figure A.2. It can be seen from residual plots that the selected model describes the data distribution well. The obtained PDF parameters are given in appendix B.3.2.

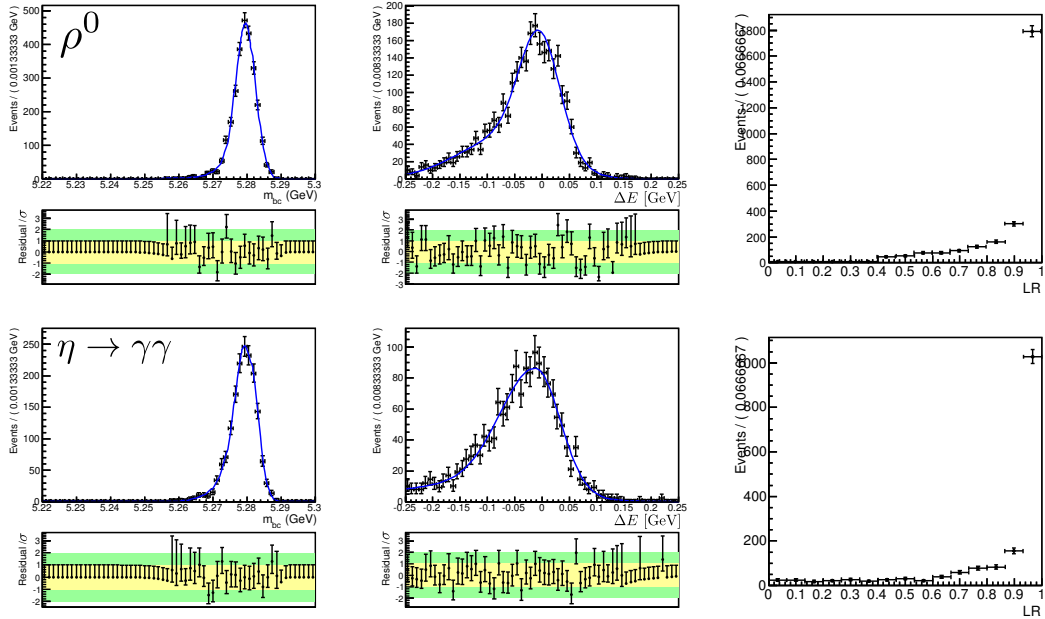


Figure A.1: One dimensional projections of the fitted  $\mathcal{F}^{sig}(M_{bc}, \Delta E, LR)$  (blue line) and the signal candidates distributions (black points), from the signal MC sample. The first column shows projection on the  $M_{bc}$ , the second on the  $\Delta E$ , and the third on the  $LR$ . For the  $LR$  projection no PDF is plotted, because the data points give the PDF itself.

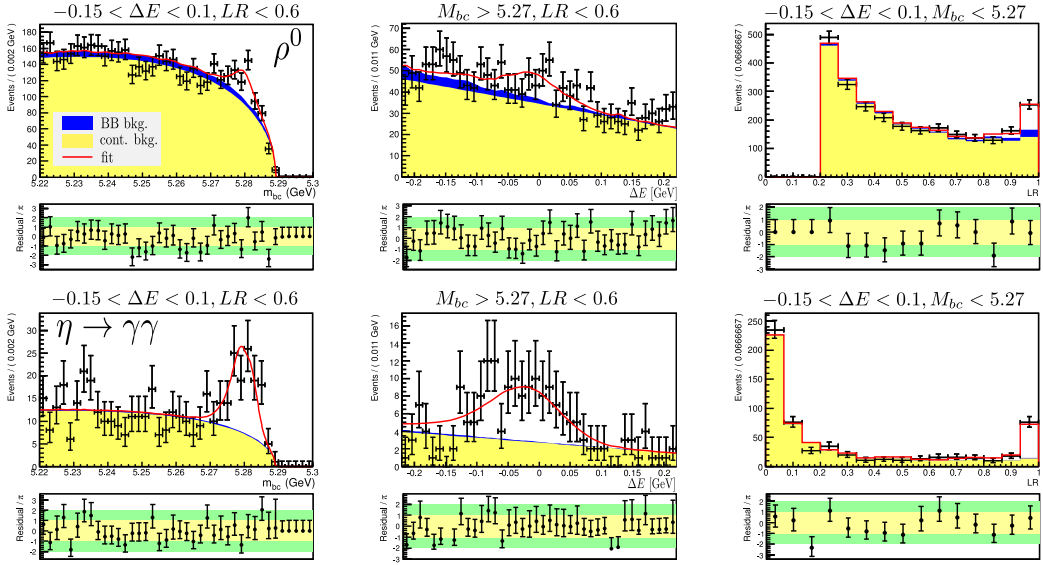


Figure A.2: One dimensional projections of  $\mathcal{F}$  (red line) to the  $M_{bc}$  (left),  $\Delta E$  (middle), and  $LR$  (right), for both reconstructed decay modes with  $K_S^0$ . The contributions of  $\mathcal{F}^{cont}$  and  $\mathcal{F}^{BB}$  to  $\mathcal{F}$  are colored in yellow and blue, respectively. Black points show the data distribution. The PDFs and data distributions plotted are summed over all seven  $r$  bins. The used  $M_{bc}, \Delta E, LR$  regions are shown above each plot.

## Signal yield

The number of signal candidates in the signal region, obtained by integrating the signal part of PDF  $\mathcal{F}$ , is shown in table A.1. In addition, we also show the fraction of background candidates in the signal region. In total we have reconstructed about 272 signal candidates.

mode	signal region				+LR > 0.75		
	$N_{sig}$	$\frac{N_{sig}}{N_B}$	$\frac{N_{cont}}{N_B}$	$\frac{N_{BB}}{N_B}$	$\frac{N_{sig}}{N_B}$	$\frac{N_{cont}}{N_B}$	$\frac{N_{BB}}{N_B}$
$\rho^0$	$168.2 \pm 21.4$	0.04	0.93	0.03	0.13	0.80	0.07
$\eta \rightarrow \gamma\gamma$	$104 \pm 14.2$	0.16	0.84	< 0.01	0.65	0.34	< 0.01
sum	$272 \pm 25.7$						

Table A.1: Obtained signal yields in the signal region for both decay modes with  $K_S^0 \rightarrow \pi^0 \pi^0$ .  $N_B$  is the number of all reconstructed candidates in the  $M_{bc} - \Delta E$  signal region, and  $N_{sig}, N_{cont}, N_{BB}$  are the numbers of candidates of the corresponding type in the signal region. For the right three columns these numbers are calculated in the part of the  $M_{bc} - \Delta E$  signal region with  $LR > 0.75$ . The uncertainties given are statistical only.

### A.3 Background $\Delta t$ shape

To model the background  $\Delta t$  shape the same PDFs as introduced in section 6.7 are used. To determine the shape parameters of the background from  $B\bar{B}$  decays, we fit the  $\Delta t$  distribution of candidates from the generic  $B\bar{B}$  MC, and for the continuum background we fit the distribution of the candidates in  $M_{bc} - \Delta E - LR$  sideband of measured events. The fit results are shown in figure A.3, and the obtained shape parameters are given in appendix B.3.3.

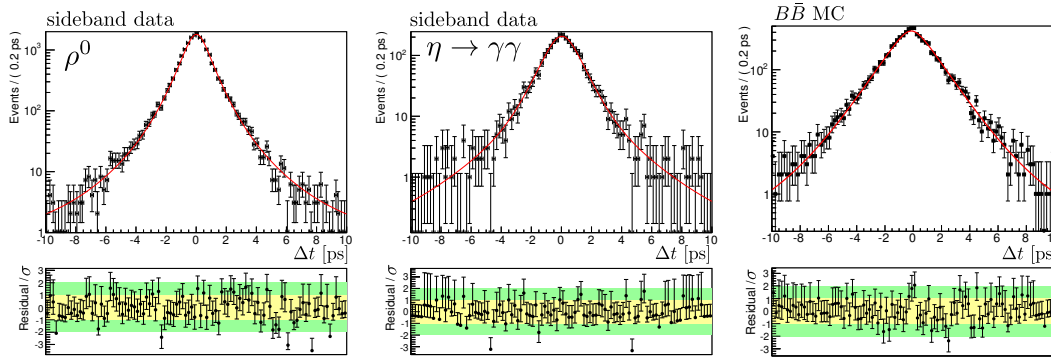


Figure A.3: Fits of background  $\Delta t$  distribution. The left two plots show fits of the candidates in the  $M_{bc} - \Delta E - LR$  sideband of measured data, and the right plot shows fit of background candidates from  $B\bar{B}$  MC sample.

### A.4 Lifetime fit

We use the same signal  $\Delta t$  resolution function as for  $K_S^0 \rightarrow \pi^+\pi^-$  decay mode. Pions from  $K_S^0$  are not used in the vertex reconstruction, so the resolution is independent of the  $K_S^0$  decay mode. We perform the lifetime fit as it also provides a test of the signal/background fraction fit and the background  $\Delta t$  distribution. Fit results are plotted in figure A.4 and obtained lifetimes from both reconstructed modes and simultaneous fit are:

$$\begin{aligned} \rho^0 : \quad \tau_{B^0} &= 1.316 \pm 0.180 \text{ ps} \\ \eta \rightarrow \gamma\gamma : \quad \tau_{B^0} &= 1.786 \pm 0.152 \text{ ps} \\ \text{simul.:} \quad \tau_{B^0} &= 1.510 \pm 0.122 \text{ ps,} \end{aligned}$$

where the uncertainties given are statistical only. The results are to be compared with the world average value of  $\tau_{B^0} = 1.519 \pm 0.007$  ps [24].

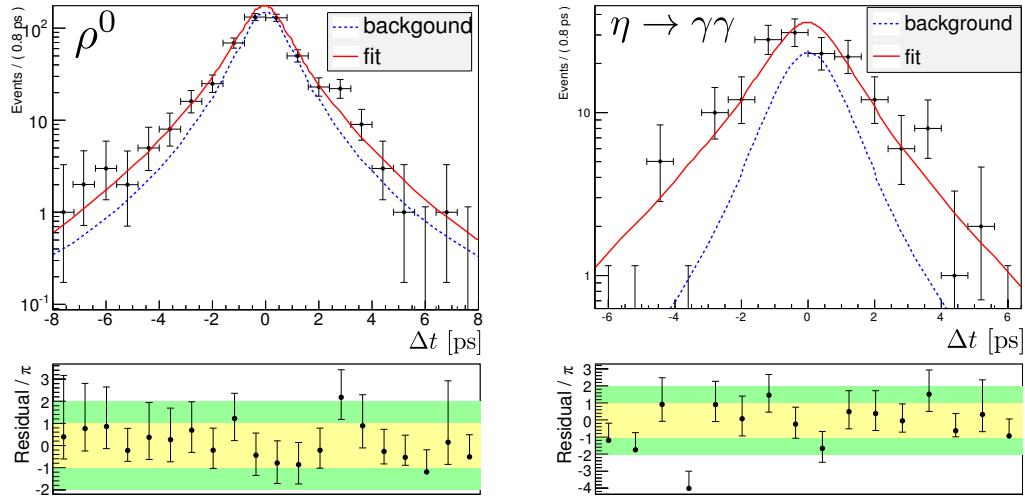


Figure A.4: Lifetime fits of  $B$  candidates reconstructed with  $K_S^0 \rightarrow \pi^0 \pi^0$ . Distributions of the candidates from the  $M_{bc} - \Delta E$  signal region that satisfy  $LR > 0.7$  are shown along with the fitted PDFs.

## A.5 Fit of CPV parameters

We conclude that the prepared procedure is valid and perform the fit of the CPV parameters on the candidates reconstructed with  $K_S^0 \rightarrow \pi^0 \pi^0$ . The obtained results are

$$\mathcal{S}_{\eta' K_S^0(\pi^0 \pi^0)} = +0.576 \pm 0.206,$$

$$\mathcal{A}_{\eta' K_S^0(\pi^0 \pi^0)} = +0.284 \pm 0.180,$$

where the uncertainties given are statistical only. Next we combine  $K_S^0 \rightarrow \pi^+ \pi^-$  and  $K_S^0 \rightarrow \pi^0 \pi^0$  candidates and perform a simultaneous fit. The results are presented in chapter 8.



# B

## Miscellaneous

### B.1 Units

In this work we use units that are commonly used in high energy physics. As a unit of energy electron volt (eV) is used, most commonly with a prefix giga, GeV, which is the energy scale of processes of our interest. To make easier use of  $E^2 = p^2c^2 + m^2c^4$  relation the same unit (GeV) is used to express also mass and momentum. Although formally  $m$  [GeV/ $c^2$ ] and  $p$  [GeV/ $c$ ] a system of natural units, with  $c$  set to 1, is used for the sake of simplicity.

### B.2 Wrong tag fractions and $\Delta t$ resolution function

To determine the fraction of  $B$  candidates with wrongly assigned flavor (wrong tag) and the parameters of the  $\Delta t$  resolution function on the measured events, the following flavor specific decays are studied:  $\bar{B}^0 \rightarrow D^+\pi^-, D^{*+}\pi^-, D^{*+}\rho^-, D^{*+}l^-\bar{\nu}_l$  and  $B^+ \rightarrow D^0\pi^+, D^{*0}\pi^+$ . After the reconstruction, event selection, and signal to background fraction fit of each decay mode, a simultaneous fit to  $\Delta t$  distribution is performed. The PDF used for the fit is given by

$$\mathcal{P}(\Delta t) = (1 - f_{ol}) \left[ f_{sig} \mathcal{P}^{sig} + (1 - f_{sig}) \mathcal{P}^{bkg}(\Delta t) \right] + f_{ol} \mathcal{P}^{ol}(\Delta t), \quad (\text{B.1})$$

where  $f_{sig}$  and  $\mathcal{P}^{bkg}$  depend on the decay mode, and outlier fraction and shape ( $f_{ol}, \mathcal{P}^{ol}$ ) are common to all decay modes. The signal PDF,  $\mathcal{P}^{sig}$ , is obtained as a convolution of the physical part and the resolution function,  $\mathcal{P}^{sig} = \mathcal{P}_{phys}^{sig} \otimes \mathcal{R}^{sig}$ .

For the self tagged  $B^0$  decay modes the  $B^0 - \bar{B}^0$  mixing has to be taken into account, and from the decay rates given in (3.20) and (3.21), we can write

$$\mathcal{P}_{phys}^{sig}(\Delta t)^{OF,SF} = \frac{1}{4\tau_{B^0}} \exp\left(-\frac{|\Delta t|}{\tau_{B^0}}\right) [1 \pm (1 - 2w) \cos \Delta M \Delta t], \quad (\text{B.2})$$

where  $OF$  ( $SF$ ), with  $+$  ( $-$ ) in the bracket, are used for the reconstructed  $B$  candidates decaying into the final state specific for the flavor opposite to (same as) the associated  $B$  meson flavor, determined by flavor tagging algorithm.  $B^0$  candidates are divided into seven bins according to the flavor tagging information quality ( $r$ ), and for each bin a different  $w$  is used. For  $B^\pm$  candidates the  $\Delta t$  PDF is given by the exponential function  $\mathcal{P}_{phys}^{sig} = \frac{1}{2\tau_{B^\pm}} \exp(-|\Delta t|/\tau_{B^\pm})$ .

In the fit of the  $\Delta t$  distribution,  $\Delta t$  resolution function parameters, wrong tag fractions, lifetimes  $\tau_{B^0}$  and  $\tau_{B^\pm}$ , and mixing parameter  $\Delta M$ , are free parameters. The obtained lifetimes and  $\Delta M$  are

$$\tau_{B^\pm} = 1.6261 \pm 0.0038 \text{ ps}, \quad (\text{B.3})$$

$$\tau_{B^0} = 1.5299 \pm 0.0029 \text{ ps}, \quad (\text{B.4})$$

$$\Delta M = 0.5088 \pm 0.0019 \text{ ps}^{-1}, \quad (\text{B.5})$$

where the uncertainties are statistical only. The results are consistent with the world average values [24],  $\tau_{B^\pm} = 1.641 \pm 0.008 \text{ ps}$ ,  $\tau_{B^0} = 1.519 \pm 0.007 \text{ ps}$  and  $\Delta M = 507 \pm 0.004 \text{ ps}^{-1}$ . This validates the resolution function used. To obtain the final values of wrong tag fractions and resolution function parameters, the fit is repeated with  $\tau_{B^\pm}$ ,  $\tau_{B^0}$  and  $\Delta M$  fixed to the world average values, since these are also fixed in the fit to extract the CPV parameters. The obtained wrong tag fractions are summarized in table B.1.

### $\Delta t$ Resolution function

In section 6.6 we only described the resolution function used for vertices reconstructed with multiple tracks. In the case of single track vertex reconstruction a different resolution function is used, because for these vertices  $\chi^2$ , as given in eq. (6.24), cannot be calculated. The detector resolution function used is given by

$$\mathcal{R}_{det}^a(x) = (1 - f_{tail})G(x; 0, s_a^{main}\sigma_z) + f_{tail}G(x, s_a^{tail}\sigma_z) \quad (a = CP, tag), \quad (\text{B.6})$$

where the scale factors  $s_{main}$ ,  $s_{tail}$  and fraction  $f_{tail}$  are shape parameters, and  $\sigma_z$  is obtained from the vertex fit. For the resolution function describing smearing due to non-primary tracks the same function as given in (6.27) is used, but with the following parametrization of effective lifetimes

$$\tau_{p,n} = \tau_{p,n}^{0,sing} + \tau_{p,n}^{1,sing}\sigma_z, \quad (\text{B.7})$$

and the fractions  $f_\delta^{sing}$ ,  $f_n^{sing}$  being constants.

The values of all resolution function parameters obtained from the fit of the control sample are summarized in table B.2

$r$ -bin	SVD1			SVD2		
	$w$	$\sigma^+$ [ $\times 10^{-3}$ ]	$\sigma^-$ [ $\times 10^{-3}$ ]	$w$	$\sigma^+$ [ $\times 10^{-3}$ ]	$\sigma^-$ [ $\times 10^{-3}$ ]
0	0.50			0.5		
1	0.4188	7.23	6.00	0.4188	4.15	3.57
2	0.3298	7.12	6.43	0.3193	3.24	2.80
3	0.2338	7.41	7.69	0.2229	3.72	3.486
4	0.1706	6.88	6.41	0.1631	3.31	4.24
5	0.0997	6.76	8.80	0.1040	3.18	3.69
6	0.0228	4.33	4.58	0.0251	2.17	3.07
$r$ -bin	$\Delta w$			$\Delta w$		
0	0.0			0.0		
1	0.0569	8.92	9.16	-0.0087	3.96	3.92
2	0.0126	9.18	9.14	0.0103	3.54	3.69
3	-0.0147	10.0	9.98	-0.0109	4.12	4.17
4	-0.0005	9.02	8.87	-0.0186	4.16	4.60
5	0.0088	9.30	9.29	0.0016	3.99	3.91
6	0.0046	5.69	5.78	-0.0036	2.43	2.36

Table B.1: Wrong tag fractions obtained from the fit of SVD1 and SVD2 control sample. Beside the mean values also the positive ( $\sigma^+$ ) and negative ( $\sigma^-$ ) uncertainties are shown (statistical + systematic).

## APPENDIX B. MISCELLANEOUS

param.	SVD1			SVD2		
	<i>mean</i>	$\sigma^+$	$\sigma^-$	<i>mean</i>	$\sigma^+$	$\sigma^-$
$s_{CP}^0$	0.7047	0.1714	0.1061	0.8075	0.2793	0.1478
$s_{CP}^1$	0.2121	0.0435	0.0470	0.2326	0.0685	0.0585
$s_{tag}^0$	0.4835	0.2821	0.0731	0.6429	0.3862	0.0721
$s_{tag}^1$	0.2366	0.0374	0.0560	0.2290	0.0265	0.0523
$s_{CP}^{main}$	0.9798	0.2777	0.0363	1.0147	0.4407	0.0389
$s_{CP}^{tail}$	-	-	-	3.6629	3.6167	0.3911
$f_{CP}^{tail}$	0.0	0.0	0.0	0.1110	0.0154	0.0394
$s_{tag}^{main}$	0.9798	0.2777	0.0363	1.0147	0.4407	0.0389
$s_{tag}^{tail}$	-	-	-	3.6629	3.6167	0.3911
$f_{tag}^{tail}$	0.0	0.0	0.0	0.1110	0.0154	0.0394
$\tau_p^0$	-0.0052	0.0154	0.0153	0.0387	0.0055	0.0054
$\tau_p^h$	-0.0296	0.0053	0.0053	-0.0263	0.0017	0.0017
$\tau_p^s$	0.7168	0.0388	0.0386	0.7653	0.0202	0.020
$\tau_p^{sh}$	0.2515	0.0144	0.0143	0.3214	0.0072	0.0071
$\tau_n^0$	0.0452	0.0269	0.0268	0.0829	0.0093	0.0093
$\tau_n^h$	-0.0783	0.0132	0.0130	-0.0301	0.0043	0.0043
$\tau_n^s$	0.5152	0.0638	0.0626	0.5342	0.0310	0.0309
$\tau_n^{sh}$	0.4305	0.0344	0.0331	0.3899	0.0158	0.0156
$f_\delta^0$	0.4664	0.0444	0.0410	0.5600	0.0128	0.0124
$f_\delta^s$	0.2701	0.0704	0.7026	0.1569	0.0278	0.0291
$f_\delta^h$	-0.2204	0.0158	0.0152	-0.2021	0.0047	0.0048
$f_\delta^{sh}$	0.2228	0.0291	0.0300	0.2324	0.0119	0.0115
$f_n$	0.1233	0.0072	0.0072	0.1224	0.0025	0.0025
$\tau_p^{0,sing}$	1.8477	0.0851	0.0806	1.6259	0.0499	0.0488
$\tau_n^{0,sing}$	2.0411	0.2773	0.2431	0.9181	0.0845	0.0781
$f_\delta^{sing}$	0.7817	0.0103	0.0108	0.7737	0.0082	0.0085
$f_p^{sing}$	0.8186	0.0172	0.0184	0.8013	0.0172	0.0176

Table B.2:  $\Delta t$  resolution function parameters obtained from the fit of the control sample. These parameters are used in our analysis. The uncertainties shown include statistical and systematic contributions.

### B.3 Tables of PDF shape parameters

In this appendix we summarize the values of all parameters of the final PDF (eq. 6.39), obtained from the fits done prior to the final fit of the CPV parameters. The uncertainties in all tables are statistical only.

#### B.3.1 Signal $M_{bc} \times \Delta E \times LR$ PDF

param.	$\rho^0$	$\eta \rightarrow \gamma\gamma$	$\eta \rightarrow 3\pi$
$f_{main}$	$0.64721 \pm 0.03152$	$0.61114 \pm 0.04989$	$0.86286 \pm 0.01366$
$f_{out}$	$0.06268 \pm 0.00667$	$0.10160 \pm 0.01992$	-
$\mu_{main}$	$0.00077 \pm 0.00024$	$-0.00017 \pm 0.00054$	$-0.00143 \pm 0.00035$
$\mu_{out}$	$-0.00540 \pm 0.00302$	$-0.02607 \pm 0.00438$	-
$\mu_{tail}$	$0.00186 \pm 0.00211$	$-0.00793 \pm 0.00555$	$-0.01837 \pm 0.00868$
$\mu^{mbc}$	$5.27941 \pm 0.00005$	$5.27942 \pm 0.00008$	$5.27932 \pm 0.00029$
$\sigma_{tail}^L$	$0.02903 \pm 0.00195$	$0.03648 \pm 0.00286$	$0.05698 \pm 0.00527$
$\sigma_{tail}^R$	$0.02563 \pm 0.00171$	$0.03394 \pm 0.00437$	$0.06653 \pm 0.00638$
$\sigma_{main}$	$0.01262 \pm 0.00033$	$0.01718 \pm 0.00072$	$0.01518 \pm 0.00036$
$\sigma_{out}$	$0.08222 \pm 0.00446$	$0.07936 \pm 0.00593$	-
$\sigma^{mbc}$	$0.00250 \pm 0.00005$	$0.00263 \pm 0.00007$	$0.00235 \pm 0.00019$

Table B.3: Parameters of signal  $M_{bc} \times \Delta E \times LR$  PDF for modes reconstructed with  $K_S^0 \rightarrow \pi^+ \pi^-$ , obtained from the fit of signal MC candidates. The used PDF is introduced in section 6.3.1. For  $\eta \rightarrow 3\pi$  mode we do not use the "outliers" component.

param.	$\rho^0$	$\eta \rightarrow \gamma\gamma$
$f_{main}$	$0.54236 \pm 0.06075$	$0.65729 \pm 0.09313$
$\mu_{main}$	$-0.00391 \pm 0.00204$	$-0.01828 \pm 0.00381$
$\mu_{tail}$	$-0.06086 \pm 0.01851$	$-0.10021 \pm 0.03604$
$\mu^{mbc}$	$5.27968 \pm 0.00022$	$5.27977 \pm 0.00048$
$\sigma_{tail}^L$	$0.08786 \pm 0.00803$	$0.09863 \pm 0.01872$
$\sigma_{tail}^R$	$0.07620 \pm 0.00872$	$0.09820 \pm 0.01652$
$\sigma_{main}$	$0.03681 \pm 0.00188$	$0.04818 \pm 0.00338$
$\sigma^{mbc}$	$0.00272 \pm 0.00019$	$0.00310 \pm 0.00025$

Table B.4: Parameters of the signal  $M_{bc} \times \Delta E \times LR$  PDF for modes reconstructed with  $K_S^0 \rightarrow \pi^0 \pi^0$ , obtained from the fit of signal MC candidates. The used PDF is introduced in section 6.3.1. For these modes the "outliers" component is not used.

**B.3.2 Signal/Background fraction fit**

param.	$\rho^0$	$\eta \rightarrow \gamma\gamma$	$\eta \rightarrow 3\pi$
$a$	$-1.51669 \pm 0.03687$	$-1.65640 \pm 0.09984$	$-1.51791 \pm 0.23528$
$b$	$0.64413 \pm 0.08372$	$1.13200 \pm 0.28642$	$0.37591 \pm 0.60075$
$c$	$-20.7794 \pm 0.43792$	$-24.4881 \pm 1.54145$	$-26.1784 \pm 3.78057$
$\mu_{main}$	$0.00191 \pm 0.00091$	$-0.00084 \pm 0.00164$	$-0.00494 \pm 0.00153$
$\sigma_{main}$	$0.01573 \pm 0.00087$	$0.01998 \pm 0.00136$	$0.01660 \pm 0.00118$
$f_{sig}^0$	$0.00859 \pm 0.00063$	$0.05325 \pm 0.00460$	$0.08343 \pm 0.01331$
$f_{sig}^1$	$0.00984 \pm 0.00087$	$0.05623 \pm 0.00616$	$0.08952 \pm 0.01667$
$f_{sig}^2$	$0.01036 \pm 0.00091$	$0.06287 \pm 0.00636$	$0.07232 \pm 0.01593$
$f_{sig}^3$	$0.01376 \pm 0.00129$	$0.09022 \pm 0.00982$	$0.12927 \pm 0.02835$
$f_{sig}^4$	$0.01118 \pm 0.00122$	$0.05594 \pm 0.00830$	$0.14034 \pm 0.02962$
$f_{sig}^5$	$0.01702 \pm 0.00165$	$0.06348 \pm 0.00949$	$0.13533 \pm 0.02994$
$f_{sig}^6$	$0.07628 \pm 0.00507$	$0.29446 \pm 0.02590$	$0.38478 \pm 0.06040$

Table B.5: Parameters obtained from the signal/background fraction fit of measured data, for modes reconstructed with  $K_S^0 \rightarrow \pi^+ \pi^-$ . The fit procedure is described in section 6.3.4.

param.	$\rho^0$	$\eta \rightarrow \gamma\gamma$
$a$	$-1.88828 \pm 0.08404$	$-2.37874 \pm 0.11247$
$b$	$0.76381 \pm 0.15177$	$1.81840 \pm 0.34942$
$c$	$-21.2708 \pm 0.79382$	$-21.3613 \pm 2.10688$
$f_{sig}^0$	$0.00186 \pm 0.00102$	$0.00923 \pm 0.00304$
$f_{sig}^1$	$0.00409 \pm 0.00142$	$0.01103 \pm 0.00443$
$f_{sig}^2$	$0.00421 \pm 0.00157$	$0.02463 \pm 0.00658$
$f_{sig}^3$	$0.0052 \pm 0.00223$	$0.04033 \pm 0.01102$
$f_{sig}^4$	$0.00461 \pm 0.00229$	$0.02620 \pm 0.00929$
$f_{sig}^5$	$0.00133 \pm 0.00384$	$0.04648 \pm 0.01458$
$f_{sig}^6$	$0.05165 \pm 0.00105$	$0.16148 \pm 0.04087$

Table B.6: Parameters obtained from the signal/background fraction fit of measured data, for modes reconstructed with  $K_S^0 \rightarrow \pi^0 \pi^0$ . The fit procedure is described in section 6.3.4.

param.	$\rho^0$	$\eta \rightarrow \gamma\gamma$	$\eta \rightarrow 3\pi$
$f_{B\bar{B}}^0$	0.01101	0.00173	0.00233
$f_{B\bar{B}}^1$	0.01431	0.00137	0.00310
$f_{B\bar{B}}^2$	0.01612	0.00240	0.00240
$f_{B\bar{B}}^3$	0.01678	0.00325	0.00449
$f_{B\bar{B}}^4$	0.01417	0.00237	0.00358
$f_{B\bar{B}}^5$	0.01819	0.00225	0.00221
$f_{B\bar{B}}^6$	0.05032	0.00581	0.00311

Table B.7: Fractions of background candidates from generic  $B\bar{B}$  decays, for all  $r$  bins, for modes reconstructed with  $K_S^0 \rightarrow \pi^+\pi^-$ . The  $M_{bc} - \Delta E$  region used is given in (6.21).

param.	$\rho^0$	$\eta \rightarrow \gamma\gamma$
$f_{B\bar{B}}^0$	0.01458	0.00227
$f_{B\bar{B}}^1$	0.01962	0.00368
$f_{B\bar{B}}^2$	0.02591	0.00398
$f_{B\bar{B}}^3$	0.02712	0.00309
$f_{B\bar{B}}^4$	0.02497	0.00487
$f_{B\bar{B}}^5$	0.03020	0.00719
$f_{B\bar{B}}^6$	0.07251	0.01408

Table B.8: Fractions of background candidates from generic  $B\bar{B}$  decays, for all  $r$  bins, for modes reconstructed with  $K_S^0 \rightarrow \pi^0\pi^0$ . The  $M_{bc} - \Delta E$  region used is given in (6.21).

### B.3.3 Background $\Delta t$ shape parameters

param.	$\rho^0$	$\eta \rightarrow \gamma\gamma$	$\eta \rightarrow 3\pi$
$\sigma_{main}$	$1.14058 \pm 0.01198$	$1.13537 \pm 0.03964$	$1.17198 \pm 0.09678$
$\sigma_{out}$	$27.6202 \pm 1.26978$	$30.3102 \pm 4.03072$	$10.6445 \pm 7.38035$
$\sigma_{tail}$	$3.84347 \pm 0.09462$	$3.84401 \pm 0.31426$	$5.97836 \pm 1.26626$
$f_\delta$	$0.46549 \pm 0.02542$	$0.47245 \pm 0.09446$	$0.39168 \pm 0.12857$
$f_{out}$	$0.01236 \pm 0.00072$	$0.01259 \pm 0.00242$	$0.00953 \pm 0.02552$
$f_{tail}$	$0.14653 \pm 0.00777$	$0.15981 \pm 0.02768$	$0.08809 \pm 0.03885$
$\mu_\delta$	$-0.01317 \pm 0.01052$	$-0.01840 \pm 0.04991$	$-0.06207 \pm 0.08989$
$\mu_\tau$	$0.04602 \pm 0.01356$	$0.06805 \pm 0.06132$	$0.07247 \pm 0.09904$
$\tau_{bkg}$	$0.57528 \pm 0.02216$	$0.63783 \pm 0.09045$	$0.78553 \pm 0.13529$

Table B.9: Parameters of the background  $\Delta t$  PDF, obtained from the fit of measured data sideband, for modes reconstructed with  $K_S^0 \rightarrow \pi^+\pi^-$ . The fit procedure is described in section 6.7.

param.	$\rho^0$	$\eta \rightarrow \gamma\gamma$
$\sigma_{main}$	$1.04506 \pm 0.02290$	$1.13098 \pm 0.04738$
$\sigma_{out}$	$17.2121 \pm 1.37908$	$27.5123 \pm 6.37009$
$\sigma_{tail}$	$3.14152 \pm 0.12165$	$3.79134 \pm 0.35678$
$f_\delta$	$0.43964 \pm 0.06147$	$0.37833 \pm 0.17060$
$f_{out}$	$0.01353 \pm 0.00165$	$0.00887 \pm 0.00269$
$f_{tail}$	$0.19884 \pm 0.01773$	$0.13620 \pm 0.02761$
$\mu_\delta$	$0.03108 \pm 0.022648$	$0.04465 \pm 0.09347$
$\mu_\tau$	$-0.00643 \pm 0.024181$	$0.02312 \pm 0.07239$
$\tau_{bkg}$	$0.47569 \pm 0.04299$	$0.50141 \pm 0.10140$

Table B.10: Parameters of the background  $\Delta t$  PDF, obtained from the fit of measured data side-band, for modes reconstructed with  $K_S^0 \rightarrow \pi^0\pi^0$ . The fit procedure and used PDF are described in section 6.7.

param.	$K_S^0 \rightarrow \pi^+\pi^-$	$K_S^0 \rightarrow \pi^0\pi^0$
$\sigma_{main}$	$5.75214 \pm 0.69209$	$8.19295 \pm 1.28161$
$\sigma_{out}$	$0.98858 \pm 0.05385$	$0.94660 \pm 0.01376$
$\sigma_{tail}$	$38.6135 \pm 5.94849$	$41.2452 \pm 10.2304$
$f_{out}$	$0.93586 \pm 0.01567$	$0.91483 \pm 0.02779$
$f_{tail}$	$0.05668 \pm 0.01659$	$0.06993 \pm 0.02779$
$\mu_l$	$-0.17100 \pm 0.01511$	$-0.13662 \pm 0.01892$
$\tau_{bkg}$	$1.44578 \pm 0.02150$	$1.24238 \pm 0.03181$

Table B.11: Parameters of the  $\Delta t$  PDF of background candidates from generic  $B\bar{B}$  decays, obtained from the fit of  $B\bar{B}$  MC sample. The fit procedure and used PDF are described in section 6.7.



## SLOVENSKI POVZETEK

### Meritev kršitve simetrije CP v razpadih

$$B^0 \rightarrow \eta' K_S^0$$

#### C.1 Uvod

Simetrije imajo pomembno vlogo tako v vsakdanjem življenju kot v sodobni znanosti. Ko se sprašujemo o simetrijah fizikalnih zakonov, nas zanimajo transformacije fizikalnih sistemov, ki ne spremenijo dinamike sistema. Če taka transformacija obstaja, pravimo, da je sistem, oziroma fizikalni zakon, ki opisuje njegovo dinamiko, invarianten ali simetričen glede na izbrano transformacijo. Tema pričujočega dela, simetrija CP, je invariantnost na produkt dveh transformacij: konjugacijo naboja C, ki pretvori delec v antidelec ( $Q \rightarrow \bar{Q}$ ) in parnost P, ki prezrcali prostorske koordinate ( $\vec{x} \rightarrow -\vec{x}$ ). Tako se na primer levoročni elektron  $e_L^-$  pri transformaciji CP preslika v desnoročni pozitron  $e_R^+$ . Večina pojavov v naravi je C in P simetričnih (torej tudi CP). Pravzaprav so taki vsi pojavi, ki so povezani z elektromagnetno, močno jedrsko in gravitacijsko silo. Na drugi strani šibka jedrska sila očitno in močno krši C in P simetrijo, saj sklaplja le levoročne fermione in desnoročne antifermione. Kljub temu obstaja precej procesov preko šibke interakcije, ki so simetrični na produkt obeh transformacij, CP. Simetrija CP je do sredine prejšnjega stoletja veljala za eksaktno simetrijo narave, simetrijo med materijo in antimaterijo. Da to ne drži povsem, se je eksperimentalno prvič pokazalo pri meritvah razpadov nevtralnih kaonov leta 1964 [3], do preboja v teoretičnem opisu opažene kršitve simetrije CP pa je prišlo slabih 10 let pozneje. Leta 1973 sta M. Kobayashi in T. Maskawa pokazala kako kršitev CP vstopa v takrat nastajajočo teorijo osnovnih delcev, Standardni Model (SM) [4]. Opazila sta, da je kršitev simetrije CP v SM naravno prisotna, če le obsta-

jajo vsaj tri družine kvarkov (leta 1973 so bili znani le kvarki  $u, d, s$ ). V tem primeru kvarkovska mešalna matrika, t.i. matrika Cabibbo-Kobayashi-Maskawa, krajše matrika CKM, ki podaja relativne jakosti sklopitev nabitih šibkih bozonov s kvarki različnih okusov, vsebuje kompleksno fazo, ki je vir kršitve simetrije CP v SM. Kmalu zatem sta bila odkrita kvarka  $c$  (1974) in  $b$  (1977), in končno leta 1995 še kvark  $t$ .

Da bi preverili konsistentnost t.i. Kobayashi-Maskawa (KM) mehanizma kršitve simetrije CP, z eno kompleksno fazo v matriki CKM, so nujne meritve kršitve simetrije CP v sistemu mezonov  $B$  (mezonov, ki vsebujejo kvark  $b$ ), v katerem mehanizem KM napove relativno velike kršitve simetrije CP. V ta namen sta bili v devetdesetih letih prejšnjega stoletja zgrajeni dve tovarni mezonov  $B$ , KEKB in PEP-II, z eksperimentoma Belle [5] in BaBar [6]. Leta 2001 sta oba eksperimenta potrdila kršitev simetrije CP v razpadih nevtralnih mezonov  $B$  v  $J/\psi K_S^0$  [7,8]. To je bila prva opažena kršitev simetrije CP izven sistema kaonov. V naslednjem desetletju so pri Belle in BaBar izmerili kršitev CP še v številnih drugih razpadih mezonov  $B$ , v vseh v skladu z napovedmi SM, in potrdili kompleksno fazo matrike CKM kot glavni vir kršitve simetrije CP. Eksperimentalna potrditev napovedi Kobayashija in Maskawe jima je prinesla Nobelovo nagrado za fiziko v letu 2008.

Kljub vsem potrditvam mehanizma KM, je na mestu vprašanje, ali je kompleksna faza matrike CKM edini vir kršitve simetrije CP. Misel, da temu ni tako, spodbujata vsaj dva argumenta. Prvič, prisotnost novih kompleksnih faz, ki kršijo simetrijo CP, se zdi neizogibna v večini modelov razširitve SM (t.i. nove fizike). Drugič, kršitev simetrije CP je nujni pogoj za razlago dominance materije nad antimaterijo v opazljivem vesolju, toda ta kršitev je v SM mnogo premajhna, da bi pojasnila opaženo asimetrijo. Prisotnost novih virov kršitve simetrije CP je tako nujna tudi s kozmološkega vidika.

V sistemu mezonov  $B$  so na morebitno prisotnost novih faz, ki kršijo simetrijo CP, posebej občutljivi razpadi pri katerih se kvark  $b$  pretvori v kvark  $s$  in še dva kvarka ( $b \rightarrow s\bar{q}q$ ). Taki razpadi v SM potekajo le preko diagramov z zankami, v katerih lahko prisotnost težkih, še neodkritih delcev, spremeni vrednosti nekaterih opazljivih količin. V primeru razpadov  $b \rightarrow s\bar{q}q$  je ta opazljiva količina časovno odvisna kršitev simetrije CP. Meritev njene vrednosti in primerjava z napovedjo SM torej ponuja možnost detekcije nove fizike.

V pričujočem delu predstavimo meritev časovno odvisne kršitve simetrije CP v razpadih  $B^0 \rightarrow \eta' K_S^0$ , ki potekajo preko omenjenega procesa  $b \rightarrow s\bar{q}q$ . Meritev je bila opravljena na vzorcu 772 milijonov razpadov parov  $B\bar{B}$ , zbranih z detektorjem Belle v času njegovega delovanja (1999-2010). V delu najprej predstavimo izvor kršitve simetrije CP v SM (poglavje C.2), nato pa v njegovem okviru izračunamo napoved vrednosti parametrov kršitve CP v razpadu  $B^0 \rightarrow \eta' K_S^0$  in jih primerjamo z rezultati dosedanjih meritev (poglavje C.3). V poglavju C.4 predstavimo detektor Belle. Sledi opis postopka meritve (poglavje C.5) in končno rezultat meritve (poglavje C.6). Zaključimo s pogledom v prihodnost, v poglavju C.7.

## C.2 Kršitev simetrije CP v Standardnem Modelu

Kršitev simetrije CP vstopa v Standardni Model preko kompleksnih faz v Yukawinih sklopitvah Higgsovega polja s kvarki. Po spontanem zlomu simetrije najdemo le te v masnih matrikah kvarkov, ki so v splošnem ne-diagonalne. Izkaže se, da njihova diagonalizacija, in s tem prehod iz baze lastnih interakcijskih stanj (t.j. stanj, ki se sklapljajo z umeritvenimi bozoni) v bazo lastnih masnih stanj, vpliva le na obliko členov Lagrangiana, ki določajo sklopitev kvarkov z nabitimi šibkimi bozoni ( $W^\pm$ ). Z  $W^\pm$  se sklapljajo le levoročni kvarki, ki se nahajajo v  $SU(2)_L$  dubletih. SM vsebuje tri družine in s tem tri kvarkovske dublete:  $(u\ d)_L, (c\ s)_L, (t\ b)_L$ . Prej omenjena menjava baze povzroči, da se  $W^\pm$  sklapljajo s kvarkovskimi stanji, ki jih iz lastnih masnih stanj kvarkov dobimo tako, da slednja (zadostuje izbrati le spodnje kvarke iz vsakega  $SU(2)_L$  dubleta, t.j. kvarke z nabojem  $-1/3 e_0$ ) pomnožimo z unitarno<sup>1</sup>  $3 \times 3$  matriko CKM (označimo jo z  $\mathbf{V}$ )

$$\begin{pmatrix} d' \\ s' \\ b' \end{pmatrix} = \mathbf{V} \begin{pmatrix} d \\ s \\ b \end{pmatrix} = \begin{pmatrix} V_{ud} & V_{us} & V_{ub} \\ V_{cd} & V_{cs} & V_{cb} \\ V_{td} & V_{ts} & V_{tb} \end{pmatrix} \begin{pmatrix} d \\ s \\ b \end{pmatrix}. \quad (\text{C.1})$$

Ob upoštevanju unitarnosti ugotovimo, da ima matrika  $\mathbf{V}$  9 prostih parametrov. Med temi so 3 koti in 6 kompleksnih faz, od katerih pa jih lahko 5 odstranimo z redefinicijo relativnih faz kvarkovskih polj. Tako končamo z eno samo kompleksno fazo, t.i. fazo Kobayashi-Maskawa, ki krši simetrijo CP Lagrangiana Standardnega modela. Poudariti velja, da so elementi matrike  $\mathbf{V}$  prosti parametri Standardnega Modela in jih moramo določiti z eksperimentom.

### C.2.1 Wolfensteinova parametrizacija

Parametrizacija matrike CKM, s štirimi prostimi parametri, ni enolično določena. S fenomenološkega vidika je posebej priročna t.i. Wolfensteinova parametrizacija [23], ki temelji na eksperimentalno opaženi hierarhiji  $|V_{ub}|^2 \ll |V_{cb}| \ll |V_{us}|^2 \ll 1$ . Definiramo  $\lambda \equiv |V_{us}| \simeq 0.22$  in zapišemo matriko CKM v obliki

$$\mathbf{V} = \begin{pmatrix} 1 - \lambda^2/2 & \lambda & \lambda^3 A(\rho - i\eta) \\ -\lambda & 1 - \lambda^2/2 & \lambda^2 A \\ \lambda^3 A(1 - \rho - i\eta) & -\lambda^2 A & 1 \end{pmatrix}, \quad (\text{C.2})$$

kjer so  $\lambda, A, \rho$  in  $\eta$  prosti parametri, določeni z eksperimentom, in ne ničelni  $\eta$  vpelje kršitev simetrije CP.

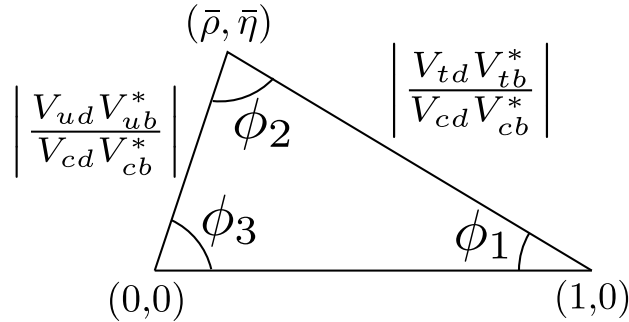
<sup>1</sup>Matrika CKM je produkt dveh unitarnih transformacijskih matrik (prehod iz int. v masno bazo) in je tako tudi sama unitarna.

### C.2.2 Unitarni trikotnik

Ker je matrika CKM unitarna, morajo njeni elementi zadoščati zvezam  $\sum_k V_{ki} V_{kj}^* = \delta_{ij}$ . Če produkte  $V_{ki} V_{kj}^*$  predstavimo kot vektorje v kompleksni ravnini, tri izmed omenjenih vsot (z  $i \neq j$ ) tvorijo t.i. unitarni trikotnik. Najzanimivejši trikotnik, v katerem so dolžine vseh treh stranic velikostnega reda  $\lambda^3$  (in posledično vsi koti veliki), daje zveza  $V_{ud} V_{ub}^* + V_{cd} V_{cb}^* + V_{td} V_{tb}^* = 0$ . Če to še delimo z  $V_{cd} V_{cb}^*$ , dobimo trikotnik z oglišči  $(0,0)$ ,  $(1,0)$  in  $(\bar{\rho}, \bar{\eta})$ , kjer je  $\bar{\rho} = \rho(1 - \lambda^2/2)$  in  $\bar{\eta} = \eta(1 - \lambda^2/2)$ . Trikotnik je skiciran na sliki C.1. Z elementi matrike CKM se koti unitarnega trikotnika zapišejo kot

$$\phi_1 = \arg \left[ -\frac{V_{cd} V_{cb}^*}{V_{td} V_{tb}^*} \right], \quad \phi_2 = \arg \left[ -\frac{V_{td} V_{tb}^*}{V_{ud} V_{ub}^*} \right], \quad \phi_3 = \arg \left[ -\frac{V_{ud} V_{ub}^*}{V_{cd} V_{cb}^*} \right]. \quad (C.3)$$

Parametri (stranice in koti) unitarnega trikotnika so v veliki meri določeni z meritvami razpadnih širin in asimetrij CP v sistemu mezonov  $B$ . Te meritve predstavljajo test konsistentnosti SM, nekateri razpadni kanali pa so, kot že omenjeno v uvodu, občutljivi na morebitne prispevke nove fizike.

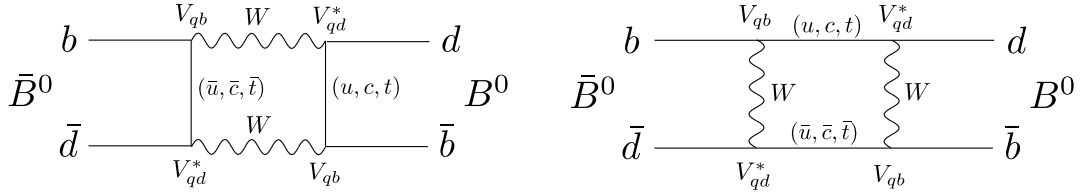


Slika C.1: Skica unitarnega trikotnika, z definicijami kotov in stranic.

### C.3 Kršitev simetrije CP v razpadu $B^0 \rightarrow \eta' K_S^0$

Nevtralni mezon  $B^0$  je vezano stanje kvarkov  $d$  in  $\bar{b}$  (njegov antidelec  $\bar{B}^0$  pa kvarkov  $\bar{d}$  in  $b$ ). Ker stanji  $B^0$  in  $\bar{B}^0$ , z dobro definirano kvarkovsko vsebino (lastni stanji okusa), nista masni lastni stanji (s katerimi opisujemo razvoj stanja v času), pride v časovnem razvoju mezona  $B^0$  ( $\bar{B}^0$ ) do t.i. mešanja, pri katerem ta pridobi komponento mezona nasprotnega okusa,  $\bar{B}^0$  ( $B^0$ ). V SM mešanje poteka preko procesa prikazanega na sliki C.2.

Fenomenološko proces mešanja opišemo s Schrödingerjevo enačbo z efektivnim Hamiltonianom. S krajšim računom lahko izpeljemo časovno odvisnost verjetnosti



Slika C.2: Feynmanova diagrama preko katerih poteka proces mešanja nevtralnih mezonov B.

za razpad stanja, ki je bilo ob času  $t = 0$  čisto  $B^0$  ( $\bar{B}^0$ ) stanje, označimo ga z  $B^0(t)$  ( $\bar{B}^0(t)$ ), v končno stanje  $f$ . Dobimo [30]

$$\begin{aligned}\Gamma(B^0(t) \rightarrow f) &\propto e^{-t/\tau_{B^0}} [1 - \mathcal{A}_f \cos \Delta Mt - \mathcal{S}_f \sin \Delta Mt], \\ \Gamma(\bar{B}^0(t) \rightarrow f) &\propto e^{-t/\tau_{B^0}} [1 + \mathcal{A}_f \cos \Delta Mt + \mathcal{S}_f \sin \Delta Mt],\end{aligned}\quad (\text{C.4})$$

kjer je  $\tau_{B^0}$  razpadni čas mezona  $B^0$ ,  $\Delta M$  razlika mas lastnih masnih stanj mezona  $B^0$ , in

$$\mathcal{A}_f = \frac{|\lambda_f|^2 - 1}{|\lambda_f|^2 + 1}, \quad \mathcal{S}_f = \frac{2\text{Im}\lambda_f}{1 + |\lambda_f|^2}, \quad \text{z} \quad \lambda_f = \frac{q}{p} \frac{\bar{A}_f}{A_f}.\quad (\text{C.5})$$

Tu z  $A_f$  ( $\bar{A}_f$ ) označimo verjetnostno amplitudo za razpad mezona  $B^0$  ( $\bar{B}^0$ ) v stanje  $f$ ,  $q/p$  pa določa izražavo masnih stanj ( $B_L, B_H$ ) z lastnimi stanji okusa,  $|B_L\rangle = p|B^0\rangle + q|\bar{B}^0\rangle$  in  $|B_H\rangle = p|B^0\rangle - q|\bar{B}^0\rangle$ , in ga lahko zapišemo kot [30]

$$\frac{q}{p} \simeq \frac{V_{tb}^* V_{td}}{V_{tb} V_{td}^*}.\quad (\text{C.6})$$

Z uporabo enačb (C.4) izračunamo časovno odvisno asimetrijo med razpadi mezonov  $B^0$  in  $\bar{B}^0$ :

$$a_f(t) \equiv \frac{\Gamma(B^0(t) \rightarrow f) - \Gamma(\bar{B}^0(t) \rightarrow f)}{\Gamma(B^0(t) \rightarrow f) + \Gamma(\bar{B}^0(t) \rightarrow f)} = \mathcal{A}_f \cos \Delta Mt + \mathcal{S}_f \sin \Delta Mt,\quad (\text{C.7})$$

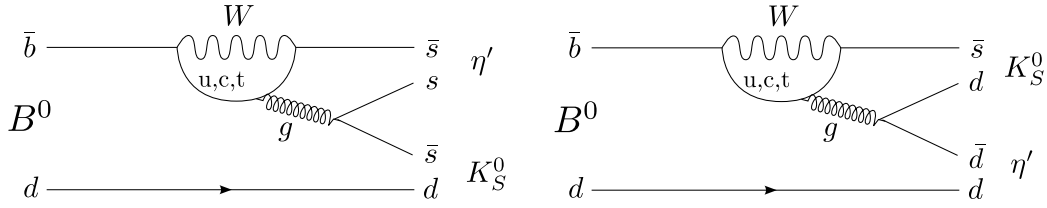
parametra  $\mathcal{A}_f$  in  $\mathcal{S}_f$  pa zato imenujemo tudi parametra kršitve CP. Njuni vrednosti sta odvisni od končnega stanja  $f$  in ju po (C.5) lahko izračunamo v okviru SM.

V SM razpad  $B^0 \rightarrow \eta' K_S^0$  poteka preko t.i. pingvinskih diagramov, prikaznih na sliki C.3. K razpadu prispeva tudi drevesni diagram z  $b \rightarrow u$  prehodom, ki pa je barvno in CKM potlačen (z  $\lambda^2$ ), in je zato njegov prispevek majhen ( $\mathcal{O}(10^{-2})$ ). Iz diagramov C.3 lahko v okviru SM izračunamo amplitudi  $A_{\eta' K_S^0}$  in  $\bar{A}_{\eta' K_S^0}$ , in skupaj s (C.5) dobimo [30]

$$\lambda_{\eta' K_S^0} = \frac{q}{p} \frac{\bar{A}_{\eta' K_S^0}}{A_{\eta' K_S^0}} \simeq -\frac{V_{tb}^* V_{td}}{V_{tb} V_{td}^*} \frac{V_{cb}^* V_{cs}}{V_{cb} V_{cs}^*} \frac{V_{cs}^* V_{cd}}{V_{cs} V_{cd}^*} = -e^{-2i\phi_1},\quad (\text{C.8})$$

kjer je  $\phi_1$  eden izmed kotov unitarnega trikotnika. Iz (C.5) nadalje sledi

$$\mathcal{A}_{\eta' K_S^0} \simeq 0, \quad \mathcal{S}_{\eta' K_S^0} \simeq \sin 2\phi_1,\quad (\text{C.9})$$



Slika C.3: Feynmanova diagrama razpada  $B^0 \rightarrow \eta' K_S^0$ . Diagram za razpad mezona  $\bar{B}^0$  dobimo z konjugacijo  $q \rightarrow \bar{q}$ .

rezultat, ki je natančen do  $\mathcal{O}(10^{-2})$ . Za oceno možnih odstopanj parametrov  $\mathcal{A}_{\eta' K_S^0}$  in  $\mathcal{S}_{\eta' K_S^0}$  od vrednosti (C.9), v okviru SM, je bilo uporabljenih več teoretičnih pristopov. Na primer, QCD faktorizacija napove  $\mathcal{S}_{\eta' K_S^0} - \sin 2\phi_1$  v območju  $(-0.03, 0.03)$  [15–17], medtem ko uporaba okusnih relacij  $SU(3)$  to razliko omejuje na  $(-0.05, 0.09)$  [18].

### C.3.1 Iskanje Nove fizike

Kot že rečeno v prejšnjem poglavju, razpad  $B^0 \rightarrow \eta' K_S^0$  v SM poteka skoraj izključno preko pingvinskih diagramov. V zankah teh diagramov lahko prispevajo težki, še neodkriti delci, in povzročijo odmik vrednosti parametrov kršitve CP od pričakovanih vrednosti v okviru SM [13]. Meritev časovno odvisne asimetrije  $a_{\eta' K_S^0}$  je dodatno zanimiva, ker je vrednost  $\sin 2\phi_1$  zelo natančno izmerjena v veliko pogostejših razpadih  $B^0 \rightarrow J/\psi K_S^0$ . Ta razpad je dominiran s procesom drevesnega reda in kot tak razmeroma neobčutljiv na prispevke nove fizike. Razlika  $\mathcal{S}_{\eta' K_S^0} - \sin 2\phi_1$  je tako ena izmed “zlatih opazljivk” za odkritje novih izvorov kršitve simetrije CP.

### C.3.2 Dosedanje meritve

Zadnje meritve časovno odvisne kršitve simetrije CP v razpadih  $B^0 \rightarrow \eta' K_S^0$  sta opravili kolaboraciji Belle (2007 [35]) in BaBar (2009 [36]). Pri Belle so za meritev uporabil vzorec z  $535 \times 10^6$ , pri BaBar pa z  $467 \times 10^6$  razpadi parov mezonov  $B\bar{B}$ . Rezultati teh meritev so povzeti v tabeli C.1, kjer so prikazani tudi rezultati skupne meritve v razpadih  $B^0 \rightarrow \eta' K_S^0$  in  $B^0 \rightarrow \eta' K_L^0$ . V razpadu  $B^0 \rightarrow \eta' K_L^0$  namreč pričakujemo enake vrednosti parametrov kršitve CP kot v  $B^0 \rightarrow \eta' K_S^0$ . S skupno meritvijo zmanjšamo statistično negotovost izmerjenih vrednosti parametrov kršitve CP, rezultat pa navajamo kot rezultat meritve v razpadu  $B^0 \rightarrow \eta' K^0$ . Iz tabele vidimo, da vrednost parametra  $\mathcal{S}_{\eta' K_S^0}$  odstopa od vrednosti  $\sin 2\phi_1$  za približno eno standardno deviacijo, negotovost posamezne meritve pa je okoli 0.10.

	$\mathcal{S}$	$\mathcal{A}$
$B \rightarrow \eta' K_S^0$		
Belle	$0.67 \pm 0.11 \pm 0.04$	$-0.03 \pm 0.07 \pm 0.05$
BaBar	$0.53 \pm 0.08 \pm 0.02$	$+0.11 \pm 0.06 \pm 0.02$
$B \rightarrow \eta' K^0$		
Belle	$0.64 \pm 0.10 \pm 0.04$	$-0.01 \pm 0.07 \pm 0.05$
BaBar	$0.57 \pm 0.08 \pm 0.02$	$+0.08 \pm 0.06 \pm 0.02$
Povprečje	$0.60 \pm 0.07$	$+0.05 \pm 0.05$
$B \rightarrow J/\psi K_S^0$	$0.68 \pm 0.02$	$-0.01 \pm 0.02$

Tabela C.1: Eksperimentalne vrednosti parametrov kršitve CP v razpadih  $B^0 \rightarrow \eta' K_S^0$ , iz zadnjih meritev. Pri vseh vrednostih je najprej navedena statistična, nato pa še sistematska negotovost. Prikazane so tudi vrednosti iz skupne meritve v razpadih  $B^0 \rightarrow \eta' K_S^0$  in  $B^0 \rightarrow \eta' K_L^0$ , in pa svetovno povprečje vrednosti  $\sin 2\phi_1$  [29, 35, 36].

## C.4 Detektor Belle

Podatki iz katerih v delu izluščimo vrednosti parametrov kršitve CP v razpadu  $B^0 \rightarrow \eta' K_S^0$  so bili pridobljeni z detektorjem Belle, ki je deloval na trkalniku KEKB v Tsukubi na Japonskem. KEKB in Belle sta bila zasnovana posebej za meritve kršitve simetrije CP v sistemu mezonov  $B$ . Trkalnik KEKB trka elektrone in pozitrone, pri čemer je energija žarka elektronov 8 GeV, žarka pozitronov pa 3.5 GeV. Trkalnik se nahaja v tunelu 11 m pod zemljo in ima obseg približno 3 km. Žarka elektronov in pozitronov se sekata v t.i. interakcijski točki, kjer pri trkih nastajajo mezoni  $B$  v procesu:

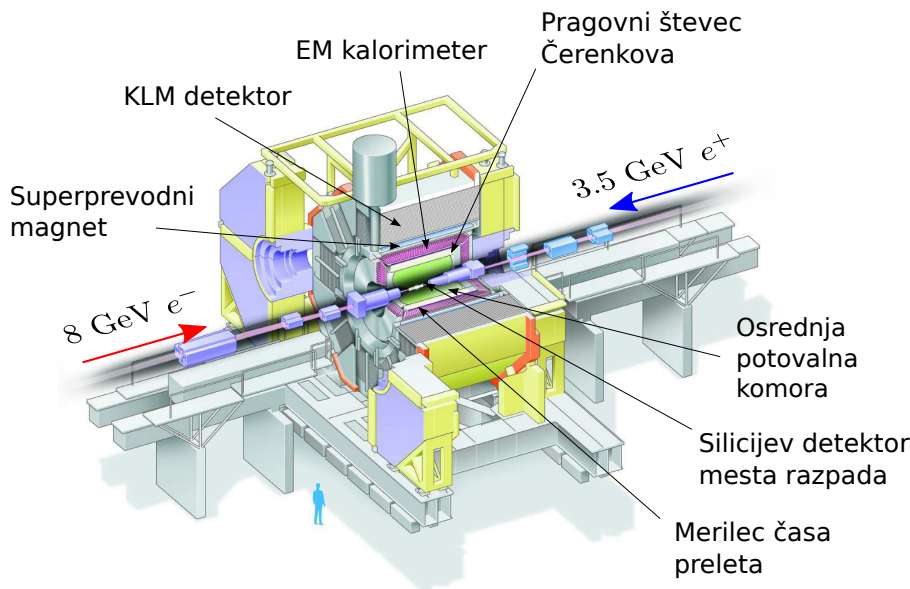
$$e^- \xrightarrow{8 \text{ GeV}} \xleftarrow{3.5 \text{ GeV}} e^+ \implies Y(4S) \implies B \bar{B}. \quad (\text{C.10})$$

Resonanca  $Y(4S)$  je vezano stanje kvarkov  $b$  in  $\bar{b}$  in v praktično 100% razpade v par  $B\bar{B}$ , ki je v polovici primerov par  $B^+ B^-$  in v drugi polovici par  $B^0 \bar{B}^0$ . Energija žarkov je naravnana tako, da ustreza masi resonance  $Y(4S)$ , s čimer dosežemo znaten presek za nastanek para  $B\bar{B}$ . Z večjo pogostostjo kot pari mezonov  $B\bar{B}$  nastanejo v trkih pari lažjih kvarkov, v procesu  $e^+ e^- \rightarrow q\bar{q}$ , kjer  $q = u, d, s, c$ . Ti dogodki v študijah lastnosti mezonov  $B$  predstavljajo dogodke ozadja. V primeru nastanka resonance  $Y(4S)$  in posledično para  $B\bar{B}$ , slednji v težiščem sistemu resonance  $Y(4S)$  praktično miruje. V laboratorijskem sistemu se nastala mezona  $B$  torej gibata v smeri žarka z višjo energijo in z znano gibalno količino, določeno z energijama žarkov. To nam omogoča posredno meritev časa iz razdalje, ki jo mezona  $B$  preletita v laboratorijskem sistemu. Kot bomo videli kasneje je to ključnega pomena pri meritvah časovno odvisnih asimetrij.

Detektor Belle, nameščen v cilindrično simetrični konfiguraciji okrog interakcijske točke, je v osnovi magnetni spektrometer. Z njim lahko z visoko učinkovitostjo detektiramo in identificiramo dolgožive delce, ki nastajajo pri trkih elektronov in

pozitronov (to so  $e^\pm, \mu^\pm, \pi^\pm, K^\pm, p^\pm, \gamma$  in  $K_L^0$ ). Običajno so ti delci razpadni produkti težjih delcev, kot so na primer mezoni  $B$  in  $D$ , ali drugih kratkoživih hadronov, ki razpadejo praktično v interakcijski točki, in jih ne moremo neposredno detektirati. Razpad mezona  $B$  moramo rekonstruirati iz dolgoživih razpadnih produktov, zato je pomembno, da detektor omogoča detekcijo, meritev gibalne količine in identifikacijo dolgoživih delcev z visoko učinkovitostjo.

Detektor Belle sestavlja več detektorskih podsistemov, ti so prikazani na sliki C.4. Velik del detektorja leži znotraj velikega superprevodnega magneta, ki zagotavlja homogeno magnetno polje z jakostjo 1.5 T. Magnetno polje ukrivi poti nabitih delcev, ki jim sledimo preko ionizacije plina v osrednji potovalni komori. Iz ukrivljenosti sledi izračunamo gibalno količino delca, iz njene orientacije pa njegov naboj. Ostali podsistemi na zunanji strani osrednje potovalne komore so namenjeni identifikaciji delcev in pa detekciji nevtralnih delcev. Pragovni števec Čerenkovih fotonov omogoča ločevanje pionov in kaonov pri relativno visokih gibalnih količinah ( $p \sim 1.2 - 3.5$  GeV), medtem ko pri nižjih gibalnih količinah to nalogo opravlja merilec časa preleta<sup>2</sup>. Sledi še elektromagnetni kalorimeter, s katerim detektiramo fotone in identificiramo elektrone, ter detektor KLM za detekcijo kaonov  $K_L^0$  in identifikacijo mionov. Za meritve časovno odvisnih asimetrij je poleg omenjenih potreben še silicijev detektor mesta razpada, ki leži v najbolj notranjem delu detektorja Belle, najbližje interakcijski točki. Namenjen je natančnemu določanju trajektorij nabitih delcev v bližini interakcijske točke in s tem rekonstrukciji razpadnih točk kratkoživih delcev.



Slika C.4: Detektor Belle z označenimi podsistemi.

<sup>2</sup>Oba podsistema delujeta na principu meritve hitrosti delca. Ob znani gibalni količini in hitrosti lahko preko relacije  $p = \gamma m v$  izračunamo njegovo maso in s tem določimo identiteto.

## C.5 Priprava postopka meritve

### C.5.1 Princip meritve

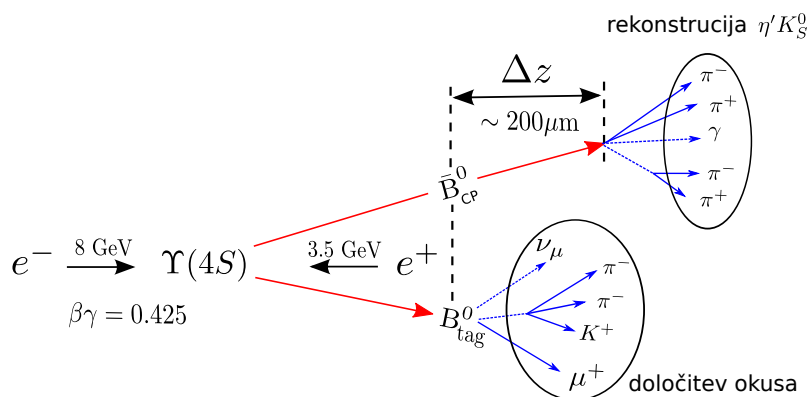
Za meritev časovno odvisne razpadne asimetrije  $a_{\eta'K_S^0}(t)$  (C.7) moramo izbrati vzorec mezonov  $B$ , ki so bili ob času  $t = 0$  v določenem lastnem stanju okusa, za vsak mezon  $B$  določiti njegov okus ( $B^0$  ali  $\bar{B}^0$ ) ob tem času, in izmeriti časovno porazdelitev razpadov v končno stanje  $\eta'K_S^0$ . Razlika med porazdelitvama mezonov  $B^0$  in  $\bar{B}^0$  nam da asimetrijo  $a_{\eta'K_S^0}(t)$  in posledično vrednosti parametrov  $\mathcal{S}_{\eta'K_S^0}$  in  $\mathcal{A}_{\eta'K_S^0}$ .

Določitev časa  $t = 0$  ob katerem je bil mezon  $B$ , ki razpade v  $\eta'K_S^0$  (označimo ga z  $B_{CP}$ ), v lastnem stanju okusa in določitev njegovega okusa ob tem času omogoča dejstvo, da je par  $B\bar{B}$ , ki nastane iz  $\Upsilon(4S)$ , v koherentnem kvantnem stanju. Za meritev izberemo le dogodke pri katerih drugi mezon  $B$  iz para (označimo ga z  $B_{tag}$ ) razpade v končno stanje specifično za mezon  $B^0$  ali  $\bar{B}^0$ . Če mezon  $B_{tag}$  ob času  $t_{tag}$  razpade v stanje specifično za  $B^0$  ( $\bar{B}^0$ ), nam kvantna koherenca pove, da je bil ob tem času mezon  $B_{CP}$  v lastnem stanju nasprotnega okusa, t.j.  $\bar{B}^0$  ( $B^0$ ). Čas med razpadoma mezonov  $B_{tag}$  in  $B_{CP}$ ,  $\Delta t = t_{CP} - t_{tag}$ , je torej ravno čas, ki nastopa v asimetriji  $a_{\eta'K_S^0}(t)$ .

Pri meritvi časa  $\Delta t$  nam pomaga asimetrična zasnova trkalnika KEKB. Nastali par  $B\bar{B}$  v težiščnem sistemu trka praktično miruje, v laboratorijskem sistemu pa se giblje s faktorjem Lorentzovega potiska  $\beta\gamma = 0.425$ . To nam omogoča enostavno pretvorbo med prostorsko in časovno oddaljenostjo razpadov para mezonov  $B$

$$\Delta t \simeq \frac{\Delta z}{c\gamma\beta'}, \quad (\text{C.11})$$

kjer je  $\Delta z$  razdalja med točkama razpada mezonov  $B_{CP}$  in  $B_{tag}$ . Življenjski čas mezona  $B$  je  $\sim 1.5$  ps, torej je tipična razdalja med točkama razpada  $|\Delta z| = \gamma\beta c\tau_B \sim 200\mu\text{m}$ . Predstavljeni princip meritve časovno odvisne asimetrije  $a_{\eta'K_S^0}(\Delta t)$  je shematično prikazan na sliki C.5.



Slika C.5: Princip meritve časovno odvisne kršitve simetrije CP.

Za meritev vrednosti parametrov kršitve CP moramo torej v vsakem dogodku najprej določiti okus mezona  $B_{tag}$  ob času njegovega razpada, rekonstruirati razpad  $B_{CP}$  v končno stanje  $\eta' K_S^0$ , in izmeriti razdaljo med točkama razpadov  $B_{tag}$  in  $B_{CP}$ . Vrednosti parametrov kršitve CP izluščimo s prilagajanjem pričakovane verjetnostne porazdelitve za  $\Delta t$  in okus mezona  $B_{tag}$  na porazdelitev izmerjenih dogodkov.

Iz enačb (C.4) lahko izpeljemo teoretično pričakovano verjetnostno porazdelitev za časovni interval  $\Delta t$  in okus  $q$  ( $q = +1$  ( $q = -1$ ) za  $B_{tag} = B^0$  ( $\bar{B}^0$ ))

$$\mathcal{P}^{sig}(\Delta t, q) = \frac{e^{-|\Delta t|/\tau_{B^0}}}{4\tau_{B^0}} \left[ 1 + q \left( \mathcal{A}_{\eta' K_S^0} \cos \Delta M \Delta t + \mathcal{S}_{\eta' K_S^0} \sin \Delta M \Delta t \right) \right], \quad (C.12)$$

ki pa jo moramo popraviti tako, da vključuje eksperimentalne omejitve naše meritve. Te so: detektorska ločljivost meritve  $\Delta t$ , prisotnost dogodkov ozadja in dogodkov v katerih napačno določimo okus mezona  $B_{tag}$ . Ti popravki na sledeči način spremenijo verjetnostno porazdelitev

$$\begin{aligned} \mathcal{P}^{sig} &\rightarrow \mathcal{P}^{sig} \otimes \mathcal{R} && \text{detektorska ločljivost,} \\ \mathcal{P}^{sig} \otimes \mathcal{R} &\rightarrow f_{sig} \mathcal{P}^{sig} \otimes \mathcal{R} + (1 - f_{sig}) \mathcal{P}^{bkg} && \text{ozadje,} \\ \mathcal{P}^{sig}(\Delta t, q) &\rightarrow \mathcal{P}^{sig}(\Delta t, (1 - 2w)q) && \text{določanje okusa,} \end{aligned} \quad (C.13)$$

kjer je  $\mathcal{R}$  resolucijska funkcija meritve  $\Delta t$ ,  $f_{sig}$  delež signalnih dogodkov (t.j. dogodkov, ki res vsebujejo razpad  $B^0 \rightarrow \eta' K_S^0$ ) v vzorcu rekonstruiranih in izbranih dogodkov,  $\mathcal{P}^{bkg}$  je verjetnostna porazdelitev  $\Delta t$  za dogodke ozadja, in  $w$  delež dogodkov z napačno določenim okusom. Vrednosti  $f_{sig}$ ,  $w$ , resolucijsko funkcijo  $\mathcal{R}$  in verjetnostno porazdelitev  $\mathcal{P}^{bkg}$  določimo za vsak rekonstruiran dogodek posebej, glede na vrsto njegovih opazljivih lastnosti. Na ta način iz podatkov pridobimo kar največ informacije, kar se odraža v večji natančnosti končne meritve (manjši statistični negotovosti izmerjenih parametrov kršitve CP). Vrednosti parametrov kršitve CP nato določimo z nebiniranim maksimiziranjem cenilke verjetnosti

$$\mathcal{L}(\mathcal{S}_{\eta' K_S^0}, \mathcal{A}_{\eta' K_S^0}) = \prod_i \mathcal{P}^i(\Delta t^i, q^i; \mathcal{S}_{\eta' K_S^0}, \mathcal{A}_{\eta' K_S^0}), \quad (C.14)$$

kjer je  $\mathcal{P}^i$  verjetnostna porazdelitev  $\Delta t, q$  za  $i$ -ti dogodek,  $\Delta t^i, q^i$  pa izmerjeni vrednosti v  $i$ -tem dogodku.

### C.5.2 Rekonstrukcija razpada $B^0 \rightarrow \eta' K_S^0$

Izmed vseh dogodkov, ki jih je zabeležil detektor Belle, moramo najprej izbrati tiste v katerih je nastal par  $B\bar{B}$  in je eden izmed mezonov  $B$  razpadel v  $\eta' K_S^0$ . Razvejitevno razmerje za razpad  $B^0 \rightarrow \eta' K_S^0$  je  $(6.6 \pm 0.4) \times 10^{-5}$ . Tako kot mezona  $B$  tudi mezona  $\eta'$  in  $K_S^0$  hitro razpadeta in ju ne moremo neposredno detektirati. Za rekonstrukcijo mezona  $\eta'$  uporabimo naslednje razpadne verige

$$\begin{aligned} \text{veriga } \rho^0 & : \eta' \rightarrow \rho^0 \gamma & \text{z } \rho^0 & \rightarrow \pi^+ \pi^- \\ \text{veriga } \eta \rightarrow \gamma\gamma & : \eta' \rightarrow \pi^+ \pi^- \eta & \text{z } \eta & \rightarrow \gamma\gamma \\ \text{veriga } \eta \rightarrow 3\pi & : \eta' \rightarrow \pi^+ \pi^- \eta & \text{z } \eta & \rightarrow \pi^+ \pi^- \pi^0, \end{aligned}$$

katerih končna stanja vsebujejo le nabite pione in fotone ( $\pi^0$  razpade v dva fotona). Za rekonstrukcijo mezona  $K_S^0$  pa uporabimo razpada  $K_S^0 \rightarrow \pi^+ \pi^-$  in  $K_S^0 \rightarrow \pi^0 \pi^0$ . Omenjeni razpadi predstavljajo dobro polovico vseh razpadov  $B^0 \rightarrow \eta' K_S^0$ .

Vektorje gibalnih količin pionov in fotonov v končnem stanju seštejemo v vektorje gibalnih količin vmesnih mezonov in končno mezona  $B$ . Pri rekonstrukciji uporabimo vrsto selekcijskih kriterijev s katerimi skušamo doseči, da končni vzorec rekonstruiranih mezonov  $B$  vsebuje kar se da veliko dogodkov v katerih je res prišlo do razpada  $B^0 \rightarrow \eta' K_S^0$  (signalnih dogodkov) in kar se da malo dogodkov, ki ne vsebujejo tega razpada (dogodkov ozadja). Z večanjem števila dogodkov ozadja v vzorcu se povečuje statistična negotovost meritve, medtem ko se z večanjem števila signalnih dogodkov ta zmanjšuje. Izbrane selekcijske kriterije optimiziramo s pomočjo simuliranih dogodkov tako, da minimiziramo statistično negotovost meritve. Najučinkovitejši selekcijski kriteriji, ki jih uporabimo, so zahteve po določenih vrednostih invariantnih mas vmesnih mezonov ( $\rho^0, \eta, \eta'$ ). Za nadaljevanje meritve izberemo le dogodke v katerih invariantne mase vmesnih mezonov ležijo v izbranem intervalu okrog njihove nominalne mase. Na ta način zavrnamo velik delež dogodkov ozadja in obdržimo velik delež signalnih dogodkov.

V tako izbranem vzorcu mezonov  $B$  je še vedno relativno velik delež dogodkov ozadja ( $\sim 50\%$ ). Iz študije simuliranih dogodkov ugotovimo, da k ozadju prispevajo večinoma dogodki s procesom  $e^+e^- \rightarrow q\bar{q}$ , kjer je  $q = u, d, s, c$  (te imenujemo kontinuumsko ozadje). Pri dogodkih, rekonstruiranih z razpadno verigo  $\rho^0$ ,  $\sim 1\%$  ozadja prispevajo dogodki, ki vsebujejo razpad para  $B\bar{B}$  v stanje, ki ni  $\eta' K_S^0$ . Da bomo iz meritve dobili prave vrednosti parametrov kršitve CP, moramo poznati delež signalnih dogodkov v končnem vzorcu. Do tega pridemo s pomočjo porazdelitve rekonstruiranih mezonov  $B$  v prostoru naslednjih treh spremenljivk:

- **Razlika energij**  $\Delta E = E_B^{cms} - E_{beam}^{cms}$ , kjer je  $E_{beam}^{cms}$  energija žarkov in  $E_B^{cms}$  energija mezona  $B$ , obe izračunani v težiščnem sistemu. Za mezone  $B$  iz signalnih dogodkov sta ti dve energiji enaki, torej ima njihova porazdelitev vrh pri  $\Delta E = 0$ , ki je razmazan zaradi končne resolucije detektorja.

- **Invariantna masa**  $M_{bc} \equiv \sqrt{(E_{beam}^{cms})^2 - (p_B^{cms})^2}$ , kjer je  $p_B^{cms}$  gibalna količina mezona  $B$  v težiščnem sistemu. Porazdelitev mezonov  $B$  iz signalnih dogodkov ima vrh pri  $M_{bc} = m_B$ , kjer je  $m_B$  masa mezona  $B^0$  ( $\simeq 5.279$  GeV).
- **Spremenljivka oblike dogodka**  $LR$  sestavljena iz večih spremenljivk, ki na osnovi različne prostorske porazdelitve gibalnih količin razpadnih produktov v težiščnem sistemu omogočajo razlikovanje med dogodki, ki vsebujejo par  $B\bar{B}$  (sferično porazdeljeni razpadni produkti) in dogodki kontinuumskega ozadja (razpadni produkti letijo v dve nasprotni strani).

S pomočjo simuliranih signalnih dogodkov in dogodkov ozadja pripravimo model, ki opisuje porazdelitev prvih ( $\mathcal{P}^{sig}$ ) in drugih ( $\mathcal{P}^{bkg}$ ) v prostoru  $M_{bc} - \Delta E - LR$ . S prilagajanjem vsote obeh modelov

$$\mathcal{F}(M_{bc}, \Delta E, LR) = f_{sig} \mathcal{F}^{sig} + (1 - f_{sig}) \mathcal{F}^{bkg}, \quad (C.15)$$

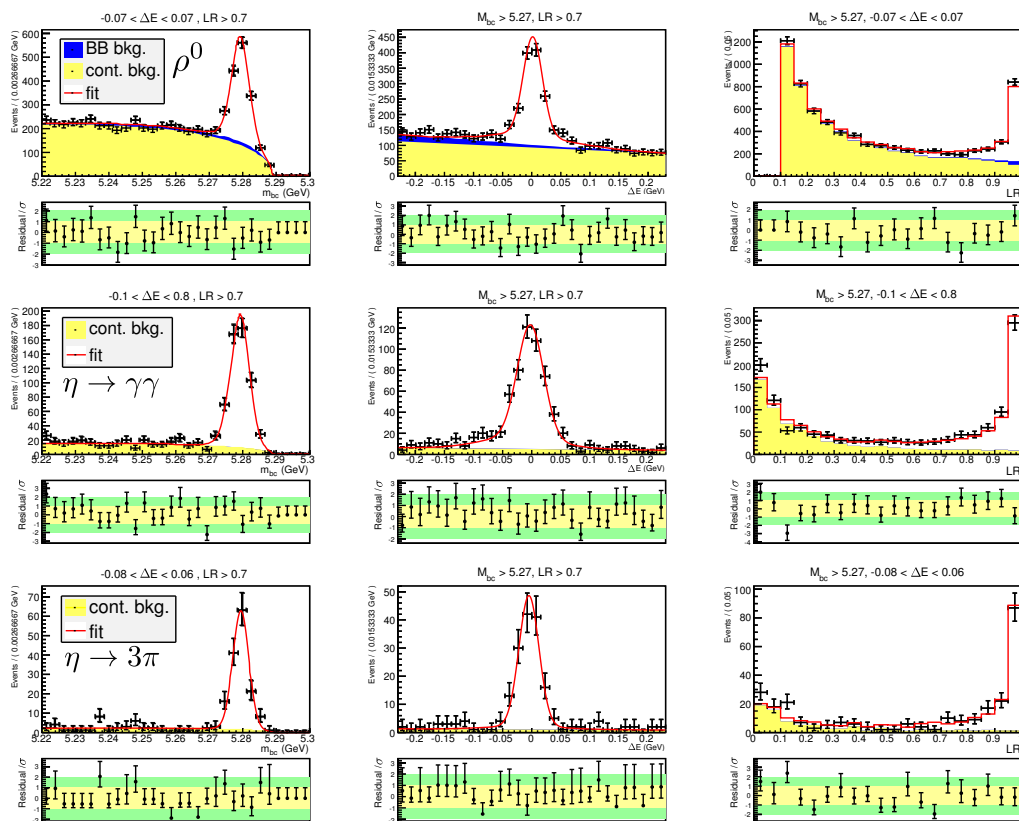
na porazdelitev izbranih razpadov, določimo delež signalnih dogodkov v vzorcu ( $f_{sig}$ ). Rezultati prilagajanja so prikazani na sliki C.6. Iz grafov vidimo, da izbrana verjetnostna porazdelitev  $\mathcal{F}$  dobro opiše porazdelitev podatkov. Ko poznamo vrednost  $f_{sig}$ , s pomočjo signalnega dela verjetnostne porazdelitve (C.15),  $f_{sig} \mathcal{F}^{sig} / \mathcal{F}$ , določimo verjetnost, da je posamezni rekonstruiran dogodek signalni dogodek (glede na specifične vrednosti  $M_{bc}$ ,  $\Delta E$  in  $LR$  v tem dogodku).

Za nadaljevanje meritve izberemo le dogodke v katerih  $M_{bc}$  in  $\Delta E$  mezona  $B$  ležita v t.i. signalnem območju, definiranim z  $M_{bc} > 5.27$  GeV in  $-0.08 < \Delta E < 0.08$  GeV. Z integralom signalnega dela verjetnostne porazdelitve izračunamo, da v signalnem območju leži  $2505 \pm 94$  signalnih dogodkov (kjer je negotovost le statistična).

### C.5.3 Določitev okusa mezona $B_{tag}$

Okus mezona  $B_{tag}$  določimo na podlagi vrste okusno značilnih razpadov mezonov  $B$ . Taki so na primer semileptonski razpadi  $B^0 \rightarrow Xl^+\nu$  (ali  $\bar{B}^0 \rightarrow Xl^-\nu$ ), pri katerih iz pozitivnega (negativnega) naboja visoko energijskega leptona sklepamo, da je  $B_{tag}$  razpadel kot  $B^0$  ( $\bar{B}^0$ ). Algoritem, ki ga uporabimo za določitev okusa je uporabljen tudi v drugih meritvah kolaboracije Belle in je podrobno opisan v [49]. Upošteva vrsto različnih okusno značilnih razpadov in za vsak dogodek vrne vrednost  $q$  (+1 ali -1) ter vrednost parametra  $r$ , ki podaja kvaliteto informacije okusa ( $r \simeq 1$  za dogodke s skoraj enolično določenim okusom in  $r \simeq 0$  za dogodke pri katerih nimamo praktično nobene informacije o okusu). Dogodke razporedimo v 7 razdelkov glede na vrednost  $r$ . V vsakem razdelku že pred tem, s pomočjo velikega kontrolnega vzorca okusno značilnih razpadov mezonov  $B_{sig}$  <sup>(3)</sup>, izmerimo delež dogodkov z napačno določenim okusom ( $w$ ). Razdelki in izmerjene vrednosti  $w$  so prikazani v tabeli C.2.

<sup>3</sup>Tu  $B_{tag}$  uporabimo za določitev okusa, drug mezon  $B$  iz para ( $B_{sig}$ ) pa rekonstruiramo v okusno značilno končno stanje. Postopek je podrobneje opisan v dodatku B.2.



Slika C.6: Enodimenzionalne projekcije verjetnostne porazdelitve  $\mathcal{F}$  (rdeča črta) na  $M_{bc}$  (levo),  $\Delta E$  (sredina) in  $LR$  (desno), za vse tri rekonstruirane verige  $\eta'$  in  $K_S^0 \rightarrow \pi^+\pi^-$ . Prispevka kontinuumskega ozadja in ozadja iz dogodkov  $B\bar{B}$  sta prikazana v rumeni in modri barvi. Črne točke prikazujejo porazdelitev podatkov. Pod vsakim grafom je prikazano odstopanje porazdelitve podatkov od prilagajane funkcije  $\mathcal{F}$ . Območje v prostoru  $M_{bc} - \Delta E - LR$ , ki ga izberemo za prikaz posamezne porazdelitve, je podano nad grafi.

razdelek	1	2	3	4	5	6	7
r	0 – 0.1	0.1 – 0.25	0.25 – 0.5	0.5 – 0.625	0.625 – 0.75	0.75 – 0.875	0.875 – 1
w	0.5	0.42	0.32	0.22	0.16	0.10	0.03

Tabela C.2: Razdelki glede na vrednosti  $r$  in izmerjeni deleži dogodkov z napačno določenim okusom  $B_{tag}$  v vsakem razdelku.

### C.5.4 Rekonstrukcija mesta razpada in resolucijska funkcija za $\Delta t$

Položaj razpada mezona  $B_{CP}$  določimo z ekstrapolacijo sledi  $\pi^+$  in  $\pi^-$ , iz razpada mezona  $\rho^0$  ali  $\eta$  <sup>(4)</sup>, v skupno točko razpada. Pri tem uporabimo le sledi, ki imajo poleg zadetkov v osrednji potovalni komori vsaj tri pripadajoče zadetke v silicijevem detektorju. Najboljšo oceno mesta razpada dobimo z minimizacijo vrednosti

$$\chi^2 = \sum_i \Delta x_i^T V_i^{-1} \Delta x_i,$$

kjer vektor  $\Delta x_i$  vsebuje razliko vrednosti parametrov  $i$ -te uporabljene sledi pred in po ekstrapolaciji vseh sledi v skupno točko, matrika  $V_i$  pa je pripadajoča kovariančna matrika. Iz simuliranih dogodkov ocenimo, da je natančnost tako določenega mesta razpada  $\sim 100 \mu\text{m}$ .

Položaj razpada mezona  $B_{tag}$  določimo z algoritmom, ki je podrobneje opisan v [52]. Algoritem z minimizacijo vrednosti  $\chi^2$  ekstrapolira vse preostale sledi v dogodku (ki jih ne uporabimo pri rekonstrukciji mezona  $B_{CP}$ ) v skupno izhodiščno točko. Pri tem zavrže sledi z zelo velikim prispevkom k  $\chi^2$ , saj te v mnogo primerih izvirajo iz razpadov vmesnih dolgoživih stanj ( $D$  ali  $K_S^0$  mezonov), ki preletijo znatno razdaljo preden razpadejo. S tem pristopom lahko tudi mesto razpada mezona  $B_{tag}$  določimo z natančnostjo  $\sim 100 \mu\text{m}$ .

Iz meritve mesta razpada  $B_{CP}$  in  $B_{tag}$  po enačbi (C.11) določimo čas  $\Delta t$ . Končno ločljivost določitve slednjega opišemo z resolucijsko funkcijo  $\mathcal{R}^{sig}$ , ki jo sestavimo kot konvolucijo štirih prispevkov

$$\mathcal{R}^{sig}(\Delta t) = \mathcal{R}_{det}^{CP} \otimes \mathcal{R}_{det}^{tag} \otimes \mathcal{R}_{np} \otimes \mathcal{R}_{kin}.$$

Prva dva opisujeta detektorsko ločljivost meritve mesta razpada mezona  $B_{CP}$  in  $B_{tag}$ , tretji opisuje razmazanost mesta razpada  $B_{tag}$  zaradi sledi, ki izvirajo iz razpadov vmesnih stanj, četrti prispevek pa opisuje razmazanost  $\Delta t$ , do katere pride zaradi predpostavke, da mezona  $B$  v težiščnem sistemu mirujeta. Natančen opis resolucijske funkcije  $\mathcal{R}^{sig}$  je podan v [53]. Povejmo le, da resolucijsko funkcijo parametriziramo kot funkcijo negotovosti meritve mesta razpada ( $\sigma_z$ ) in vrednosti  $\chi^2$ , ki ju dobimo iz procesa rekonstrukcije mesta razpada.

### C.5.5 Porazdelitev $\Delta t$ za dogodke ozadja

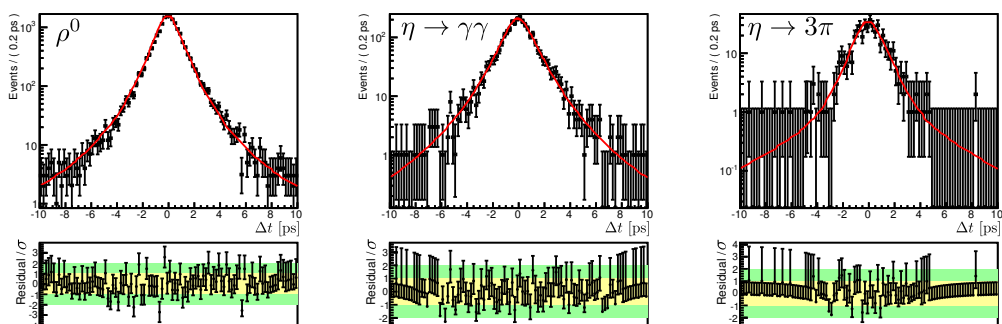
Da bi iz meritve dobili nepristranske vrednosti parametrov kršitve CP, moramo poleg deleža signalnih dogodkov v vzorcu poznati tudi porazdelitev  $\Delta t$  za dogodke ozadja. Slednjo opišemo z verjetnostno porazdelitvijo

$$\mathcal{P}_{phys}^{bkg}(\Delta t) = f_\delta \delta(\Delta t - \mu_\delta) + (1 - f_\delta) \exp\left(-\frac{|\Delta t - \mu_\tau|}{\tau_{bkg}}\right), \quad (\text{C.16})$$

---

<sup>4</sup>Razpadni čas mezonov  $\rho^0$  in  $\eta$  je tako kratek, da razpadeta praktično na mestu razpada mezona  $B$

ki jo konvoluiramo z resolucijsko funkcijo dogodkov ozadja, sestavljeno iz vsote treh Gaussovih funkcij. Proste parametre verjetnostne porazdelitve  $\mathcal{P}_{phys}^{bkg} \otimes \mathcal{R}^{bkg}$  določimo posebej za dogodke iz kontinuumskega ozadja in dogodke ozadja z razpadom para  $B\bar{B}$ , ter za vsako razpadno verigo. Obliko ozadja z razpadom  $B\bar{B}$  določimo s prilagajanjem verjetnostne porazdelitve (C.16) na porazdelitev  $\Delta t$  simuliranih dogodkov tega tipa, obliko kontinuumskega ozadja pa s prilagajanjem na porazdelitev  $\Delta t$  dogodkov v območju  $M_{bc} < 5.265$  GeV,  $-0.1 < \Delta E < 0.25$  GeV in  $LR < 0.9$ . V tem območju je delež signalnih dogodkov zanemarljiv ( $< 0.1\%$ ). Primerjava verjetnostne porazdelitve iz prilagajanja in porazdelitve dogodkov kontinuumskega ozadja je prikazana na sliki C.7. Vidimo, da izbrani model dobro opiše izmerjeno porazdelitev dogodkov.



Slika C.7: Primerjava verjetnostne porazdelitve  $\mathcal{P}^{bkg}(\Delta t)$  s porazdelitvijo  $\Delta t$  dogodkov v izbranem  $M_{bc} - \Delta E - LR$  območju, za vse tri rekonstruirane verige z  $K_S^0 \rightarrow \pi^+ \pi^-$ . Velika večina dogodkov v tem območju je dogodkov kontinuumskega ozadja (iz študije simuliranih dogodkov vidimo, da je prispevek signalnih dogodkov in dogodkov ozadja z razpadom para  $B\bar{B}$  zanemarljiv ( $< 1\%$ )).

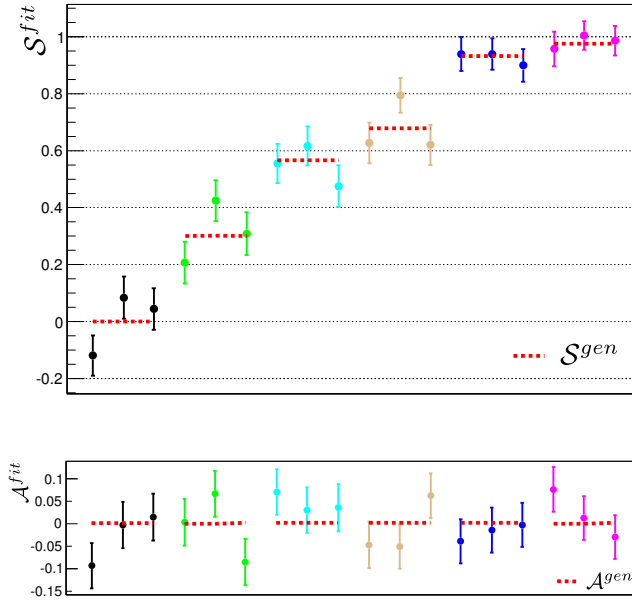
### C.5.6 Testi pripravljenega postopka

Preden izvedemo meritev na vzorcu izmerjenih dogodkov, opravimo vrsto testov pripravljenega postopka, s katerimi se prepričamo v nepristranskost le tega. Pri tem si pomagamo s simuliranimi dogodki, pri katerih lahko izmerjene vrednosti parametrov kršitve CP primerjamo s pravimi vrednostmi<sup>5</sup>, in pa dogodki v kontrolnem vzorcu razpadov  $B^+ \rightarrow \eta' K^+$ . Na tem mestu predstavimo le rezultate dveh pomembnih testov.

Celoten postopek meritve preizkusimo na več vzorcih simuliranih dogodkov, z različnimi generiranimi vrednostmi parametra  $\mathcal{S}_{\eta' K_S^0}$  (v vseh pa uporabimo  $\mathcal{A}_{\eta' K_S^0} = 0$ ). V teh vzorcih združimo simulirane signalne dogodke in dogodke ozadja v razmerju, kot ga pričakujemo v vzorcu izmerjenih dogodkov. Za določitev vseh verjetnostnih porazdelitev, ki jih potrebujemo za konstrukcijo končne verjetnostne

<sup>5</sup>t.j. vrednostmi, ki jih uporabimo pri generiranju simuliranih dogodkov.

cenilke  $\mathcal{L}$ , uporabimo enake postopke kot so opisani v prejšnjih poglavjih. Vrednosti parametrov kršitve CP, ki jih z maksimizacijo  $\mathcal{L}$  izluščimo iz omenjenih vzorcev simuliranih dogodkov, prikazuje slika C.8. Primerjava izmerjenih vrednosti z generiranimi potrjuje veljavnost uporabljene metode, saj se te v okviru statistične negotovosti meritve ujemajo.



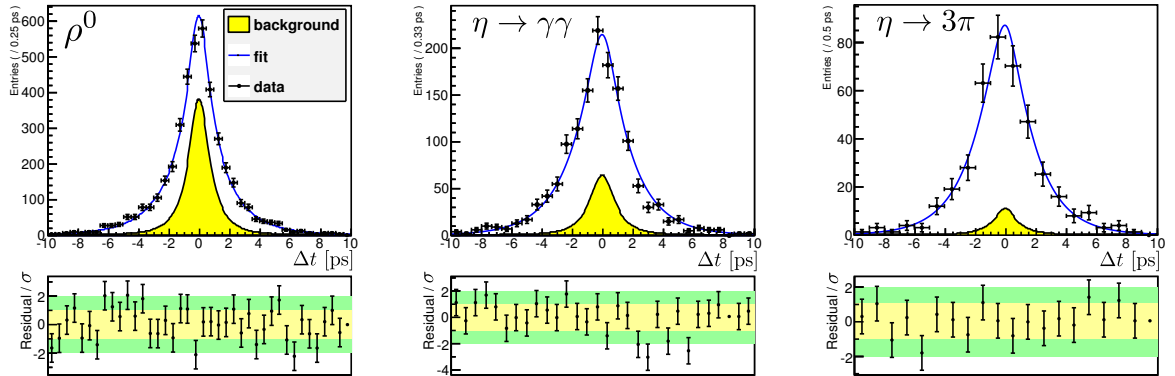
Slika C.8: Primerjava izmerjenih (barvne točke) in generiranih (rdeča črtkana črta) vrednosti parametrov kršitve CP iz vzorca simuliranih dogodkov. Za vsako generirano vrednost parametra  $\mathcal{S}$  izvedemo meritev na treh neodvisnih vzorcih dogodkov.

Drug pomemben test, ki ga opravimo, je meritev življenskih časov mezona  $B^+$  in  $B^0$ . Postopek te meritve je v veliki meri enak kot meritev parametrov kršitve CP, le da za signalne dogodke uporabimo verjetnostno porazdelitev  $\mathcal{P}^{sig}(\Delta t) = \frac{1}{2\tau_B} \exp(-|\Delta t|/\tau_B)$ , ki je neodvisna od okusa ( $q$ ). Življenski čas  $\tau_B$  postavimo kot prosti parameter, ki ga določimo z maksimizacijo verjetnostne cenilke. Z izjemo določitve okusa mezona  $B_{tag}$ , ta meritev ponuja test vseh ostalih korakov meritve parametrov kršitve CP. Vrednost  $\tau_{B^+}$  določimo iz porazdelitve dogodkov kontrolnega vzorca z razpadom  $B^+ \rightarrow \eta' K^+$ , vrednost  $\tau_{B^0}$  pa iz porazdelitve dogodkov našega glavnega vzorca (ki ga uporabimo za meritev parametrov kršitve CP). V obeh primerih uporabimo enako resolucijsko funkcijo, saj mezonov  $K_S^0$  in  $K^+$  ne uporabimo pri meritvi mesta razpada mezonov  $B$ . Rezultata meritev sta

$$\tau_{B^+} = 1.650 \pm 0.027 \text{ ps}, \quad \tau_{B^0} = 1.494 \pm 0.043 \text{ ps}, \quad (\text{C.17})$$

kjer je prikazana le statistična negotovost. Ti dve vrednosti sta konsistentni s trenutnima svetovnima povprečjema,  $\tau_{B^+} = 1.641 \pm 0.008$  in  $\tau_{B^0} = 1.519 \pm 0.007$  [24].

Na sliki C.9 je prikazana primerjava verjetnostne porazdelitve  $\mathcal{P}(\Delta t)$  in porazdelitve dogodkov kontrolnega vzorca v signalnem območju  $M_{bc} - \Delta E$ .



Slika C.9: Primerjava verjetnostne porazdelitve  $\mathcal{P}(\Delta t)$  (modra črta) s porazdelitvijo dogodkov kontrolnega vzorca v signalnem območju (črne točke). Prispevek dogodkov ozadja je obarvan rumeno.

## C.6 Rezultat meritve

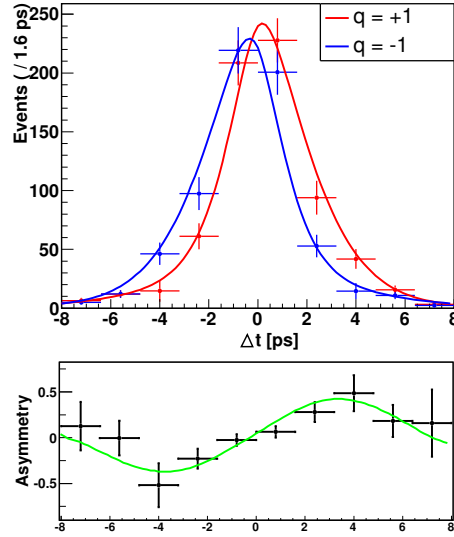
Po tem, ko smo se prepričali o nepristranskosti pripravljenega postopka, izvedemo meritve parametrov kršitve CP na vzorcu rekonstruiranih dogodkov  $B^0 \rightarrow \eta' K_S^0$ . Iz začetnega vzorca, ki vsebuje 772 milijonov razpadov parov  $B\bar{B}$ , zbranih z detektorjem Belle, smo uspeli rekonstruirati  $2505 \pm 94$  signalnih dogodkov (kjer je negotovost le statistična). Vrednosti parametrov kršitve CP, ki jih dobimo z maksimizacijo verjetnostne cenilke  $\mathcal{L}$ , so

$$\begin{aligned} \mathcal{S}_{\eta' K_S^0} &= +0.71 \pm 0.07(stat) \pm 0.03(sist), \\ \mathcal{A}_{\eta' K_S^0} &= +0.02 \pm 0.05(stat) \pm 0.03(sist), \end{aligned} \quad (C.18)$$

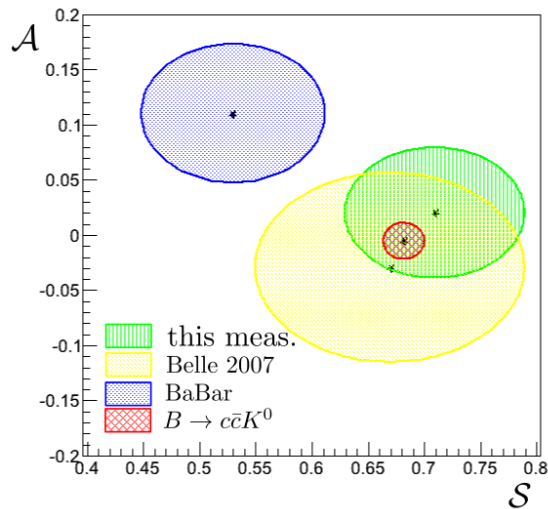
kjer je prva negotovost statistična, druga pa sistematska. Največji prispevek k sistematski negotovosti prinese nenatančno poznavanje parametrov resolucijske funkcije ( $0.020$  k  $\mathcal{S}_{\eta' K_S^0}$  in  $0.006$  k  $\mathcal{A}_{\eta' K_S^0}$ ), obravnavamo pa še vrsto drugih prispevkov, kateri v večini izhajajo iz nenatančnega poznavanja parametrov verjetnostne porazdelitve  $\mathcal{P}(\Delta t, q)$  (delež signalnih dogodkov, delež dogodkov z napačno določenim okusom, oblika porazdelitve  $\Delta t$  za dogodke ozadja, ...). Primerjava verjetnostne porazdelitve  $\mathcal{P}^{sig}(\Delta t, q)$  s porazdelitvijo  $\Delta t$  rekonstruiranih signalnih dogodkov z  $q = +1$  in  $q = -1$  je prikazana na sliki C.10. Vidimo, da se verjetnostna porazdelitev in porazdelitev dogodkov dobro ujemata.

Vrednosti parametrov  $\mathcal{S}_{\eta' K_S^0}$  in  $\mathcal{A}_{\eta' K_S^0}$  v (C.18), ki predstavljajo končni rezultat meritve, so najnatančnejše izmerjene vrednosti omenjenih parametrov doslej. Slika C.11 prikazuje primerjavo izmerjenih vrednosti z dosedanjimi meritvami in vrednostjo

$\sin 2\phi_1$  (izmerjeno v razpadih  $B \rightarrow c\bar{c}K^0$ ), ki podaja pričakovano vrednost parametra  $\mathcal{S}_{\eta'K_S^0}$  v okviru SM. Iz slike vidimo, da je rezultat predstavljene meritve konsistenten tako z rezultati dosedanjih meritev, kot tudi z napovedjo SM.



Slika C.10: Primerjava porazdelitve  $\Delta t$  signalnih dogodkov z  $q = +1$  (rdeče točke) in  $q = -1$  (modre točke) z ustrezno komponento verjetnostne porazdelitve, ki jo nam da vrednosti parametrov kršitve CP (rdeča in modra črta). Upoštevani so le dogodki z dobro določenim okusom (z  $r > 0.5$ ). Spodnji graf prikazuje asimetrijo  $a_{\eta'K_S^0}$  (definirano v enačbi C.7) v izmerjeni porazdelitvi (črne točke) in pričakovano asimetrijo ob izmerjenih vrednostih parametrov  $\mathcal{S}_{\eta'K_S^0}$  in  $\mathcal{A}_{\eta'K_S^0}$  (zeleno črta).



Slika C.11: Primerjava vrednosti parametrov  $\mathcal{S}_{\eta'K_S^0}$  in  $\mathcal{A}_{\eta'K_S^0}$  iz te in prejšnjih meritev kolaboracij Belle [35] in BaBar [36]. Poleg omenjenih je podana še vrednost parametrov kršitve CP v razpadih  $B \rightarrow c\bar{c}K^0$  [29], ki predstavlja pričakovano vrednost parametrov  $\mathcal{S}_{\eta'K_S^0}$  in  $\mathcal{A}_{\eta'K_S^0}$  v okviru SM.

---

## C.7 Zaključek

V delu smo predstavili meritev parametrov kršitve simetrije CP v razpadu  $B^0 \rightarrow \eta' K_S^0$ . Meritev je bila opravljena na vzorcu 772 milijonov parov  $B\bar{B}$ , zbranih z detektorjem Belle v času njegovega delovanja (1999-2010). Izmerjene vrednosti

$$\begin{aligned}\mathcal{S}_{\eta'K_S^0} &= +0.71 \pm 0.07(stat) \pm 0.03(sist), \\ \mathcal{A}_{\eta'K_S^0} &= +0.02 \pm 0.05(stat) \pm 0.03(sist),\end{aligned}$$

so konsistentne z rezultati dosedanjih meritev in napovedjo SM.

Za konec se ozrimo še nekoliko v prihodnost te in podobnih meritev. Izmerjene vrednosti parametrov kršitve CP v razpadih, ki potekajo preko procesa  $b \rightarrow s\bar{q}q$ , ki je dominiran s pingvinskimi diagrami, in so kot taki občutljivi na prispevke novih izvorov kršitve CP, so v vseh primerih konsistentne z napovedmi SM. Trenutno dosežena natančnost teh meritev pa še vedno dopušča znatne prispevke kršitve CP iz izvorov onkraj SM. Ti so naravno prisotni v večini modelov nove fizike in nujni tudi s kozmološkega vidika (razlaga očitne asimetrije med materijo in antimaterijo v vesolju). Ker je eksperimentalna natančnost meritev v večini razpadov omenjenega tipa dominirana s statistično negotovostjo, lahko do natančnejših meritev pridemo le z večjim vzorcem mezonov  $B$ . To možnost bo ponudil trkalnik SuperKEKB z detektorjem Belle II [57, 58] (nadgradnja trkalnika KEKB in detektorja Belle), ki bo začel delovati v letu 2016. Z detektorjem Belle II nameravamo do leta 2023 zabeležiti  $\sim 50$ -krat več razpadov mezonov  $B$ , kot jih je zabeležil Belle. To bo omogočilo meritve parametrov kršitve CP z natančnostjo nekaj  $10^{-2}$  (npr. za  $\mathcal{S}_{\eta'K_S^0}$  pričakujemo negotovost  $\simeq 0.02$  [59]) in morda vodilo do detekcije novih izvorov kršitve simetrije CP. Če slednjih ne bomo opazili, bo to postavilo močne omejitve na možno strukturo (predvsem okusnega dela) modelov nove fizike.



# Bibliography

- [1] T.D. Lee, C. N. Yang, Phys. Rev. **104** (1), 254 (1956)
- [2] C.S. Wu, E. Ambler *et al.*, Phys. Rev. **105** (4), 1413 (1957)
- [3] J.W. Coronin, V.L. Fitch, Phys. Rev. Lett. **13**, 138 (1964)
- [4] M. Kobayashi and T. Maskawa, Prog. Theor. Phys. **49**, 652 (1973)
- [5] A. Abashian *et al.* (Belle Collaboration), Nucl. Instrum. Methods Phys. Res. A **479**, 117 (2002).
- [6] BaBar Collaboration, Nucl. Instrum. Meth. A **479**, 1 (2002)
- [7] K. Abe *et al.* (Belle Collaboration), Phys. Rev. Lett. **87**, 091802 (2001)
- [8] B. Aubert *et al.* (BaBar Collaboration), Phys. Rev. Lett. **87**, 091801 (2001)
- [9] A.D. Sakharov, Pis'ma Zh. Eksp. Teor. Fiz. **5**, 32 (1967) [JETP Lett. **5**, 24 (1967)].
- [10] M. B. Gavela *et al.*, Nucl. Phys. B **430**, 382 (1994)
- [11] Atlas Collaboration, Phys. Lett. B **716**, 1 (2012)
- [12] CMS collaboration, Phys. Lett. B **716**, 30 (2012)
- [13] Y. Grossman and M. P. Worah, Phys. Lett. B **395**, 241 (1997); D. Atwood and A. Soni, Phys. Lett. B **405**, 150 (1997); M. Ciuchini *et al.*, Phys. Rev. Lett. **79**, 978 (1997).
- [14] S.L. Glashow, J. Iliopoulos, L. Maiani, Phys. Rev. D **2**, 1285 (1970)
- [15] M. Beneke, Phys. Lett. B **620**, 143 (2005).
- [16] A. R. Williamson and J. Zupan, Phys. Rev. D **74**, 014003 (2006)
- [17] H-Y. Cheng, C-K. Chua, and A. Soni, Phys. Rev. D **72**, 014006 (2005).
- [18] M. Gronau, J. L. Rosner, and J. Zupan, Phys. Rev. D **74**, 093003 (2006)
- [19] M. Beneke and M. Neubert, Nucl. Phys. A **675**, 333 (2003)

## BIBLIOGRAPHY

---

- [20] M. Gronau, J. L. Rosner, and J. Zupan, *Phys. Lett. B* **596**, 107 (2004).
- [21] Y. Grossman, Z. Ligeti, Y. Nir, and H. Quinn, *Phys. Rev. D* **68**, 015004 (2003)
- [22] J. E. Kim and G. Carosi, *Rev. Mod. Phys.* **82**, 557(2010)
- [23] L. Wolfenstein, *Phys. Rev. Lett.* **51**, 21 (1983)
- [24] J. Beringer *et al.* (Particle Data Group), *Phys. Rev. D* **86**, 010001 (2012) and 2013 partial update for the 2014 edition.
- [25] J. Charles *et al.* (CKMfitter Group), *Eur. Phys. J. C* **41**, 1-131 (2005) [hep-ph/0406184], updated results and plots available at: <http://ckmfitter.in2p3.fr>
- [26] R. Jost, *Hel. Phys. Acta* **30**, 409 (1957)
- [27] A.J. Buras, W. Slominski, and H. Steger, *Nucl. Phys. B* **245**, 369 (1984).
- [28] I. I. Bigi *et al.*, in "CP violation", ed. C. Jarlskog, Signapore World Scientific (1989)
- [29] D. Asner *et al.* (HFAG), arXiv:1010.1589v3 [hep-ex] (2001), updated results and plots available at: <http://www.slac.stanford.edu/xorg/hfag>
- [30] I.I. Bigi and A.I. Sanda, "CP violation", Cambridge Univ. Press (2000)
- [31] A. B. Carter and A. I. Sanda, *Phys. Rev. D* **23**, 1567 (1981); I. I. Bigi and A. I. Sanda, *Nucl. Phys. B* **193**, 85 (1981).
- [32] L. Silvestrini, *Ann. Rev. Nucl. Part. Sci.* **57**, 405 (2007)
- [33] I. Adachi *et al.* (Belle Collaboration), *Phys. Rev. Lett.* **108**, 171802 (2012)
- [34] B. Aubert *et. al* (BaBar Collaboration), *Phys. Rev. D* **79**, 052005 (2009)
- [35] K.-F. Chen *et al.* (Belle Collaboration), *Phys. Rev. Lett.* **98**, 031802 (2007)
- [36] B. Aubert *et al.* (BaBar Collaboration), *Phys. Rev. D* **79**, 052003 (2009)
- [37] S. Kurokawa and E. Kikutani, *Nucl. Instrum. Methods Phys. Res. A* **499**, 1 (2003)
- [38] T. Iijima, B PHYSICS AND CP VIOLATION: Proceedings. Edited by H.-Y. Cheng and W.-S. Hou. Singapore, World Scientific, 29 (2000)
- [39] D. J. Lange *et al.*, *Nucl. Instrum. Methods Phys. Res. A* **462**, 152 (2001).
- [40] QQ - The CLEO Event Generator, <http://www.lns.cornell.edu/public/CLEO/soft/qq> (unpublished)
- [41] R. Brun *et al.*, GEANT 3.21, CERN DD/EE/84-1 (1984).

- 
- [42] Rene Brun and Fons Rademakers, Nucl. Instrum. Methods Phys. Res. A **389**, 81 (1997). See also <http://root.cern.ch/>.
- [43] J. Tanaka, *Development of the Low Momentum Track Reconstruction Program and the Kinematic Fitter for the Belle Experiment*, M.Sc. thesis, University of Tokyo (1999).
- [44] M. Feindt and U. Kerzel, Nucl. Instrum. Meth. A **559**, 190 (2006).
- [45] K. Abe *et al.* (Belle Collaboration), Phys. Rev. Lett. **87**,101801 (2001).
- [46] R. A. Fisher, Annals Eugen. **7**, 179 (1936).
- [47] K. Abe *et al.* (Belle Collaboration), Phys. Rev. Lett. **91**, 261801 (2003).
- [48] H. Albrecht *et al.* (ARGUS collaboration ), Phys. Lett. B **241**, 278 (1990).
- [49] H. Kakuno *et al.* (Belle Collaboration), Nucl.Instrum.Meth. A **533**, 516 (2004).
- [50] K. Abe *et al.* (Belle Collaboration), Phys. Rev. D **71**, 072003 (2005).
- [51] H. Sahoo *et al.* (Belle Collaboration), Phys. Rev. D **77**, 091103 (2008).
- [52] K. F. Chen *et al.* (Belle Collaboration), Phys. Rev. D **72**, 012004 (2005).
- [53] H. Tajima *et al.*, Nucl. Instrum. Meth. A **533**, 370 (2004).
- [54] F. James, MINUIT - Function Minimization and Error Analysis - Reference Manual (2000).
- [55] O. Long *et al.*, Phys. Rev. D **68**, 034010 (2003)
- [56] Y. Yusa, Belle Collaboration internal note #1300.
- [57] “Super-KEKB Letter of Intent (LoI)”, KEK Report 04-4 (2004), available from <http://www-superkekb.kek.jp>
- [58] Belle II Collaboration, KEK Report 2010-1, arXiv:1011.0352 [physics.ins-det] (2010)
- [59] Belle II Collaboration, KEK Report 2009-12, arXiv:1002.5012 [hep-ex] (2009)



## **Izjava o avtorstvu**

Izjavljam, da je predložena disertacija rezultat lastnega znanstveno-raziskovalnega dela.

Ljubljana, 16. 9. 2013

Luka Šantelj



